FORSCHUNGSZENTRUM JÜLICH GmbH

Institut für Festkörperforschung

Spin-Resolved Photoemission of Thin Magnetic Films

Uwe Alkemper

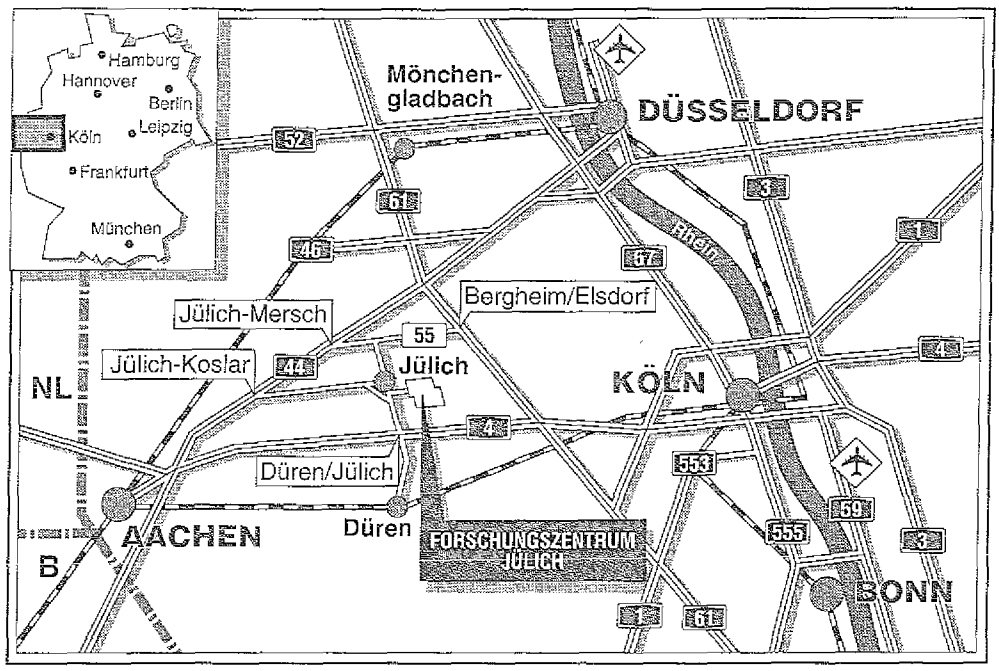

Berichte des Forschungszentrums Jülich ; 2706
ISSN 0366-0885
Institut für Festkörperforschung Jül-2706

Zu beziehen durch: Forschungszentrum Jülich GmbH · Zentralbibliothek
Postfach 1913 · D-5170 Jülich · Bundesrepublik Deutschland
Telefon: 02461/61-6102 · Telefax: 02461/61-6103 · Telex: 833556-70 kfa d

Spin-Resolved Photoemission of Thin Magnetic Films

Uwe Alkemper

Contents

1 Introduction

Magnetic properties of thin films offer a fascinating field of research. Besides the fundamental interest in physical properties, such as the magnetic moment, the Curie temperature and the dependence of the magnetization on temperature or film thickness, magnetic materials are also technically important. The understanding of ferromagnetism and the electronic structure of ferromagnets are a first step in the development of new data storage devices.

To study the electronic structure of ultrathin films in the monolayer regime, it is important to use a surface sensitive experimental technique.

Electrons are very well suited as a carrier of information, due to their small inelastic mean free path (IMFP) in solids. For energies in the range of 10-1000eV the IMFP of electrons is typically below 20Å (see fig. 1.1).

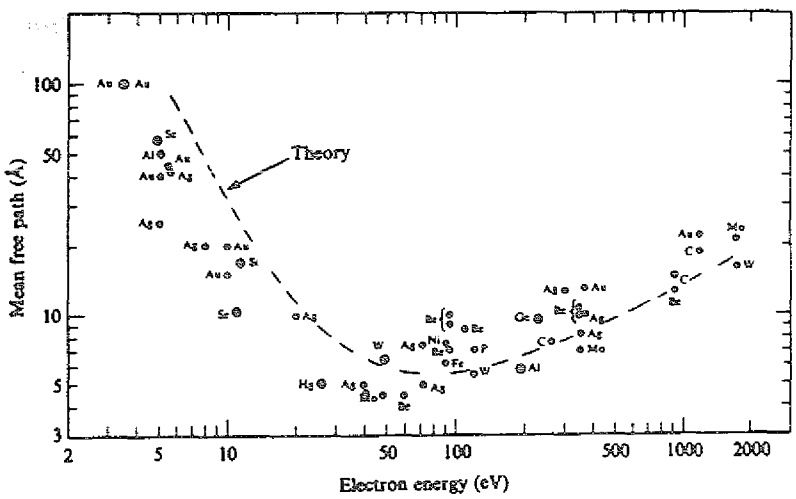

Fig. 1.1: *Universal Curve* of electron mean free path, after [Zangwill, 88]. Theory by Penn [Penn, 76]

One of the most common techniques using electrons as a sample probe is *photoelectron spectroscopy*. Photons of a specific energy are absorbed by electrons in the sample. Energy conservation demands that the excited system takes the energy of the annihilated photon as a whole. If the energy of the excited electrons is high enough to overcome the work function they can be detected outside the sample and characterized with respect to their kinetic energy, momentum and spin.

2 Theory

2.1 Photoelectron Spectroscopy

The photoelectric effect was discovered at the end of the last century by Hertz, Lenard and Thompson. In 1921, Einstein received the Nobel prize for his theoretical work on the photoelectric effect [Einstein, 1905]. Today we make use of the photoelectric effect to study the electronic structure of many different systems such as atoms and molecules in the gas phase, solids, clean or covered with adsorbates, and liquids. The photon energies range from a few electron volts (Ultraviolet Photoemission Spectroscopy, UPS) to kiloelectron volts (X-ray Photoemission Spectroscopy, XPS). With this energy range, it is possible to study electron core levels as well as valence-band states.

Fig. 2.1 schematically shows the photoemission spectrum of a metal. In a photoemission experiment the intensity of the photocurrent is measured as a function of the kinetic energy E_{kin} of the emitted electrons, for a fixed photon energy $h\nu$. The work function Φ is the difference between the potential of the vacuum level and the Fermi level. Φ can change with the material and crystal plane [Kittel]. Small amounts of contamination or adsorbates can change the work function rather drastically.
The binding energy E_B is the physical property that can be compared directly with band-structure calculations. Usually it is referred to the Fermi energy. Electrons with the lowest binding energy have the highest kinetic energy ($E_B = h\nu - E_{kin} - \Phi$). In a metal, the origin of electrons with the lowest binding energy is E_F. This can be used to determine the Fermi edge in the photoemission spectra.

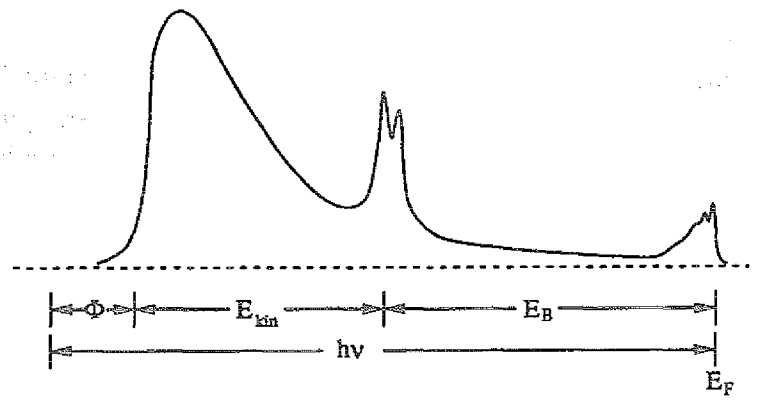

Fig. 2.1: Schematically drawn photoemission spectrum

By measuring the kinetic energy, the momentum k and the spin s of the emitted electrons one gains information about the wavefunctions of the filled states and the transiton probabilities into empty states. With tuneable light sources such as synchrotron radiation, it is possible to determine the 3D band structure of a periodic solid or the 2D band structure of a thin film or a surface.

2.2 The Photoionization Process

In many cases photoemission experiments are connected closely to theoretical calculations. Band-structure calculations and their comparison to experiment for example are fundamental to the understanding of the electronic structure of crystals. Differences and similarities between theory and experiment give hints to the accuracy of the theory.
Due to the fact, that the photoelectric effect is a quantum phenomenon, it has to be discussed in the framework of quantum mechanics. Here the theory of photoionization is discussed as a single-particle excitation starting from *Fermi's Golden Rule.*

$$\frac{d\omega}{dt} = \frac{2\pi}{\hbar} | < \psi_f | w^{\pm} | \psi_i > |^2 \cdot \delta(E_f - E_i \pm \hbar\omega) \tag{1}$$

It describes the transition rate between the final state ψ_f and the initial state ψ_i of the unperturbed Hamiltonian H_0 due to a periodic perturbation of the form

$$W(t) = w^{\pm} e^{\pm i\omega t} \tag{2}$$

The origin of Fermi's Golden Rule is the Schrödinger equation treated in first order perturbation theory.
If the perturbation is given by the vector potential of an electromagnetic wave, H takes the well known form

$$H = H_0 + W(t) \qquad \text{with} \qquad W(t) = \frac{e}{2mc}(\mathbf{A}\cdot\mathbf{p} + \mathbf{p}\cdot\mathbf{A}) - e\phi + \frac{e^2}{2mc^2}|A|^2 \tag{3}$$

Usually the calibration is choosen in a way that ϕ is zero. The second order term in the vector potential is very small and can be neglected.
With the commutator relation $[\mathbf{p}, \mathbf{A}] = -i\hbar\nabla\mathbf{A}$ the following expression for $W(t)$ is obtained

$$W(t) = \frac{e}{mc}(\mathbf{A}\cdot\mathbf{p} - i\hbar\nabla\mathbf{A}) \tag{4}$$

Often the term $\nabla\mathbf{A}$ is omitted, because it is normally small with respect to $\mathbf{A}\cdot\mathbf{p}$. It can become important at the surface and change the cross sections as discussed in detail in ref. [Plummer, 82].

$$W(t) = \frac{e}{mc}\mathbf{A}\cdot\mathbf{p} \tag{5}$$

The vector potential of the electromagnetic wave that causes the transition can be written in the form

$$\mathbf{A}(\mathbf{r}, t) = \mathbf{A_0}\cdot e^{-i\omega t + i\mathbf{kr}} \tag{6}$$

With equations 2, 5 and 6 we get the following expression for the term $w^{\pm}$ in the perturbation

$$w^{\pm} = \frac{e}{mc}\cdot\mathbf{A_0}\cdot e^{-i\mathbf{kr}}\cdot\mathbf{p} \tag{7}$$

Equation 7 introduced into Fermi's Golden Rule gives

$$\frac{d\omega}{dt} = \frac{2\pi}{\hbar}\cdot\frac{e}{mc}\cdot| < \psi_f | e^{-i\mathbf{kr}}\cdot\mathbf{A_0}\cdot\mathbf{p} | \psi_i > |^2 \delta(E_f - E_i - \hbar\omega) \tag{8}$$

On the atomic scale A can be regarded as a constant since the spatial variation of the vector potential is very small and the wavefunctions differ from zero only for very small r. Furthermore we use only the first-order term of the series expansion $e^{-i\mathrm{kr}} \simeq 1 - i\mathrm{kr}$. As a result we get the following dipole approximation

$$\frac{d\omega}{dt} = \frac{2\pi}{\hbar} \cdot \frac{e}{mc} \cdot | < \psi_f|\mathrm{p}|\psi_i > \cdot \mathrm{A}_0|^2 \delta(E_f - E_i - \hbar\omega) \tag{9}$$

If $< \psi_f|\mathrm{p}|\psi_i >= 0$ is valid, one must also take into account terms of higher order in the series expansion.
In the experiment we are interested in the *differential cross section* $\frac{d\sigma}{d\Omega}$, which is proportional to the transition rate and given by

$$\frac{d\sigma}{d\Omega} \sim | < \psi_f|\mathrm{p}|\psi_i > \cdot \mathrm{A}_0|^2 \delta(E_f - E_i - \hbar\omega) \tag{10}$$

In some cases it is better to use other forms of this equation

$$\frac{d\sigma}{d\Omega} \sim | < \psi_f|\mathrm{r}|\psi_i > \cdot \mathrm{A}_0|^2 \delta(E_f - E_i - \hbar\omega) \tag{11}$$

or

$$\frac{d\sigma}{d\Omega} \sim | < \psi_f|\nabla V|\psi_i > \cdot \mathrm{A}_0|^2 \delta(E_f - E_i - \hbar\omega) \tag{12}$$

These equations are obtained from eqn. 10 by using the following commutator relations

$$[H_0, \mathrm{p}] = -\frac{\hbar}{i}\nabla V \qquad \text{and} \qquad [H_0, \mathrm{r}] = \frac{2i}{\hbar}\mathrm{p} \tag{13}$$

$$< \psi_f|\mathrm{p}|\psi_i >= \frac{\hbar}{2i} < \psi_f|[H_0, \mathrm{r}]|\psi_i >= \frac{\hbar}{2i}(E_f - E_i) < \psi_f|\mathrm{r}|\psi_i > \tag{14}$$

$$< \psi_f|\mathrm{p}|\psi_i >= \frac{1}{E_f - E_i} < \psi_f|[H_0, \mathrm{p}]|\psi_i >= \frac{1}{\hbar\omega} < \psi_f|-\frac{\hbar}{i}\nabla V|\psi_i >= -\frac{1}{i\omega} < \psi_f|\nabla V|\psi_i > \tag{15}$$

Due to the translation symmetry parallel to the surface the initial state $|\psi_i >$ and the final state $|\psi_f >$ have to fulfill the Bloch equation

$$\psi(\mathrm{r} + \mathrm{P}) = e^{i\mathrm{k}_\parallel \cdot \mathrm{P}}\psi(\mathrm{r}) \tag{16}$$

where P represents a two dimensional lattice vector in the surface plane. A finite scattering amplitude can be found if the difference between the momentum of the final state $\mathrm{k}_{\mathrm{f}\parallel}$ and initial state $\mathrm{k}_{\mathrm{i}\parallel}$ is equal to a lattice vector g in the 2D reciprocal lattice.

$$\Delta\mathrm{k}_\parallel = \mathrm{k}_{\mathrm{f}\parallel} - \mathrm{k}_{\mathrm{i}\parallel} = \mathrm{g} \tag{17}$$

When the excited electrons pass the surface potential barrier, the momentum parallel to the surface is conserved $\mathrm{k}_\parallel^{out} = \mathrm{k}_\parallel^{in}$.

The two components of the wave vector outside the solid can be obtained with the dispersion relation of a free electron

$$E_{kin} = \frac{\hbar^2 \mathrm{k}^2}{2m} \tag{18}$$

by measuring the kinetic energy and the emission angle Θ of the emitted electrons.

$$\mathrm{k}_{\parallel} = \sqrt{\frac{2m}{\hbar^2} E_{kin}} \cdot \sin\Theta \tag{19}$$

$$\mathrm{k}_{\perp}^{out} = \sqrt{\frac{2m}{\hbar^2} E_{kin}} \cdot \cos\Theta \tag{20}$$

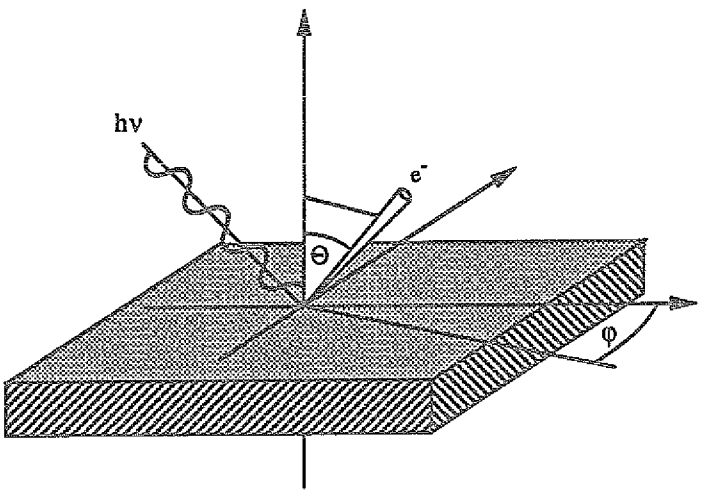

Fig. 2.2: Photoemission geometry.

For surface or adsorbate induced states the binding energy does not depend on $\mathrm{k}_{\perp}$ and the knowledge of the binding energy as a function of $\mathrm{k}_{\parallel}$ is sufficient to characterize the states.

The situation is more difficult for bulk states that depend on $\mathrm{k}_{\perp}$ as well. Due to the fact that the momentum $\mathrm{k}_{\perp}$ of the electrons is not conserved when they pass the surface one needs information about the final state inside the sample.
The most simple approach to the final state is to suggest a free-electron final state. In this picture the final state inside the sample is regarded as a free-electron parabola modified by an inner potential V_0.

$$\text{outside:} \qquad E_f = \frac{\hbar^2}{2m}(\mathrm{k}_{f\parallel}^2 + \mathrm{k}_{f\perp}^{out\,2}) \tag{21}$$

$$\text{inside:} \qquad E_f - V_0 = \frac{\hbar^2}{2m}(\mathrm{k}_{f\parallel}^2 + \mathrm{k}_{f\perp}^{in\,2}) \tag{22}$$

The inner potential is typically in the range -5 to -10eV and corresponds to the average ionic potential, seen by the electrons. With eqn. 21 and 22 we get for $k_{f\perp}^{in}$

$$k_{f\perp}^{in} = \sqrt{k_{f\perp}^{out\,2} - \frac{2m}{\hbar^2} V_0} \tag{23}$$

$k_{||}$ and $k_{\perp}^{out}$ are given by eqn.19 and 20. Most of the spectra presented in this work are measured in normal emission ($\Theta = 0$). In this case the momentum parallel to the surface vanishes and with eqn. 19, 20 and 23 we get

$$k_{||} = 0 \tag{24}$$

$$k_{\perp}^{in} = \sqrt{\frac{2m}{\hbar^2} \cdot (E_f - V_0)} \tag{25}$$

$$= \sqrt{\frac{2m}{\hbar^2} \cdot (E_i + h\nu - V_0)} \tag{26}$$

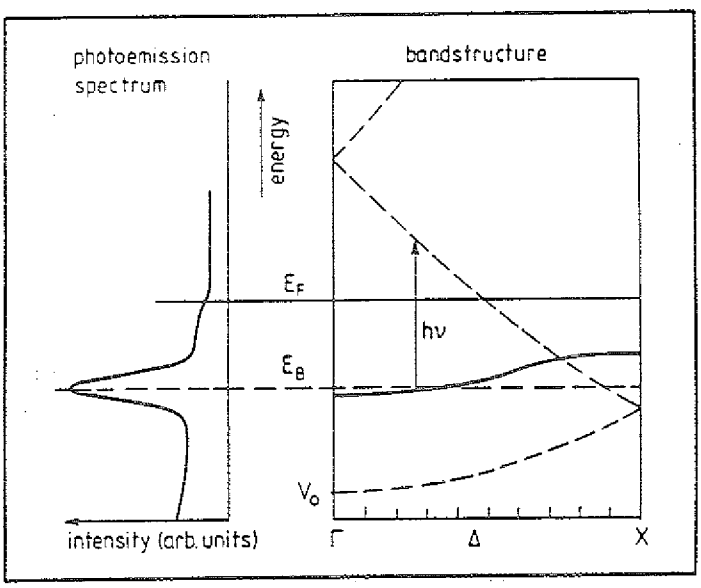

Fig. 2.3: Band structure determination with angle-resolved photoemission

The only unknown parameter in eqn. 26 is the inner potential V_0. To determine the inner potential in the experiment, we try to identify emission from a high-symmetry point like the Γ point. When we change the photon energy in a range, where k crosses the border between two Brillouin zones we see, due to the periodicity in k-space, an extremum in the binding energy E(k). At the extremum we know $k_{\perp}^{in}$ as well as the binding energy E_i and V_0 can be determined with eqn. 26.

2.3 Spin-Resolved Photoemission Spectroscopy

The spin polarisation of the emitted electrons is defined as [Kessler, 85]

$$P = \mathrm{tr}\sigma\rho \tag{27}$$

where σ is the Pauli spin matrix and ρ is the spin density matrix. When we are interested only in one quantization axis (z) eqn. 27 becomes

$$P_z = \frac{N^{\uparrow} - N^{\downarrow}}{N^{\uparrow} + N^{\downarrow}} \tag{28}$$

$N^{\uparrow}$ ($N^{\downarrow}$) is the number of electrons with a magnetic moment parallel (antiparallel) to the chosen axis.
For a ferromagnetic sample it is natural to choose the direction of magnetization as a quantization axis. The density of states of a ferromagnet is spin-split with an excess of electrons of one spin direction. They are referred to as *majority-spin* ($\uparrow$) electrons, those of opposite spin are *minority-spin* ($\downarrow$) electrons.
The band structure of majority- and minority-spin electrons are of similar shape, but shifted by the so-called *exchange splitting.*
Usually we do not show the polarization curves, but the spin dependent energy distribution curves (EDC) that can be compared directly with the band structure. They can be obtained from the photoemission current $I_0(E)$ and spin-polarization curve $P(E)$ with the equation

$$I^{\uparrow,\downarrow}(E) = \frac{1}{2} I_0(E) \cdot (1 \pm P(E)) \tag{29}$$

To measure the polarization experimentally we use the asymmetry of a scattering process called *Mott scattering.*

2.4 Mott Scattering

A beam of polarized electrons that is scattered at a thin Au foil shows an anisotropy in the intensity of the scattered electrons that corresponds to the degree of polarisation.
The reason for this anisotropy can be found in the relativistic spin-orbit coupling. If we choose the z-axis as a quantization axis, the scattering potential of the scattered electrons differs by $\pm\mu_B \cdot M$ between electrons that pass the Au atom on the right and on the left side. This results in a left-right asymmetry A(P) of the photocurrent.
In the Mott detector we use this left-right intensity asymmetry to determine the degree of polarization of the incident electron beam. Mott scattering denotes the high-energy scattering (about 100keV) at the atomic nuclei.
The asymmetry is defined as the product of the polarization and the sensitivity of the Mott detector.

$$A = P \cdot S_{eff} \tag{30}$$

S is the so-called *Sherman factor.*
The Sherman factor depends on the kinetic energy of the scattered electron beam as well

as on the angle Θ between the incident beam and the detector. It is largest for scattering nuclei with large atomic number Z, electron beam energy E=120keV and $\Theta = \pm 120^0$. With these parameters, the Sherman factor has been calculated to be S=0.39 for a single scattering event. For a Au-foil approximately 2000Å thick we get an effective Sherman factor S_{eff} that is, due to multiple scattering, smaller than S. A typical value for S_{eff} is 0.2. This means, we obtain an asymmetry of the intensities between left and right detectors, which is only 20% of the polarization of the electrons.
Experimentally an additional detector measures the electrons that pass the gold film in forward direction ($\Theta = 0^0$). With this detector the so-called spin-integrated (sum of minority- and majority-spin electrons) spectrum is measured. The count rates of this detector are about 10^3 times larger than the count rates of the detectors measuring the back-scattered electrons.

2.5 Selection Rules

In many solids the valence-band structure consists of various bands in a small energy interval. A spectrum that shows the overlapping structures of all these bands at once is very difficult to discuss. The situation becomes even more complicated, when surface, adsorbate-induced or interface states also have to be interpreted.
For that reason we usually choose specific experimental geometries that allow us to observe only states with a special symmetry. Parameters that may define the symmetry of the observed states are:
- the direction and the polarization of the incident light
- the orientation of the crystal
- the position of the detector

For example consider a crystal mirror plane. Solutions to Schrödinger's equation for electrons with a momentum in this plane have to be of either even or odd parity under reflection about the mirror plane.
If the detector is placed in this mirror plane, we observe only final states ψ_f of even parity. Odd-parity final states have a node in the plane, the square of the amplitude, proportional to the intensity at the detector, is zero. That means, if we observe electrons propagating in a mirror plane of the crystal, we can see states with even parity only.
The dipole matrix element $< \psi_f | \mathbf{A} \cdot \mathbf{p} | \psi_i >^2$ gives the transition rate between initial state ψ_i and final state ψ_f (9). The symmetry of the dipole operator $\mathbf{A} \cdot \mathbf{p}$ with respect to the mirror plane is even if the polarization vector $\mathbf{A}$ is in the mirror plane and odd if it is perpendicular. Since we know, that the final state has to be even, as well as the whole dipole matrix element, ψ_i and $\mathbf{A} \cdot \mathbf{p}$ must have the same parity. With $\mathbf{A}$ parallel to the mirror plane, we can detect even initial states wheras odd initial states can be seen with $\mathbf{A}$ perpendicular to the mirror plane.
Selection-rule tables for different geometries can be found in [Eberhardt, 80].
Depending on the polarisation vector of the incident light one defines *s-polarized* and *p-polarized light.* If the polarisation vector is perpendicular to the plane of incidence (the plane of incidence is given by the surface normal and the direction of the incident light)

the light is called s-polarized and if the A is parallel to the plane of incidence the light is called p-polarized.
In most of our experiments the direction of the incident light is chosen perpendicular to the surface. In this case the incident light is defined to be s-polarized.

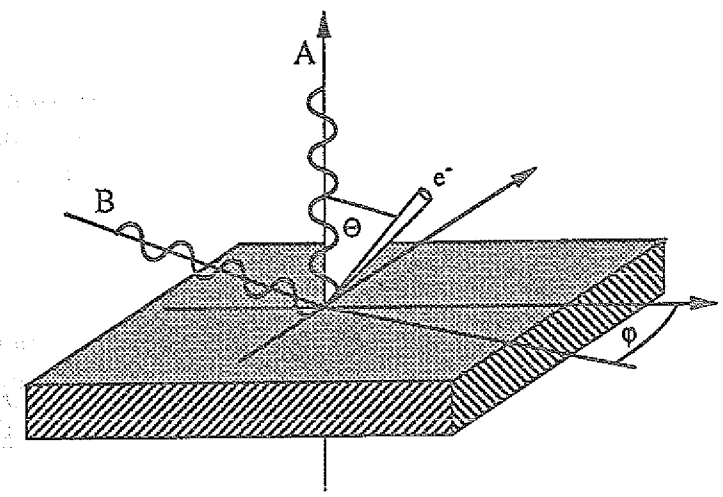

Fig. 2.4:(A) s- and (B) p-polarized light. p polarization (A||n, n=surface normal direction) can be archieved by off-normal incidence of the light only.

In table 1 we show the selection rules for low-index faces in normal emission which are important in our experiment.

Crystal Face	Coordinate axes			Irreducible Representations	Initial Symmetries		
	x	y	z		$\mathbf{A} \parallel x$	$\mathbf{A} \parallel y$	$\mathbf{A} \parallel z$
(001)	$<100>$	$<010>$	$<001>$	$\Delta_1\Delta_1'\Delta_2\Delta_2'\Delta_5$	Δ_5	Δ_5	Δ_1
(110)	$<001>$	$<1\underline{1}0>$	$<110>$	$\Sigma_1\Sigma_2\Sigma_3\Sigma_4$	Σ_3	Σ_4	Σ_1
(111)	$<\underline{1}10>$	$<\underline{11}2>$	$<111>$	$\Lambda_1\Lambda_2\Lambda_3$	Λ_3	Λ_3	Λ_1

Table 1: Dipole-allowed initial state symmetries for normal emission from low-index faces of cubic crystals after ref. [Hermanson, 77]. For each face the directions of Cartesian coordinate axes are referred to the conventional cubic axes and irreducible representations at $k_{||}=0$ are listed in single group notation. A is the vector potential of the light.

2.6 Magnetism

The magnetism of atoms has its origin in the way the electrons in a given shell occupy the orbitals of an atom. The ground state of an atom is characterized by an electronic configuration as given by *Hund's Rules*:

1. The maximum value of the total spin S allowed by the exclusion principle;

2. The maximum value of the orbital angular momentum L consistent with this value of S;

3. The value of the total angular momentum J is equal to $|L - S|$ when the shell is less than half full and to $L+S$ when the shell is more than half full. When the shell is just half full, the application of the first rule gives $L = 0$, so that $J = S$.

When we apply the first rule to Fe ($[Ar]4s^2 3d^6$) the d shell will fill in a way that the sum of the spins is $S = 2$. Another configuration, where the spin up and spin down orbitals are filled to an equal extent and the sum of the spins is S=0, is higher in energy and cannot be found as a ground state. With a total spin of $S = 2$ the magnetic moment of an Fe atom is $M = 4\mu_B$ where μ_B is the Bohr magneton.

The first of Hund's rules has its origin in the Pauli exclusion principle and the coulomb repulsion between electrons. The Pauli exclusion principle prevents two electrons of the same spin from being at the same place at the same time. For this reason electrons with the same spin stay farther apart than electrons of opposite spin. Due to the coulomb interaction, the energy of electrons with parallel spin is lower than the energy of electrons with opposite spin.

2.7 Stoner Model

In the solid the simple model using Hund's rules does not apply. Parallel spins minimize the exchange energy but increase the kinetic energy. The change in the kinetic energy is a direct consequence of the delocalization of the valence electrons, as can be seen in the following model for free electrons. In this model of free electrons the Fermi sphere has a radius of $k_F = (3\pi^2 n)^{1/3}$ where each k state is occupied with a spin up and a spin down electron ($n = N/V$ is the electron density). The resulting average kinetic energy is $E_{kin} = N \cdot \frac{3}{5} \cdot \frac{\hbar^2 k_F^2}{2m}$. In a ferromagnetic state, where each state is occupied with only one electron, the volume of the Fermi sphere is twice as big, and the average kinetic energy increases by a factor of $2^{2/3}$.
The exchange energy can compensate this effect only partially and delocalized electrons therefore show a smaller tendency for ferromagnetic behaviour than localized electrons. Consequently the localization of the valence electrons influences the magnetic behaviour of a solid.

In the Stoner model for 3d transition metals the effective Hamiltonian $H_\pm$ of the majority and minority electrons is determined by the spin-independent one-particle Hamiltonian H_0 of the paramagnetic case modified by an exchange term

$$H_\pm = H_0 \mp \frac{1}{2} IM \tag{31}$$

where I is the exchange integral ($I \simeq 0.7eV$ for 3d atoms) and M is the magnetic moment. The corresponding energy eigenvalues change to

$$E^{\pm}_{k\nu} = E^{0}_{k\nu} \mp \frac{1}{2} IM \tag{32}$$

As a result the band structure and the density of states $n_{\pm}(E)$ for the two spin directions are of the same shape, but shifted in energy. The number of particles per unit cell and the local magnetic moment are given by

$$N = \int^{E_F} (n_0 \cdot (E + \frac{1}{2} IM) + (n_0 \cdot (E - \frac{1}{2} IM))dE \tag{33}$$

$$M = \int^{E_F} (n_0 \cdot (E + \frac{1}{2} IM) - (n_0 \cdot (E - \frac{1}{2} IM))dE \tag{34}$$

n_0 is the paramagnetic density of states. $E_F = E_F(M)$ can be calculated with eqn 33 and eqn. 34 must be solved self consistently to determine M.

$$M = F(M) \quad \text{with} \quad F(M) = \int^{E_F} (n_0 \cdot (E + \frac{1}{2} IM) - (n_0 \cdot (E - \frac{1}{2} IM))dE \tag{35}$$

When we solve this equation, we find either one trivial solution $M = 0$ that corresponds to the paramagnetic case or we find three solutions $M = 0, \pm M_s$ that correspond to a ferromagnetic state with the spontaneous magnetization M_s. The solution $M = 0$ in the ferromagnetic state is not stable. A criterion that allows one to distinguish between the two cases is the *Stoner criterion.* If

$$F'(0) = n_0(E_F) \cdot I > 1 \tag{36}$$

the system is ferromagnetic.

Besides the Stoner criterion which allows one to decide if a system is paramagnetic or ferromagnetic, there exists another important relation for the bandwidth W

$$W^2 = z|h|^2 \tag{37}$$

where z is the coordination number and h is the hopping matrix element, which is mainly influenced by the overlap of the wavefunctions for two neighbouring atoms. For example, when the lattice constant of a crystal is reduced the wavefunctions have a greater overlap and h increases. With h also the bandwidth increases according to eqn. 37. When the bandwidth increases and the number of states is constant, the density of states n_0 becomes smaller. As a result the Stoner criterion is less likely fulfilled and the tendency for ferromagnetism is decreased. With the same argument one finds that compression decreases the tendency for ferromagnetism, and expansion increases the tendency.
In a two-dimensional system the number of nearest neighbours z is less than for a 3D system. The bandwidth is smaller and the 2D system is more likely ferromagnetic than the 3D system.
Within a group of transition metals the bandwidth decreases with increasing atomic

number. The reason for this is a lowering of the energy position of the bands with the consequence of stronger localization. The same is true for the rare earths.
The Stoner model is just an approximation. It predicts a shift in the density of states between majority- and minority-spin direction but it can not explain differences in the shape. In this model the exchange splitting is expected to be independent of k.

3 Experiment

3.1 Experimental Conditions

The experiments have been performed at BESSY in Berlin. BESSY is a 800MeV electron storage ring that provides synchrotron light with photon energies ranging from the infrared up to about 2000eV.
The experimental set up is located in an ultra-high vacuum (UHV) chamber. For the production of high-quality overlayers it is necessary to have a gas pressure as low as possible to avoid contamination of the surface. In our experiments the base pressure was typically $1 - 2 \cdot 10^{-10}$mbar. A schematic drawing of the experimental set up is shown in fig 3.1

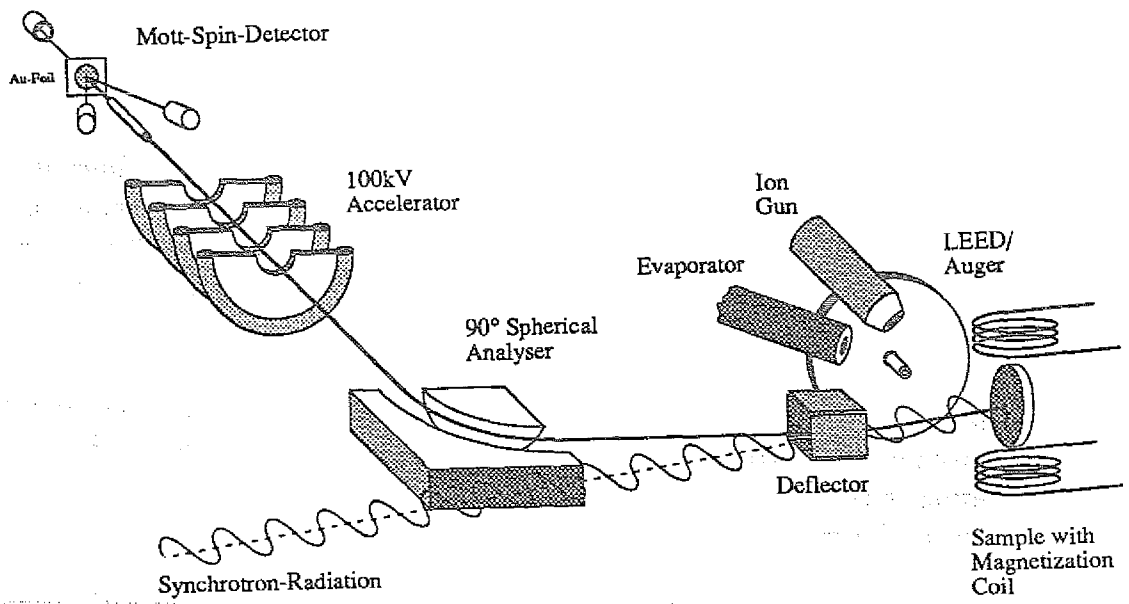

Fig. 3.1: Shematic drawing of the experimental set up

A manipulator holds the sample and allows translation in three directions plus rotation about the z-axis.
To obtain high-quality overlayers, it is of great importance to start with a clean and well-ordered substrate. A very common method to remove contamination from the surface is to use a Sputtergun. Ar^+ or Ne^+ ions are accelerated with high voltage towards the sample and remove atoms from the sample simply by ion bombardment.
This method is useful for sample cleaning, but produces structural defects in the surface

region.

To get a well ordered surface after sputtering, the sample is heated. The temperature of the heating depends on the substrate material. It must stay below the melting point, but be high enough to increase the mobility of the atoms at the surface. A tungsten filament, not shown in fig. 3.1, was mounted on the manipulator very near to the sample. A constant current of 6-10 Amperes through the filament produces enough radiation to heat the sample up to about 800 K. For higher heating rates or higher temperatures, we used electron-beam heating. The electrons that are emitted by the filament are accelerated towards the sample with a high voltage that is applied between filament and sample.
The temperature of the sample is checked with a Ni-CrNi thermocouple, spot-welded close to the sample.

We checked the structure and cleanliness of the sample with a conventional four-grid LEED/Auger system. A mono-energetic electron beam impinges on the sample and the scattered electrons are collected on a screen.
In the LEED study the reciprocal lattice of the sample surface is displayed on a fluorescent screen. The sharpness of the LEED spots corresponds to the degree of order at the sample surface.
Contaminants like carbon or oxygen can be detected by their characteristic lines in the Auger spectra. Four grids are mounted in front of the screen and the potentials given to these grids define a minimum kinetic energy of the deteted electrons. The retarding voltage is modulated with a given freqency and connected to a lock-in amplifier. With this system we can not only record the integral Auger signal of electrons passing the retarding voltage but also the 1st and 2nd derivative of this curve.
The 1st derivative gives the energy distribution curve (EDC) of the Auger electrons and the 2nd derivative (1st derivative of the EDC) is commonly used for studies of the growth mode or for testing the cleanliness of the sample surface. The 2nd derivative is commonly called the *Auger spectrum.*

Co has been evaporated from a high-purity Co wire by heating the wire with electron bombardment to its evaporation temperature. The electrons were emitted from a tungsten filament and accelerated with a potential of 1kV, applied between the filament and the Co wire. To avoid radiative heating of the chamber the evaporator was water cooled. A small hole in the water-cooled shielding determined the direction of the beam of Co atoms. During evaporation the pressure in the chamber stayed below $4 \cdot 10^{-10}$mbar.
The evaporation rate was checked with an oscillating quartz crystal thickness monitor.

Due to the fact that we measure electron spin dependent effects, the magnetization of the sample is of great importance. It must be possible to magnetize the sample permanently and homogenously, because the size of the light spot and the analyzer acceptance area of a demagnetized sample are typically larger than a single Weiss domain. Usually picture frame crystals or, as in our experiments, thin films are used. This is because they

have a high magnetic remanence and negligible magnetic stray fields.
The magnetization coils are mounted near the sample. A short pulse of high current through the coils produces a permanent in-plane magnetization in the sample. The arrangement of the sample and the magnetization coils is shown in fig. 3.1. The samples were oriented in a way that the magnetic field was applied along the [110] direction for studies on (100) surfaces and along the [$\bar{2}$11] direction for studies on (111) surfaces.

The experiments have been performed at the TGM1 (toroidal grating monochromator) and TGM5 beamlines at BESSY. TGM1 is connected to a bending magnet and provides monochormatized light of 10-100eV photon energy. TGM5 transmits the synchrotron light from a wiggler/undulator and thus provides a higher photon flux and photon energies of 25-200eV. The use of synchrotron radiation as a light source has the advantage of producing intense, bright and continuously tunable light.
In our chamber the direction of the incoming synchrotron light and the direction of the collected electrons are identical. Capacitor plates deflect the electron beam behind the first lens system and separate the electrons from the incident light. In the next step a 90^0 spherical analyser is used to select electrons of a given kinetic energy. A static field is applied between the two spheres of a spherical capacitor. It influences the passing electrons by electrostatical force and allows only electrons of a given trajectory to pass the spheres. The energy resolution is 250meV.
Another lens system directs the electrons to the Mott spin analyser. Mott scattering is one of the most common methods for measuring the spin polarization of the electrons. The electron beam is accelerated to 100keV and directed at a 2000Å Au-foil target. Two surface barrier detectors measure the number of electrons scattered into angles about $\pm 120^0$. A third detector measures the spinintegrated signal at $\Theta = 0$ of the unscattered electrons. The Sherman factor of the Mott detector is 0.2. This means the asymmetry measured in the detectors is 20% of the polarization of the electron beam.

3.2 Sample Preparation

We used two different types of Cu substrate crystals in this work, one crystal has been cut parallel to the (100) plane and the other one has been cut parallel to the (111) plane. Both Cu crystals were prepared in the same way, cut from a single crystal and then polished.
In the UHV system they have been treated with cycles of sputtering and heating until the LEED pattern showed sharp and bright spots and no contaminations were detectable with Auger electron spectroscopy. For the sputtering procedure a beam energy in the range of 600-1200eV was used. The heating temperature of approximately 1000K was kept well below the melting point of Cu ($T_{melt} = 1358K$).

After the initial preparation the adsorbate films were removed by sputtering for 10-60 min with about 800eV beam energy. The time depends on the thickness of the film. Heating of the sample to about 800K for 1 min was sufficient to once again obtain a sharp

LEED pattern.

The Co films were evaporated from a high-purity Co wire with a typical rate of 1ML/min. During the evaporation the pressure in the chamber stayed below $4 \cdot 10^{-10}$ mbar. A freshly prepared Co film can be used for 4-5 hours before contamination appears in the photoemission spectra.

4 Growth mode of Co on Cu

Bulk Co can be found in two different structures, fcc and hcp. At room temperature the hcp phase is present, but at 720K Co undergoes a phase transition and the structure changes to fcc. By choosing Cu as a substrate it is possible to stabilize, through epitaxy, ultrathin film structures of fcc Co at room temperature. An important first step in characterizing the properties of such materials is a determination of the growth mode.

4.1 Auger Study of Co/Cu(111)

The Auger process is a non-radiative decay of a core hole involving three atomic levels, XYZ. In a first step a core hole in level X is created by the removal of an electron. This can be done with irradiation or by electron/ion bombardment. In the second step this level is filled with an electron of an outer shell Y. To fulfill energy conservation the difference in Energy $\Delta E = E_Y - E_X$ is transferred to a third electron in the Z shell. When ΔE is greater than the binding energy of this electron, it can be detected with the kinetic energy $E_{kin} = E_Z - \Delta E$. This so-called *Auger process* is a competitive process to the generation of a photon of the characteristic wavelength $h\nu = \Delta E$. Auger transitions are denoted with the three levels involved. The one described above is an XYZ Auger transition. Auger lines are (like characteristic radiation) typical for each element. One tenth of a monolayer of a specific element can easily be detected by its fingerprint in the Auger spectrum.

We used Auger electron spectroscopy (AES) to study the growth mode of Co on Cu(111).
Usually three different growth modes are considered, depending on the interaction between substrate and adsorbate atoms.

1. In *Frank van der Merve growth* the adsorbate grows layer by layer on the substrate. The interaction between substrate and adsorbate atoms is stronger than the interaction between two neighbouring atoms in the adsorbate. The surface energy is less for completing one layer, than for starting the growth of the next layer.

2. In *Vollmer-Weber growth* the opposite is true. In this case, the interaction of the in-plane atoms is stronger than the interaction between different layers. The adsorbate forms three dimensional islands that grow on the substrate.

3. In *Stranski-Krastanov growth* the adsorbate starts growing layer by layer, but after one or more completed layers nucleation takes place and the adsorbate begins to grow by forming three dimensional islands.

With AES we can distinguish between these three growth modes. In a figure showing AES intensity versus adsorbate deposition the resulting theoretical curves for the three growth modes appear very different. In *Frank van der Merve growth* we expect an exponential

decrease of the substrate Auger signal and a corresponding increase of the adsorbate signal as the thickness of the overlayer increases

$$I^{sub} = I_0^{sub} \exp(\frac{-d}{\lambda^{ads}}) \tag{38}$$

$$I^{ads} = I_0^{ads}(1 - \exp(\frac{-d}{\lambda^{ads}})) \tag{39}$$

λ is the inelastic mean free path (IMFP) of the substrate- (adsorbate-) electrons scattered through the overlayer. Within a layer the substrate signal increases linearly as the layer is filled (see fig. 4.2). The completion of a layer would therefore be indicated by a discontinuity in the slope of the Auger curves and the exponential curves in eqns. 38 and 39 describe the envelope of the substrate and the adsorbate Auger curves.

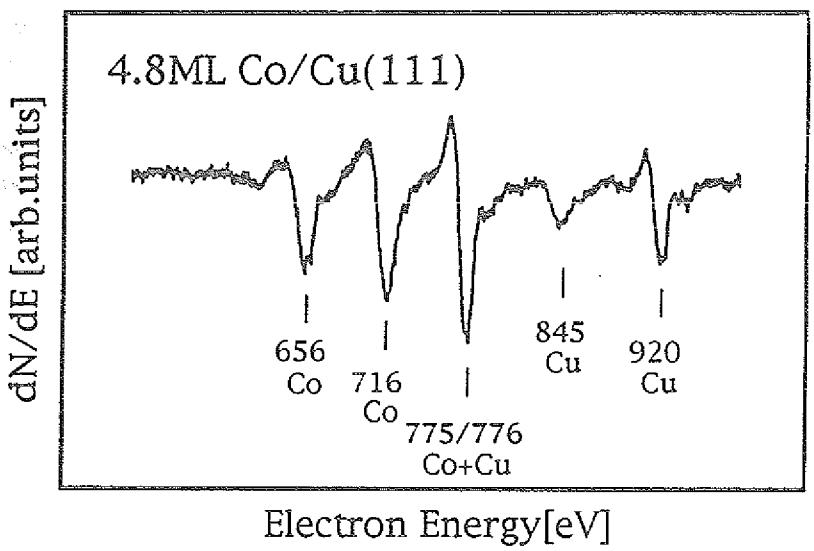

Fig. 4.1: Derivative Auger spectrum of 4.8ML Co/Cu(111)

In the case of *Vollmer-Weber growth* the substrate signal decreases much slower because even for high coverages there is unattenuated emission from uncovered substrate areas. Correspondingly the adsorbate signal increases much slower with increasing coverage. Finally *Stranski-Krastanov growth* is indistinguishable from layer-by-layer growth for the first few layers until island growth begins. As shown schematically in fig 4.2 (dotted line; here island growth starts after one layer), it corresponds to a superposition of Frank van der Merve and Vollmer-Weber growth.

A detailed study of the system Pd/Fe(100) in comparison with different growth models can be found in [Rader, 91]. In the work of Rader the Auger-signal intensities of the substrate signal and of the adsorbate signal have been calculated for several growth modes, including the growth modes considered for Co/Cu(111) in this work. His work discusses the accuracy and the reliability of statements about the growth modes. We performed our Auger measurements about Co/Cu(111) in the same conditions and with the same experimental setup as he did. A general dicussion of this subject together with a compilation of the Auger data for many systems can be found in Ref. [Argile, 89].

Figure 4.1 shows a derivative Auger spectrum of 4.8ML Co/Cu(111). The typical Co-lines have a minimum at 53eV (not shown), 656eV, 716eV and 775eV. Typical Cu-lines are 60eV (not shown), 776eV, 845eV and 920eV.

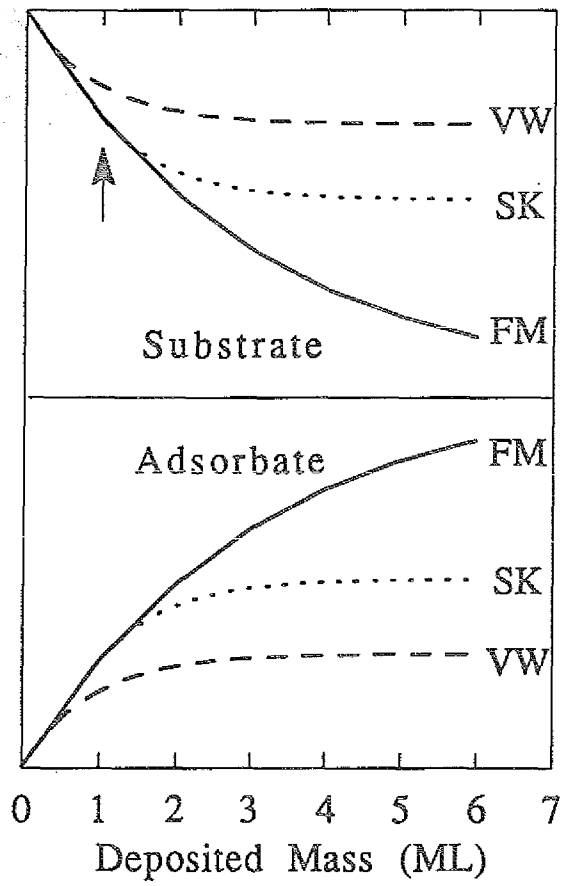

Fig. 4.2: Schematic behavior of the Auger signals of the substrate and adsorbate as a function of the deposited mass in ML for layer-by-layer (Frank van der Merve, FM) growth (solid line), island (Volmer-Weber, VW) growth (dashed line) and layer plus island (Stranski-Krastanov, SK) growth (dotted line). The arrow marks the discontinuity in the slope of the substrate signal after completion of the first layer.

Co has been evaporated at a constant rate while successive Auger spectra were recorded. The axis of the LEED/Auger system was located 45^0 from the sample surface normal to allow in situ evaporation. Due to the fact that the Auger system possesses an acceptance angle of about $\pm 30\%$ electrons are collected that leave the sample at angles of $15 - 75^0$ to the surface normal.

The peak-to-peak height of the 656eV and 716eV peak gives the Co intensity wheras the 850eV and 920eV peak was used for the Cu signal. The peak at 776eV overlaps strongly with the Co 775eV Auger peak and for that reason is not used in the analysis. The evaporation rate was checked with an oscillating quartz crystal thickness monitor and found to be constant. Co films were evaporated at a typical rate of 2Å/min.

As shown in Fig. 4.3a, the Cu signal decreases exponentially and the Co signal increases, following a curve of the form $I_0 \cdot (1 - \exp(-x))$. A comparison with the theoretical reference curves for the different growth modes indicates that in this case Co grows layer by layer on Cu(111).

We compared also the theoretical curves of Volmer-Weber and Stranki-Krastanov growth with the data. In fig. 4.3b the expected Auger curves for island growth (islands cover-

ing 90%, 80% and 70% of the substrate surface) and the expected curve of Frank van der Merve growth (100% (FM)) are compared to the Auger data of the substrate signal (4.3a). The main difference between the data and the expected curves for island growth is the more slow decrease of the substrate Auger signal in the model of island growth. By chosing a shorter IMFP in the theoretical curves we are able to get a reasonable agreement between the island model with islands covering 90% of the surface and the data points but when we try to fit in the same way curves for islands growth with islands covering less than 90% we find these curves are either too flat at higher coverages (6-12ML) or too steep in the low-coverage regime (0-5ML). The same is valid when island growth is considered after one or two complete cobalt layers have formed. Best agreement with the data points can be archieved by fitting an exponential curve.

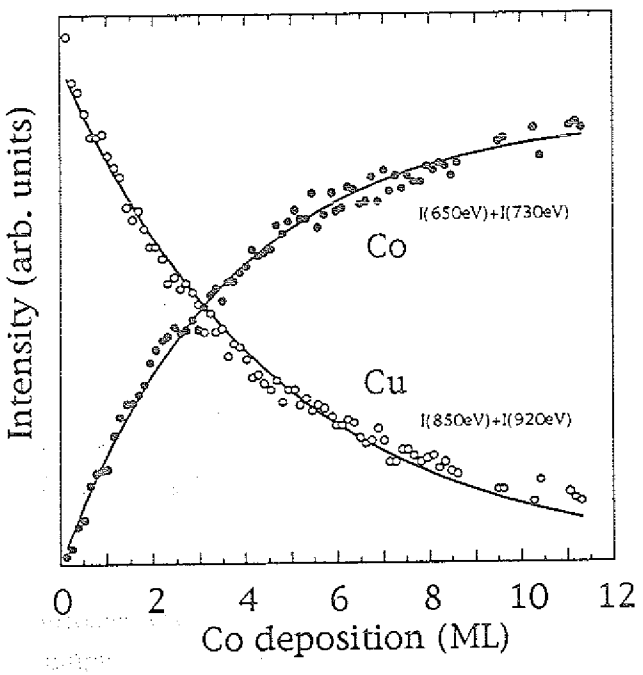

Fig. 4.3a: Auger-signal intensity versus Co coverage. The peak-to-peak height of the 656eV and 716eV line give the Co intensity (open circles) and the peak-to-peak height of the 920eV and 850eV line give the Cu intensity (filled circles)

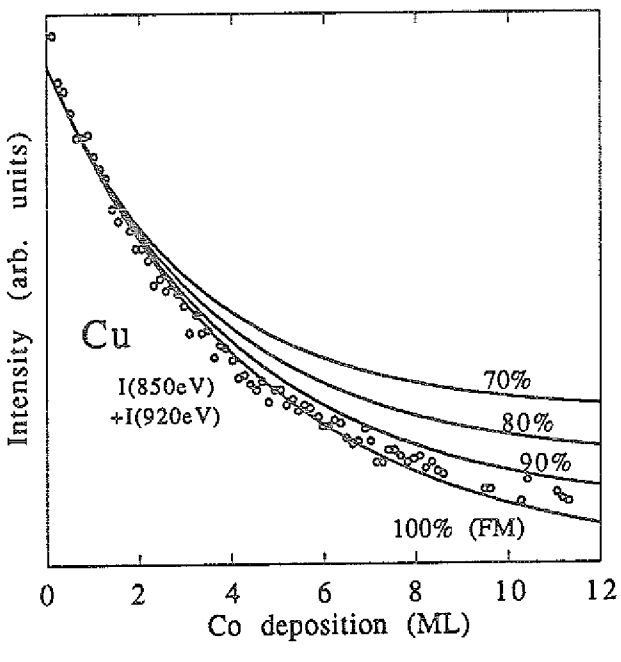

Fig. 4.3b: Auger-signal intensity versus Co coverage. Data points are taken from fig. 4.3a and show the Auger intensity of the Cu substrate. The solid lines represent the expected curves for island growth, islands covering 70%, 80% and 90% of the substrate surface. Frank van der Merve growth corresponds to the curve marked 100% (FM).

A least-squares fit of the expected curve for a layer-by-layer growth to the data is shown as a straight line in fig 4.3a. The IMFP determined from this fit is $\lambda = 13.7 \pm 1.7$Å for the Cu Auger signal whereas $\lambda = 10.4 \pm 1.5$Å for the Co Auger signal has been found. The values for the IMFP's include corrections that arise from the facts that (a) the Auger spectra have been measured off normal (the path length of electrons in the solid is

$1/\cos(\alpha) \cdot d$ where d means the thickness of the cobalt layer and α is the angle between surface normal direction and observation angle) and (b) that the Auger system possess an acceptance angle of about $\pm 30^0$.
In the substrate signal in fig. 4.3a the data points are systematically lower than the fitted exponential curve in the range 2-5ML and systematically higher above 7ML. The origin of this difference is the large acceptance angle of the Auger system. We have calculated the deviations resulting from the large acceptance in the chosen geometry ($\alpha = 45^0$) and found that they exactly cancel the systematical difference between the data points and the fitted exponential curve in fig. 4.3a.
We are not able to resolve experimentally the kinks in the Auger that indicate the completion of the different layers due to the scattering of the data points. Tikhov and Bauer performed a study similar to ours but for the low-energy regime of the Auger spectra (51eV Co line and 63eV Cu line) [Tikhov, priv.]. They studied the growth mode of Co/Cu(111) with the system Co/45ML Cu(111)/Mo(110). The resulting Auger curves reveal a linear dependence of the substrate and the adsorbate Auger signal for the first monolayer but not for higher coverages. One can therefore expect that small deviations from ideal layer-by-layer growth exist that smooth out the kinks and lead to the observed curve form.

We obtained the follwing results about the growth mode of Co on Cu(111):
Co grows on Cu(111) to a good approximation in a layer-by-layer fashion (Frank van der Merve growth) although there are some indications for small deviations from ideal layer-by-layer growth.

4.2 LEED study

One of the most common methods of surface analysis is low-energy electron diffraction (LEED). A parallel beam of electrons having energies ranging from 10-300eV impinges on a crystal and is back-diffracted in directions given by the well known Ewald construction. The diffracted electrons produce spots on a fluorescent screen. Like AES this method is very surface sensitive because the IMFP is below 10Å for electrons in this energy range. LEED can be used to determine qualitatively the structure of the surface. On the screen we see the reciprocal lattice of the two dimensional surface structure of the sample.

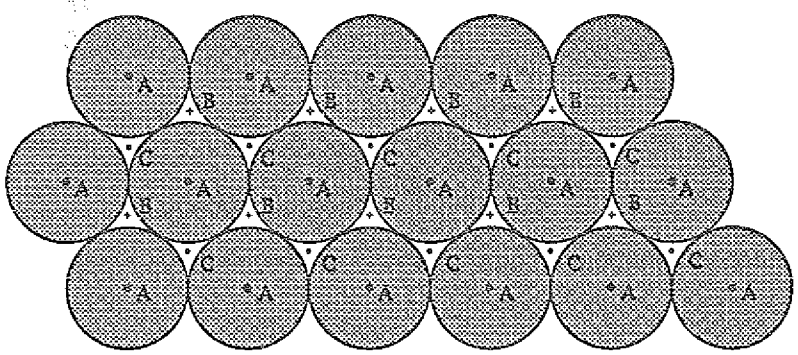

Fig. 4.4: Close packed structures. The atoms of the first layer are marked with an A and the atoms of the second layer are marked with B. If the third layer is identical to the first layer (ABA...) the structure is hcp and the layers are (1000) planes. If the atoms of the third layer occupy the positions C, it is a (111) plane of an fcc structure (ABC...). Taken from [Kittel].

In fig. 4.6 we show LEED pictures of the clean Cu samples and 5.5ML Co on top of Cu(111) for different electron energies. The Cu(111) crystal has sharp spots of three-fold symmetry as can be seen clearly at 127eV electron energy. The six spots at 81eV consists of two sets of three spots with, by coincidence, nearly the same intensity. With Co on top of Cu(111) the spots are nearly as sharp as for the clean Cu. Co grows on Cu in a well ordered fashion, adopting the lattice structure of copper. This result is expected due to the small mismatch in the fcc lattice constants of Co and Cu ($a_{Cu} = 3.61$Å, $a_{Co} = 3.54$Å). As mentioned above, there exist two different Co structures for bulk Co, fcc and hcp, that could possibly grow on Cu. The two structures differ only by the packing sequence of the successive layers. While an fcc crystal has an *abcabc* structure an hcp crystal has an *ababab* structure (see fig 4.4). The LEED pattern for the hcp phase has a sixfold symmetry wheras the fcc phase has, like clean Cu, a threefold symmetry [Lee, 78]. The LEED picture for 5.5ML Co/Cu(111) clearly shows the threefold symmetry of the fcc crystal.

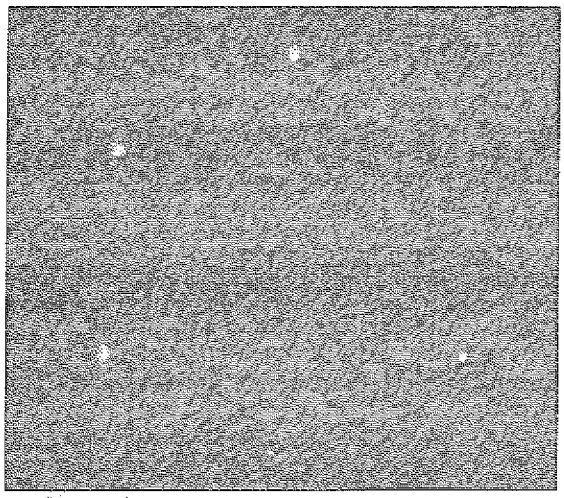

a) clean Cu(111) at 81eV

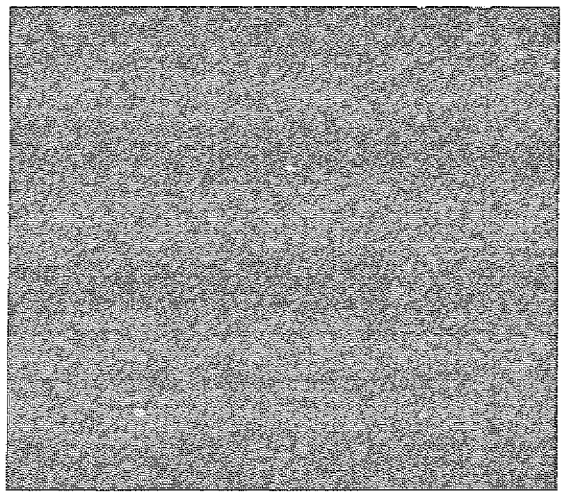

b) clean Cu(111) at 127eV

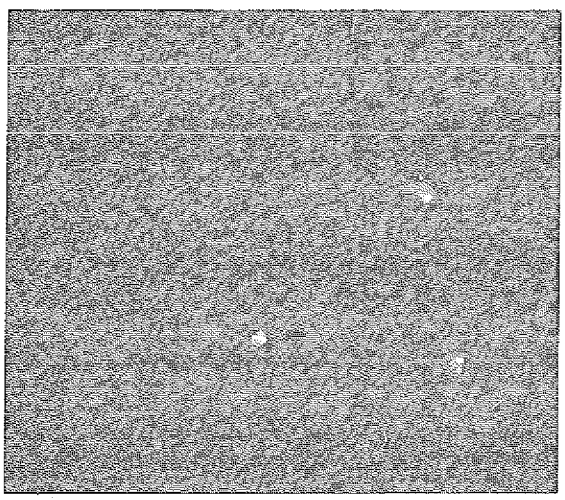

c) 5.5ML Co/Cu(111) at 57eV

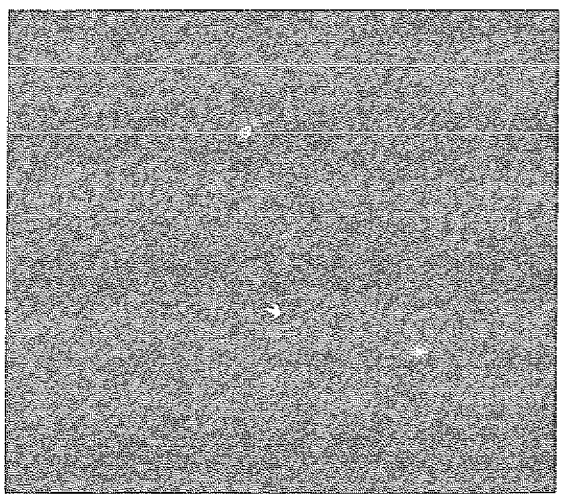

d) 5.5ML Co/Cu(111) at 131eV

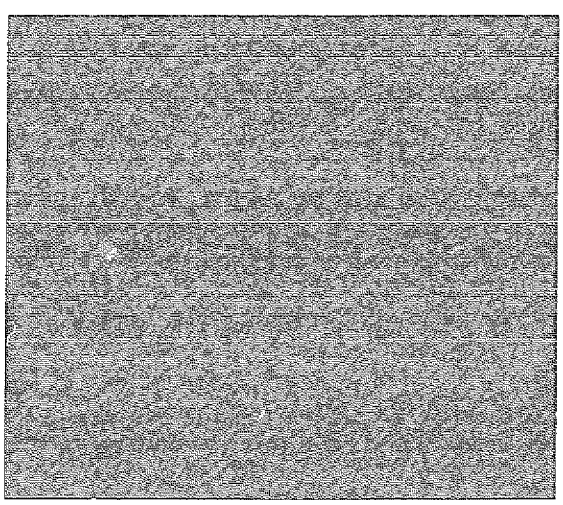

e) clean Cu(100) at 112eV

Fig. 4.5: LEED pattern
of fcc Cu and fcc Co

It is possible that for higher coverages the structure switches to hcp as reported by Gonzalez [Gonzalez, 81], but we found no evidence for this. Furthermore, in the photoemission spectra we did not see any change of the electronic structure between 5ML and higher coverages up to 20ML. For this reason, in the description of the bandstructure that follows, only the bands with fcc symmetry labels are discussed.

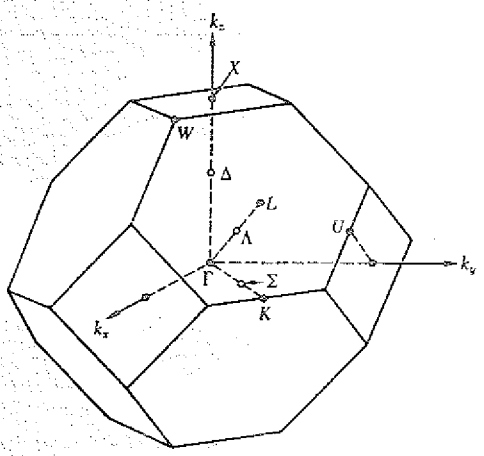

Fig. 4.6: Standard labels of the symmetry points and axes of the Brillouin zones of the fcc lattice. The boundary point at $(2\pi/a)(100)$ is X and the boundary point at $2\pi/a(\frac{1}{2}\frac{1}{2}\frac{1}{2})$ is L. Taken from [Kittel].

4.3 Growth of Co on Cu(100)

The system Co/Cu(100) has been studied much more extensively than Co/Cu(111) [H.Li, 90] [Clarke, 87] [Gonzalez, 81] [Miguel, 89]. Co grows in a well-ordered layer-by-layer fashion on the Cu(100) surface . It adopts the fcc structure of the substrate up to coverages of at least 20ML. Clemens [Clemens, 91] has done a LEED/Auger study for Co/Cu(100) similar to the one we presented for Co/Cu(111). He recorded Auger spectra in the high-energy range of the Auger spectrum (600eV-1000eV). The resulting Auger curve (see fig 4.7) is used in our spectra to calibrate the thicknesses for the Cu(100) surface. Clemens obtained IMFP's for the Co Auger line ($\lambda = 7$Å) and the Cu Auger line ($\lambda = 9$Å) which are significantly smaller than the results of our study on Cu(111). Due to the fact that the (111) surface is the one with the highest atomic density, the different IMFP's cannot be attributed to the different surface planes (That would result in a shorter IMFP for the (111) surface).
Due to the fact that Clemens shows only the ratio of the Co and the Cu+Co Auger signal his fitted curve possesses more parameters for the fit than we do leading to larger uncertanties. We determined an Auger curve for the substrate and the overlayer Auger signal independently. There are only small uncertanties in the initial intensity $I_0^{sub/ads}$ in our study and errors in the determination of the IMFP's must be attributed mainly to uncertanties in the coverage. Beside the differences in the analysis of the data there are also differences in the measurement. By measuring the Auger spectra and evaporating Co at the same time we kept the experimental conditions more constant than Clemens and were able to take much more data points.

Figure 4.5e shows the LEED pattern of clean Cu(100) at 112eV primary electron en-

ergy. The LEED pattern shows the fourfold symmetry of the (100) surface. It remains as sharp and intense as shown in fig. 4.5e for all Co coverages studied in this work, up to about 20ML.

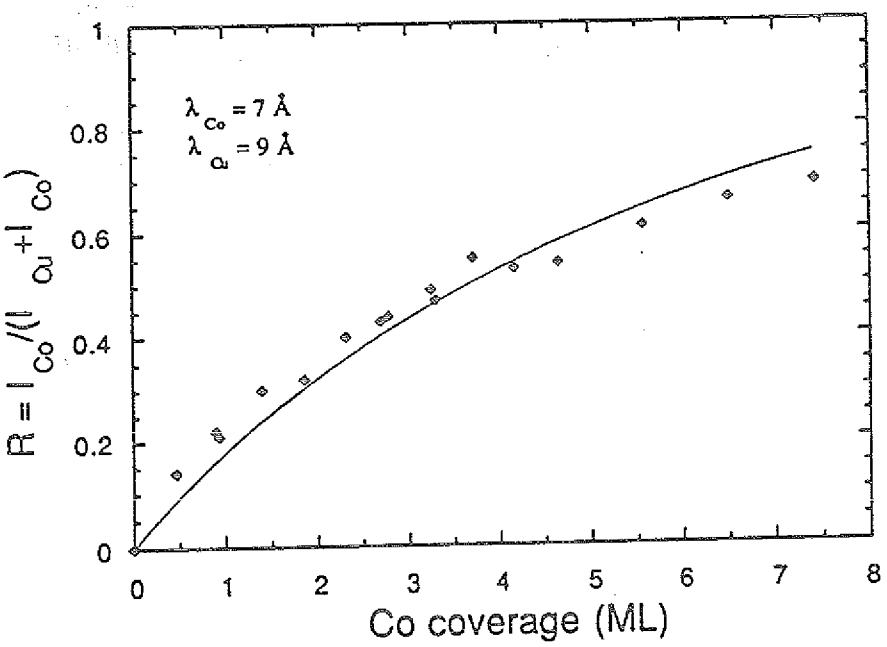

Fig. 4.7: Ratio of the Cobalt to Copper peak-to-peak intensities in the derivative AES spectra $R = I_{Co}/(I_{Co} + I_{Cu})$ as a function of Co thickness (diamonds) on Cu(100). The line shows the expected curve for the layer-by-layer growth mode, taken from Ref.[Clemens, 91]

5 Band Structure

5.1 Band Structure of Cu

In Cu the d shell is filled with 10 electrons and the s shell has 1 electron ([Ar]$3d^{10}4s^1$). The wavefunctions of the 4s electrons show a strong overlap with the 4s wavefunctions of the neighbouring atoms, whereas the 3d wavefunctions are more localized. The localization of the d electrons leads to rather flat d bands with a high density of states. In a solid the 5-fold degenerate d bands split and the band structure shows five different bands. Only in the high symmetry directions, $\Gamma - L$ and $\Gamma - X$, some bands are still degenerate.
Due to the strong overlap of the s wavefunctions the s electrons are itinerant and form a band in the solid that is similar to the parabolic bands characteristic of free electrons.
The pure character of s and d bands is lost where these bands cross. Due to hybridization, they form sd bands.
The density of states for Cu is shown in fig. 5.1 and fig. 5.3 shows a theoretical calculation by Burdick [Burdick, 62]. The high density of states 2-4eV below E_F and the strong structures are a direct result of the small dispersion of the d bands.

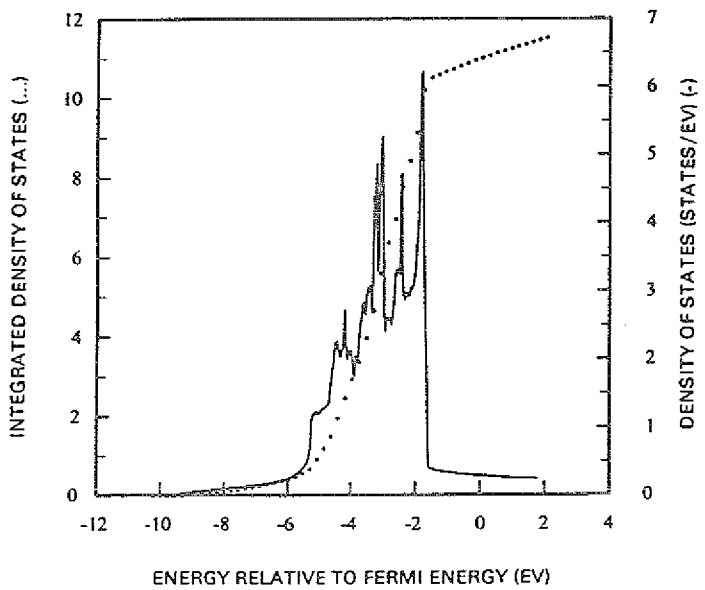

Fig. 5.1: Density of states for Cu [Moruzzi, 78]

With clean Cu(111) and (100) crystals we have mapped the band structure in the Γ-L and Γ-X directions for the fcc Brillouin zone respectively
We took photoemission spectra with the direction of the incident light and the direction of the emitted electrons parallel to the surface normal direction (s-polarized light/normal emission). The spectra for Cu(100) are shown in fig. 5.2a and for Cu(111) they are shown in fig. 5.2b.
Symmetry and selection rules restrict our observation in this geometry to bands of Δ_5 symmetry in (100) direction and to bands of Λ_3 symmetry in (111) direction (see table 1, page 2.5).

After excitation we assume that the electrons are in a final state which can be described by a free-electron parabola

$$E_f(\mathrm{k}) = \frac{\hbar^2 \mathrm{k}^2}{2m} + V_0 \qquad \text{with} \quad m = m_e \quad \text{electron mass} \tag{40}$$

with the constant inner potential V_0. The inner potential can be determined with emission from a high symmetry point (see chapter 2.2).

For the (100) direction only one band of the observable Δ_5 symmetry exists along $\Gamma - X$ in the calculation. Emission from this band corresponds to the peak labeled A in fig. 5.2a. Between 10eV and 45eV photon energy this peak shifts from 2.3eV to 3.5eV binding energy. At 45eV photon energy the binding energy of this peak has reached a maximum and with increasing photon energy shifts back to smaller binding energy.

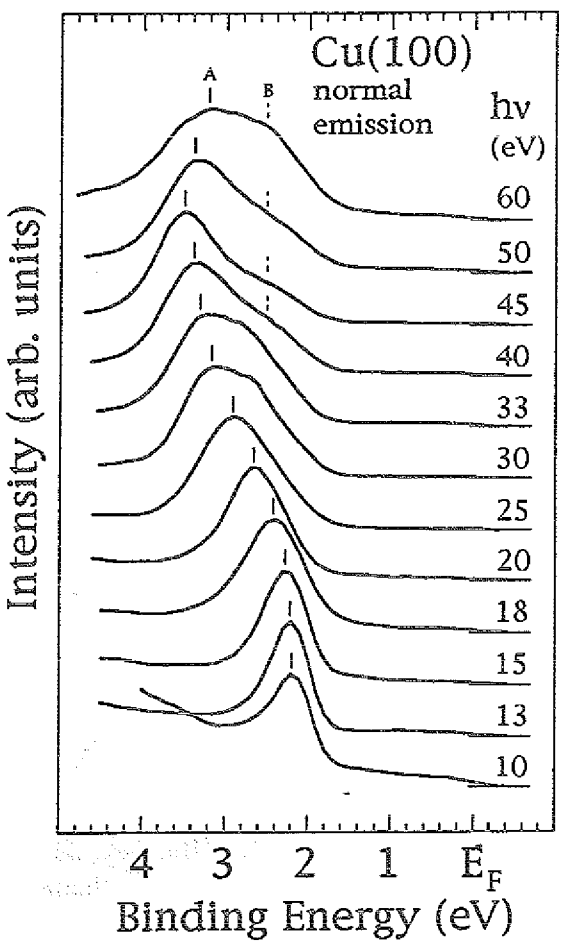

Fig. 5.2a: Spin-integrated photoemission spectra of Cu(100), taken in normal emission with s-polarized light of different photon energies

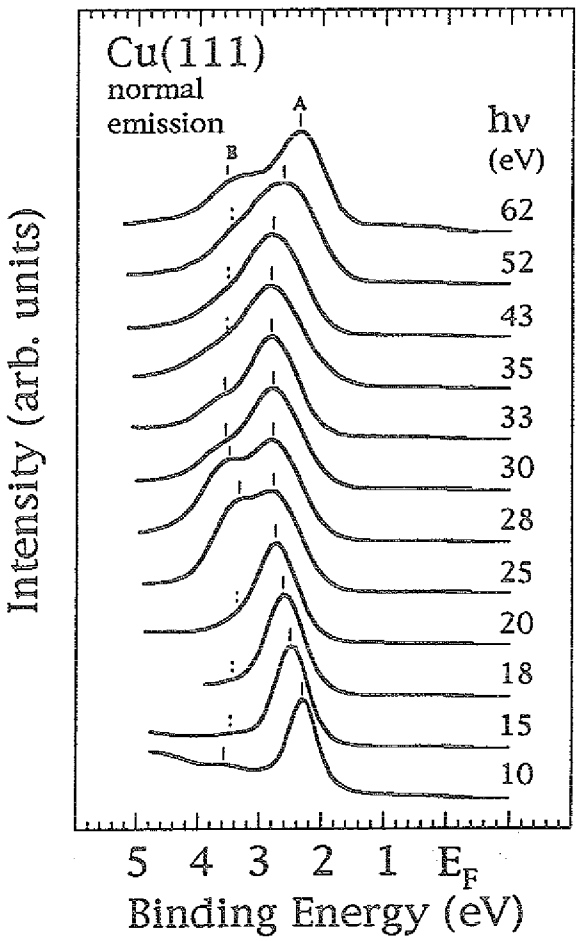

Fig. 5.2b: Spin-integrated photoemission spectra of Cu(111), taken in normal emission with s-polarized light of different photon energies

The extremum of the binding energy corresponds to emission from the high-symmetry

Γ-point.
With the photon energy $h\nu = 45eV$ and the binding energy $E_i = 3.5eV$ in the extremum we get the energy of the final state $E_f = h\nu - E_i = 41.5eV$. The k point that corresponds to Γ in the second Brillouin zone is $|k| = 2\pi/a_{Cu} = 3.48\text{Å}^{-1}$. With eqn. 40 an inner potential of $V_0 = -5eV$ is obtained.
With the knowledge of the inner potential we can use eqn. 26 to determine the dispersion of the observed bands. The dots in fig. 5.3 between Γ and X show the dispersion of feature A in fig. 5.2a. Filled circles correspond to wave vectors k in the second Brillouin zone and open circles correspond to wave vectors in the third Brillouin zone. The size of the points corresponds to the error bars ($\pm 0.1eV$). The dispersion of this band is in good agreement with the calculated Δ_5 band.
A second feature B can be seen in the (100) direction at photon energies above 30eV. This shoulder at 2.5eV binding energy has been interpreted as Umklapp processes involving transitions of the Δ_5 band near the X-point [Clemens, 91].

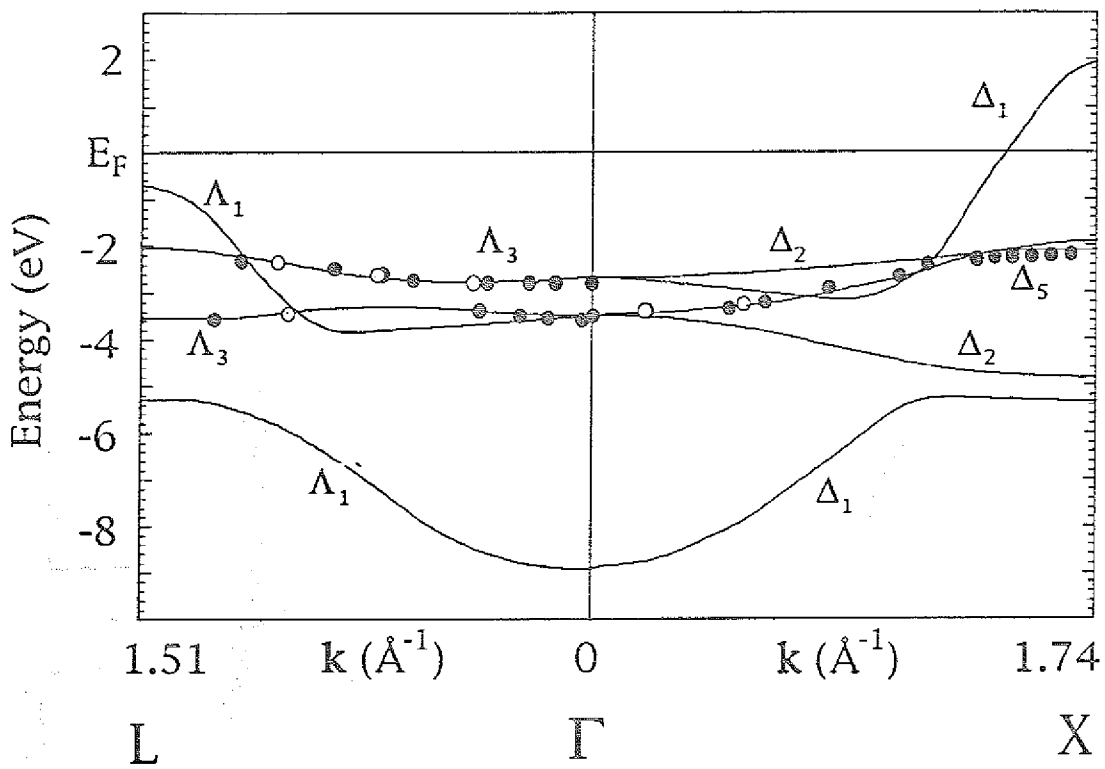

Fig. 5.3: Band structure of Cu in Γ-L and Γ-X direction after Burdick [Burdick, 62]. Filled (empty) dots show experimental determined points in the second (third) Brillouin zone

In the (111) direction most of the spectra show two structures, marked A and B in fig. 5.2b, that belong to the two different Λ_3 bands. The upper Λ_3 band (A) shows a strong emission in all spectra, while the lower Λ_3 band (B) in some spectra is hardly visible. With the free-electron parabola final state determined above it is possible to map the band structure in the same way as on the (100) surface. Due to the fact that along

the (111) direction the Γ point in the second Brillouin zone has a different |k| value than along the (100) direction, we get with eqn. 40 different final states. As a result we observe a symmetry point in the photoemission spectra at different photon energies. For example emission from Γ in the second Brillouin zone is found at $h\nu = 33eV$ on Cu(111) instead of 45eV on Cu(100).

The experimental points as obtained from fig. 5.2b are compared to the Λ_3 bands of the calculation and both are shown in fig. 5.3.
Emission from the second (third) Brillouin zone is printed with filled (empty) circles. We find a good agreement with the band structure calculation in the (111) direction as we did for the Δ_5 band in the (100) direction.

Due to the fact that clean Cu is easy to prepare and serves as a substrate for many different materials, it has been studied extensively by other groups.
In the classical work of Thiry [Thiry, 81] the band structure of Cu has been determined along several high-symmetry directions with photoelectron spectroscopy. His results can be directly compared to our measurements. He found a very good agreement with the calculations of Burdick [Burdick, 62] as we did. Due to the fact that he used p-polarized light he was able to study also bands of other symmetries whereas we are restricted to the observation of Λ_3 and Δ_5 bands.
Jona [Wu, 91] presented spectra of Cu(111) that were taken with a much better resolution and compared the results to a relativistic band-structure calculation. He was able to resolve fine structures that were predicted by the relativistic calculation and that were not seen in the spectra of Thiry. With the exception of the better resolution Jona's data showed the same band dispersions as the one of Thiry.
We find a good agreement between our measurements and the work of these groups for the observed bands.
As Thiry, we are not able to resolve the fine structures, predicted by the relativistic calculation, but a comparison with the calculation of Burdick [Burdick, 62] (fig. 5.3) shows that experiment and theory agree quite well.

5.2 Band Structure of Co

Since Co is a ferromagnet, the band structure for the two different spin directions, majority and minority, is not the same. In fig. 5.4 and 5.5 we show the results of a spin-dependent band-structure calculation for the high-symmetry directions Γ-L and Γ-X of fcc Co with the lattice constant of Cu done by Noffke [Noffke, priv.].

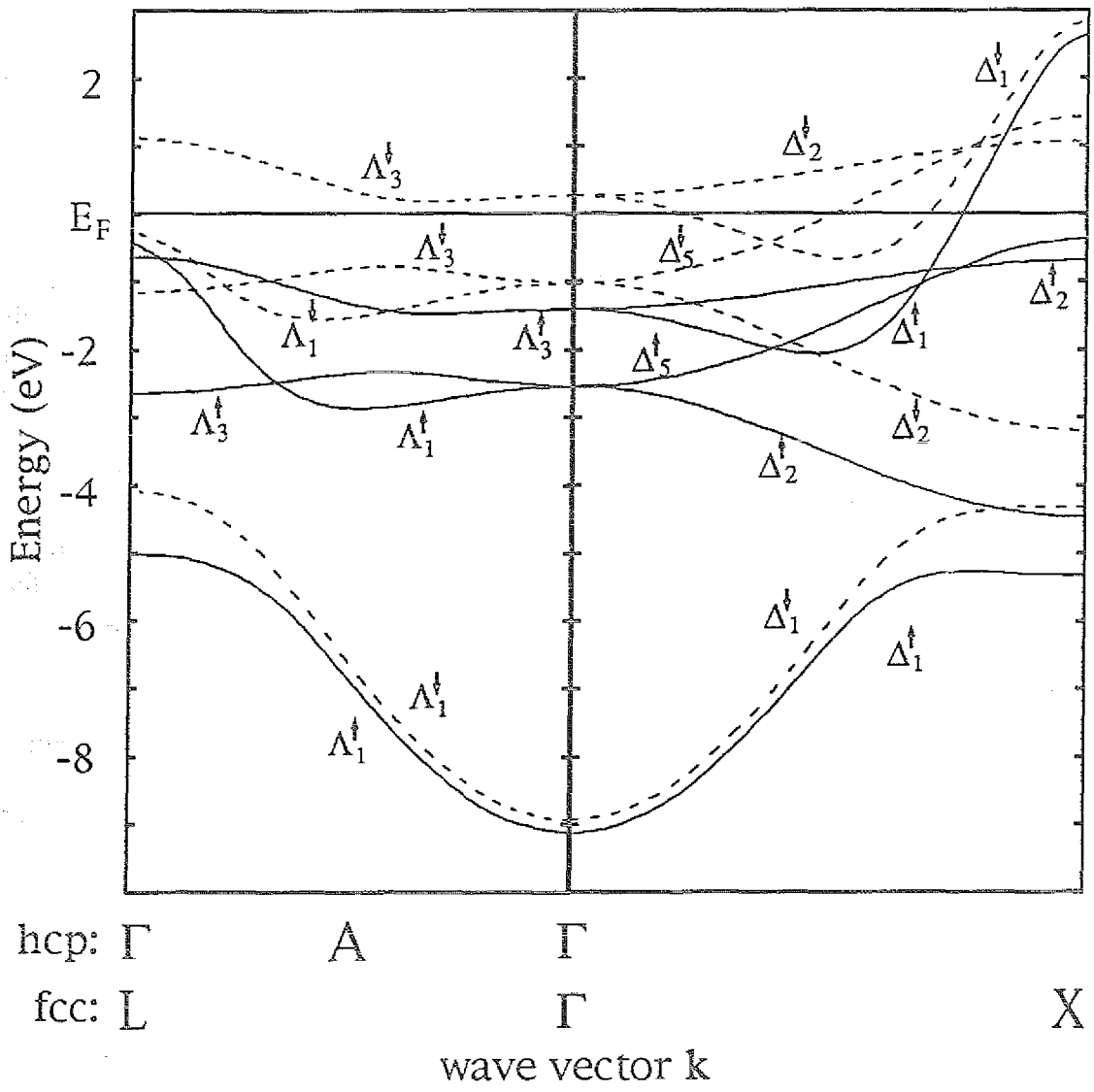

Fig. 5.4: Band structure of Co in Γ-L direction after Noffke [Noffke, priv.].

The minority bands (dotted lines) and the majority bands (full lines) have a similar shape, but the minority bands are located at a higher energy. At Γ the exchange splitting of the Δ_5 bands was calculated to be $\Delta E_{ex} = 1.55eV$.
In this study we have mapped the band structure in the Γ-L direction only. For comparison we show some results for the Γ-X direction that had been obtained previously [Clemens, 91] [Clemens, 92].

For magnetic materials, in addition to E and k, the spin of the emitted electrons becomes an important quantum number. For bandmapping it can be of great importance to distinguish between majority- and minority-spin directions when peaks overlap or can not be clearly identified.

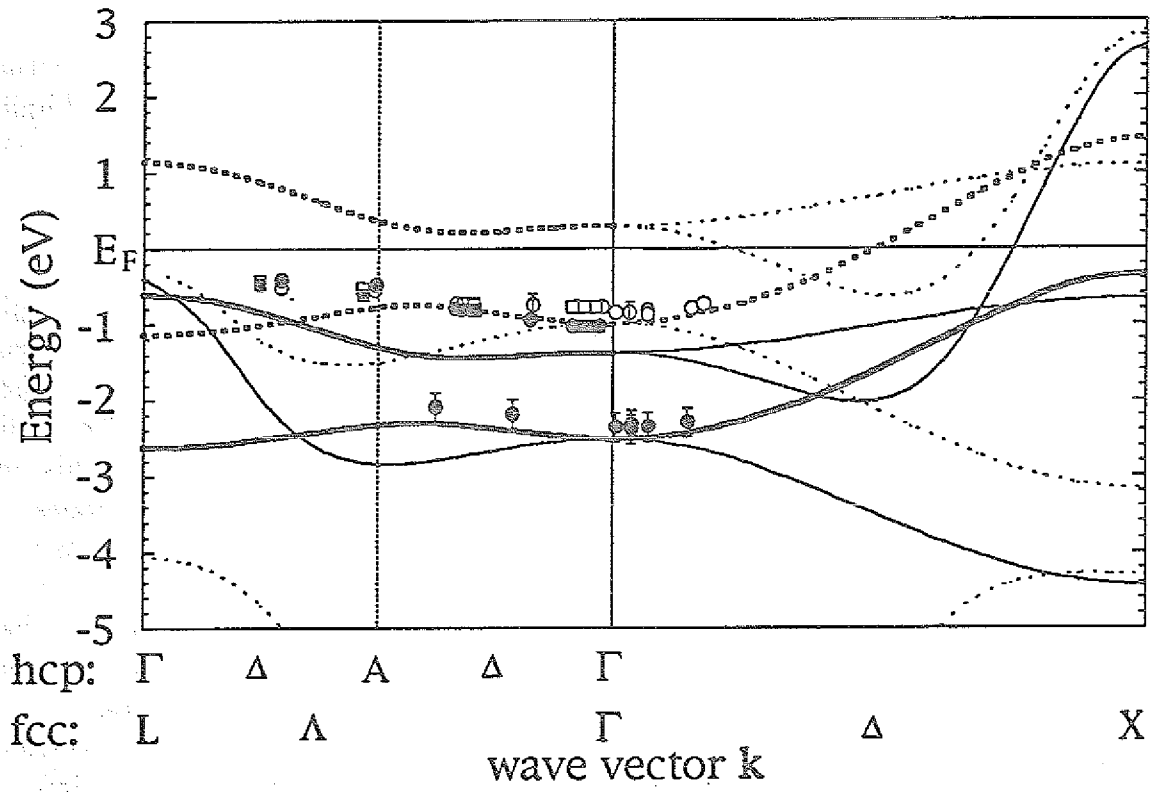

Fig. 5.5: Band structure of Co after Noffke [Noffke, priv.]. Filled (empty) points show experimentally determined structures of minority- (majority-) spin character. Circles are used for structures in the second brillouin zone, squares for the third. Bands of Λ_3 symmetry in the Γ-L direction and bands of Δ_5 direction in the Γ-X direction are printed with a bold line

Unfortunately spin-resolved spectra are much more time consuming than comparable spin-integrated spectra. There is a factor of 10^{-3} in signal intensity when comparing spin-integrated spectra, shown in fig. 5.7 to the spin-resolved spectra in fig. 5.6. The spin-resolved spectra shown here require 1-2 hours to obtain, but are necessary since spin-integrated spectra alone do not provide much information about the band structure of cobalt on copper.

All the spectra shown in this chapter, the spin-resolved in fig. 5.6 and the spin-integrated in fig. 5.7 are taken with s-polarized light in normal emission. As for Cu, we can observe in this geometry only bands of Λ_3 symmetry in the $\Gamma - L$ direction and bands of Δ_5 symmetry in the $\Gamma - X$ direction.

Clemens [Clemens, 91] has previously studied the band structure in the $\Gamma - X$ direction with spin-resolved photoemission of Co/Cu(100). We extent this work to a study of the

$\Gamma - L$ direction with Co/Cu(111).
We use the same free-electron final state as previously [Clemens, 91], with an inner potential of $V_0 = -5eV$ (eqn. 40). The inner potential has been determined with emission from the high-symmetry Γ point, in the same way as for Cu.
The free-electron parabola final state is in good agreement with final states calculated by Noffke [Noffke, priv.].
In this chapter we show films with 10-30ML Co on Cu. Some spectra still show structures at about 2.5eV binding energy that originate from the Cu substrate. But the binding energy of the adsorbate-induced peaks does not change with coverage for more than 5ML Co/Cu(111). For that reason we can expect that the band structure, determined with 10-30ML Co/Cu, is the same as for bulk fcc Co.

In fig. 5.6 we show spin-resolved photoemission spectra for different photon energies. With a photon energy of 10eV we see emission near the L point of the fcc Brillouin zone and emission from Γ can be seen with $h\nu = 31eV$. The spin-resolved spectra show a peak near E_F for every photon energy in the minority spin channel. At $h\nu = 10eV$ the binding energy of this peak is 0.4eV. With increasing photon energy the intensity of this peak goes up and the binding energy shifts to 0.7eV (see 28eV and 33eV photon energies). At 25eV the minority peak is the main feature in the spectrum. When the photon energy is increased above 33eV the peak shifts back towards E_F and the intensity goes down.
The corresponding exchange-split majority band is located 1.5eV below the minority band at a binding energy of about 2.1eV. Emission from this band can be seen only in the spin-resolved spectra at $h\nu = 20eV$ and $25eV$ (marked with a dashed line). To separate the peak from the background, we have subtracted in the curve of the majority electrons a spectrum of the shape of the curve of the minority electrons. The exact form and intensity of the subtracted spectrum changes the majority peak position slightly.
With this procedure we have determined the exchange splitting as $\Delta E_{ex} = (1.4 \pm 0.2eV)$. This value can be compared to the exchange splitting that has been determined on the (100) surface at Γ ($\Delta E_{ex} = 1.55 \pm 0.2eV$) by Clemens [Clemens, 92]. The results agree within the uncertainty of the measurement.
A second peak in the majority spin of fig. 5.6 is present at all photon energies. This structure near E_F corresponds to the upper Λ_3 band. This band shows a stronger dispersion than the other Λ_3 bands.

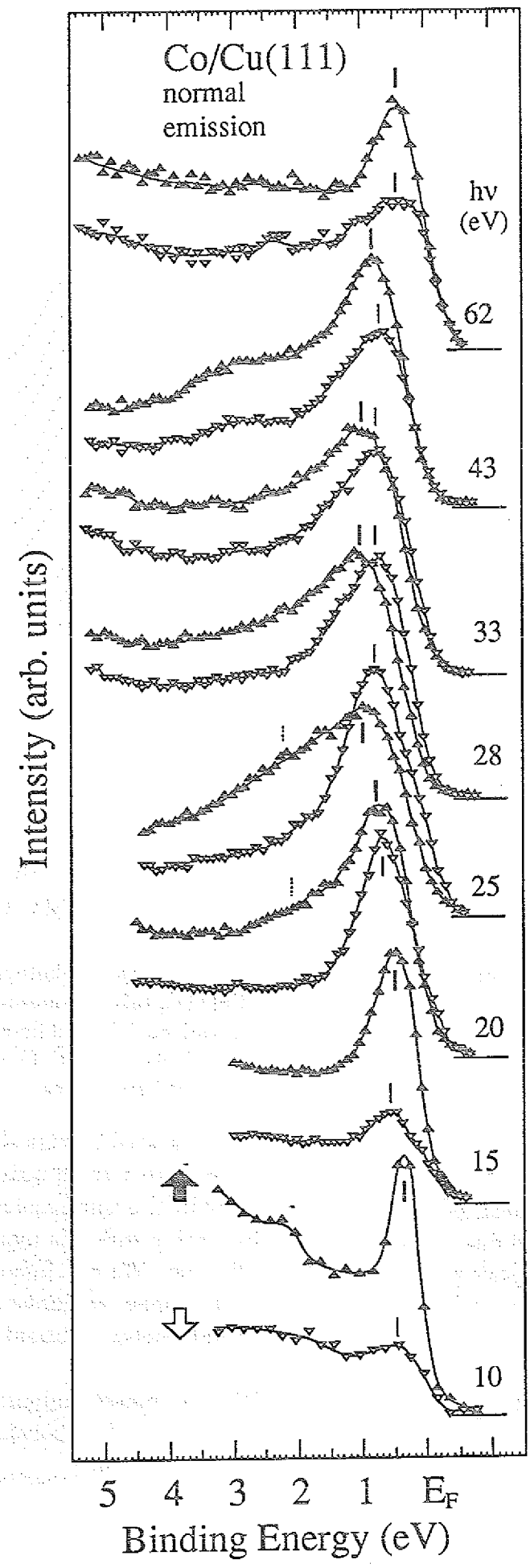

Fig. 5.6: Spin-resolved photoemission spectra of Co/Cu(111), taken in normal emission with s-polarized light of different photon energies. △ and ▽ are used for majority and minority spin directions.

It crosses the minority band at 18eV photon energy and has a maximum binding energy of 1eV at Γ ($\Gamma_{12}^{\uparrow} = 1.0 \pm 0.1eV$).

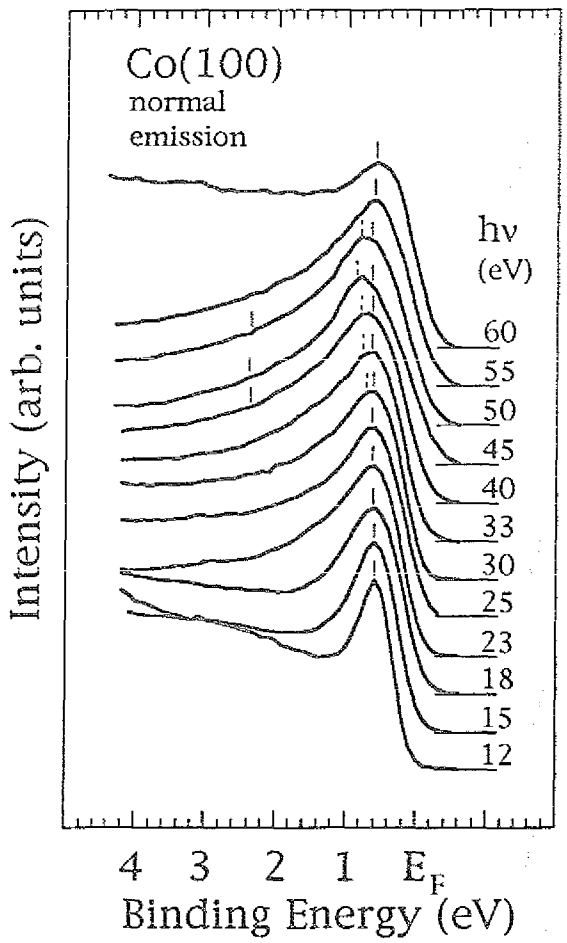

Fig. 5.7a: Spin-integrated photoemission spectra of Co(100), taken in normal emission with s-polarized light of different photon energies. Broken (solid) lines mark minority (majority) structures.

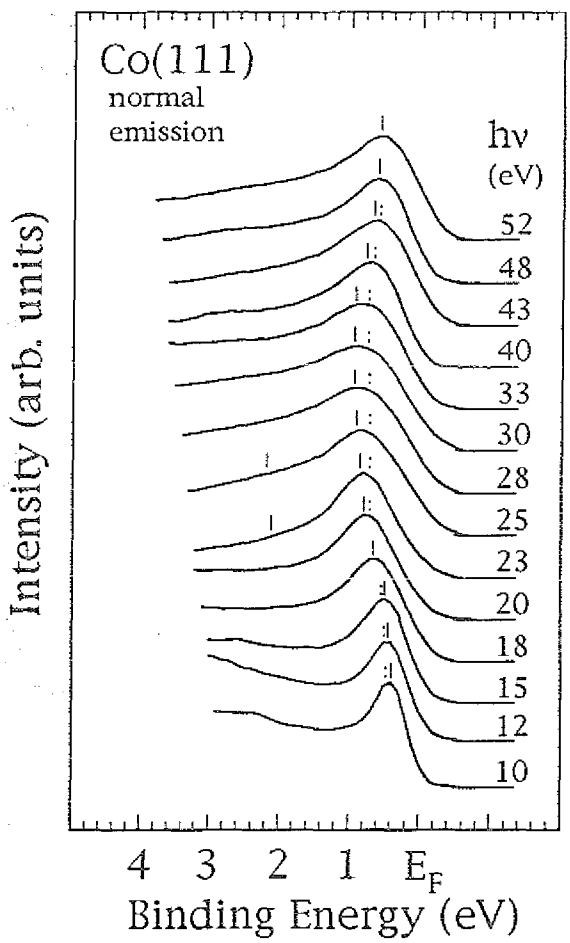

Fig. 5.7b: Spin-integrated photoemission spectra of Co(111), taken in normal emission with s-polarized light of different photon energies. Broken (solid) lines mark minority (majority) structures.

The dispersion of the Λ_3 bands can also be seen in the spin-integrated spectra shown in fig. 5.7b. The spin-integrated spectra do not resolve the different structures near the Fermi edge, but when we mark the peak positions as obtained with the spin-resolved spectra, it is possible to follow the band dispersion. The minority-peak position is marked with a broken line and the majority peak is marked with a solid line. We can follow the weak dispersion of the lower minority Λ_3 band, the crossing of the upper majority Λ_3 band at about 18eV photon energy and the extremum in the binding energy at about 25-30eV is also evident.

Figure 5.7a shows spin-integrated spectra of Co(100). We have marked minority and majority peak positions as in fig. 5.7b. As a reference we used the spin-resolved spectra of Clemens.

The spectrum at 60eV photon energy shows a broad structure in the background that originates from a MNN Auger decay of Co.
A comparison between theory [Noffke, priv.] and experiment is given in fig. 5.5. In the $\Gamma - X$ direction a few points are plotted that correspond to measurements on Co(100) done by Clemens.
The points in the $\Gamma - L$ direction show our results on Co(111). Best agreement between experiment and theory can be found near Γ. We have determined an exchange splitting of $\Delta E_{ex} = 1.4 \pm 0.2eV$ near Γ that agrees within the error bars with the theory and the results on Co(100). The binding energy of the upper majority Λ_3 band at the Γ point is $\Gamma_{12}^{\uparrow} = 1.0 \pm 0.1eV$ and the binding energy of the lower minority Λ_3 band at Γ is $\Gamma_{25}^{\downarrow} = 0.7 \pm 0.1eV$.

In this work spin- and angle-resolved photoemission has been applied for the first time to study the bandstructure of Co(111).
Angle-resolved photoemission without spin information was used already by Himpsel to determine the bandstructure of hcp cobalt [Himpsel, 80]. He studied the (0001) surface of a single crystal of cobalt and compared the data to a self-consistent calculation [Moruzzi, 78]. Due to the fact, that the (0001) surface of the hcp phase is very similar to the (111) surface of the fcc phase, the same band-structure calculation can be used for the directions $\Gamma - A - \Gamma$ (hcp) and $\Gamma - L$ (fcc). Only the symmetry labels differ. Himpsel's spectra can be directly compared to our spectra.
At the Γ point he reported an energy difference between the minority Λ_3 band ($\Gamma_{25}^{\downarrow}$) and the upper majority Λ_3 band ($\Gamma_{12}^{\uparrow}$) of $\Delta E_1 = 0.1eV$. He was not able to directly resolve the two peaks at 1eV and therefore used the result of a decomposition to determine the peak positions.
The spin-resolved spectra in fig. 5.6 show that the energy difference at Γ between these two bands is clearly larger than reported by Himpsel (see spectrum at $h\nu = 28eV$). We find an energy difference of $\Delta E_1 = 0.3eV$ that agrees much better with the theory.
Himpsel resolved a sharp peak close to the Fermi energy ($E_B = 0.3eV$) in a spectrum taken in normal emission with s-polarized light of 25eV photon energy. In the spin-resolved 25eV spectrum in fig. 5.6, recorded under the same conditions, we find the corresponding structure in the minority spectrum, as predicted by Himpsel. There is a small shoulder near E_F that can hardly be seen.
Assuming that this structure originates from the upper Λ_3 minority band, although calculations predict that this band is above E_F, Himpsel concluded an exchange splitting of $\Delta E_{ex} = 1.0eV$ at Γ (he took the average of the exchange splitting of the upper d band (0.85 ± 0.2 eV) and the lower d band (1.2 ± 0.3 eV)) which is much to small.
With an exchange splitting of $\Delta E_{ex} = 1.4eV$ for the lower d bands at Γ, determined in this work, we locate the upper minority band about 0.4eV above E_F. Possibly we see emission from a tail of this state that reaches below E_F and produces the observed structure although the maximum is located above the Fermi energy. A determination of the binding energy must fail in that case.
Due to the fact that calculations, as recently done by Li [C.Li, 91], reveal surface states

(see chapter 6) on the (0001) surface of hcp cobalt, they must also be considered as a possible explanation for the structure near E_F. Acording to this calculation we can expect surface states at Γ in both spin directions, at about 2eV binding energy in the majority-spin direction and close to the Fermi level, at about 0.5eV, in the minority-spin direction. Himpsel [Himpsel, 79] found a surface state of Λ_1 symmetry at 0.3eV binding energy on Co(0001). The Λ_1 surface state is very sensitive to contamination with hydrogen and can be seen, due to its symmetry, only with p-polarized light.
However, this does not rule out the possibility of a surface state of Λ_3 symmetry that may appear in the spectra that were taken with s-polarized light.
The dispersion of the Λ_3 bands as determined by Himpsel, further away from Γ is similar to our results. The dispersion of the bands does not agree with the theory. The main difference is, as our spin-resolved spectra show, that the energy difference between the Λ_3 minority band and the upper Λ_3 majority band is much smaller than predicted (see fig. 5.5). For k values further away from Γ, where a difference between these bands of about 0.6eV is given in the calculation, we find that the two bands are nearly degenerate.
A possible explanation for the reported differences between theory and experiment, including the fact that all the observed d bands are more close to E_F than predicted, can be given in terms of many-body effects.
Due to the fact that only the ground state of a system is determined in a calculation whereas an excited system with electron-electron correlations is studied in the experiment, differences between theory and experiment are expected.

The measurements that were done by Clemens with spin-resolved photoemission [Clemens, 91] [Clemens, 92] on Co(100) are in good agreement with the results presented here. Due to the fact that he studied a different high-symmetry direction of the crystal, we can compare only the results at the Γ point.
He found an exchange splitting of 1.55eV between the spin-split Δ_5 bands at Γ, that is slightly higher than our value of 1.4eV. The difference can certainly be attributed to errors in the determination of the peak position of the weak majority peak of the lower Λ_3 band. In addition we have determined the binding energy of this peak not exactly at Γ, because no emission from the lower Λ_3 majority band can be seen in the corresponding spectra. This gives an additional uncertainty to our value.

As a result of this study we find at the Γ point that the energy difference between the upper majority Λ_3 band and the lower minority Λ_3 band ($\Delta E_1 = 0.3eV$) and the exchange splitting ($\Delta E_{ex} = 1.4eV$) agree with theoretical calculations.
We find the d bands more close to the Fermi level (0.3eV at Γ) than predicted in the calculation. These differences can be explained by many body effects.
The dispersion of the Λ_3 bands does also not agree with the calculation. As one goes further away from Γ one finds that a minority band and a majority band that should show a difference in energy of about 0.6eV are nearly degenerate.

6 Two-Dimensional Systems

Until now, we have discussed the electronic structure of three-dimensional systems. The band-structure calculations of Co and Cu, shown in chapter 5, have been done for infinite periodic three-dimensional crystals. Boundary effects have not been taken into account although it has been mentioned several times that photoemission spectroscopy is very sensitive to the surface of our samples.
In reality it turns out, that the presence of a surface can influence the wavefunctions of the bulk and produce completely new states at the surface, called *surface states.*
Surface states are states at the two-dimensional surface and can be characterized by the quantum numbers E and $k_{||}$. In contrast to bulk states they are independent of $k_{\perp}$. Surface states cannot mix with any bulk states, they must lie in a band gap of the projection of the bulk states onto the surface.
A state of the same kind that mixes with bulk states is called a *surface resonance.* It does not lie in a gap of the projected bulk bands and can extent into the bulk.
To identify surface states in angle-resolved photoemission, there exist three criteria [Plummer, 82]:

1. The energy E and parallel momentum $k_{||}$ of the state must lie in a gap in the projection of the bulk band structure onto the surface brillouin zone. These projections must consider the symmetry of the bulk state.

2. The binding energy of the peak must be independent of the exciting photon energy for a fixed $k_{||}$.

3. The peak that is caused by a surface state or surface resonance should be sensitve to the perfectness and cleanliness of the surface.

Surface states have been reported for Cu as well as for Co. A surface state near E_F, that lies in the surface brillouin zone of Cu(111) cannot be seen in our geometry (s-polarized light) due to the fact that the state is of the wrong symmetry. It can be seen with p-polarized light only. The same is true for the surface state on Co(111) which has been observed by Himpsel [Himpsel, 79].
Another two-dimensional system that is expected to show a similar k dependence as a surface state can be found when ~1ML adsorbate is grown epitaxially on a substrate crystal and the interaction with the substrate is weak. When the adsorbate grows epitaxially on the substrate, the periodicity within the surface is conserved and the parallel component of the momentum $k_{||}$ is still a good quantum number.
Normal to the surface a single monolayer does not show any periodicity. As a consequence, structures, that arise from the single adsorbate layer, should not depend on $k_{\perp}$.
Due to the fact that the monolayer at the surface of the sample has a different coordination number Z and a different chemical surrounding compared to the bulk, one can expect additional changes in the electronic structure. For the single layer the wavefunctions have a smaller overlap and the electrons are more localized. As a result the adsorbate atoms of the 2D system have a more free-atom like character with an enhanced magnetic moment.

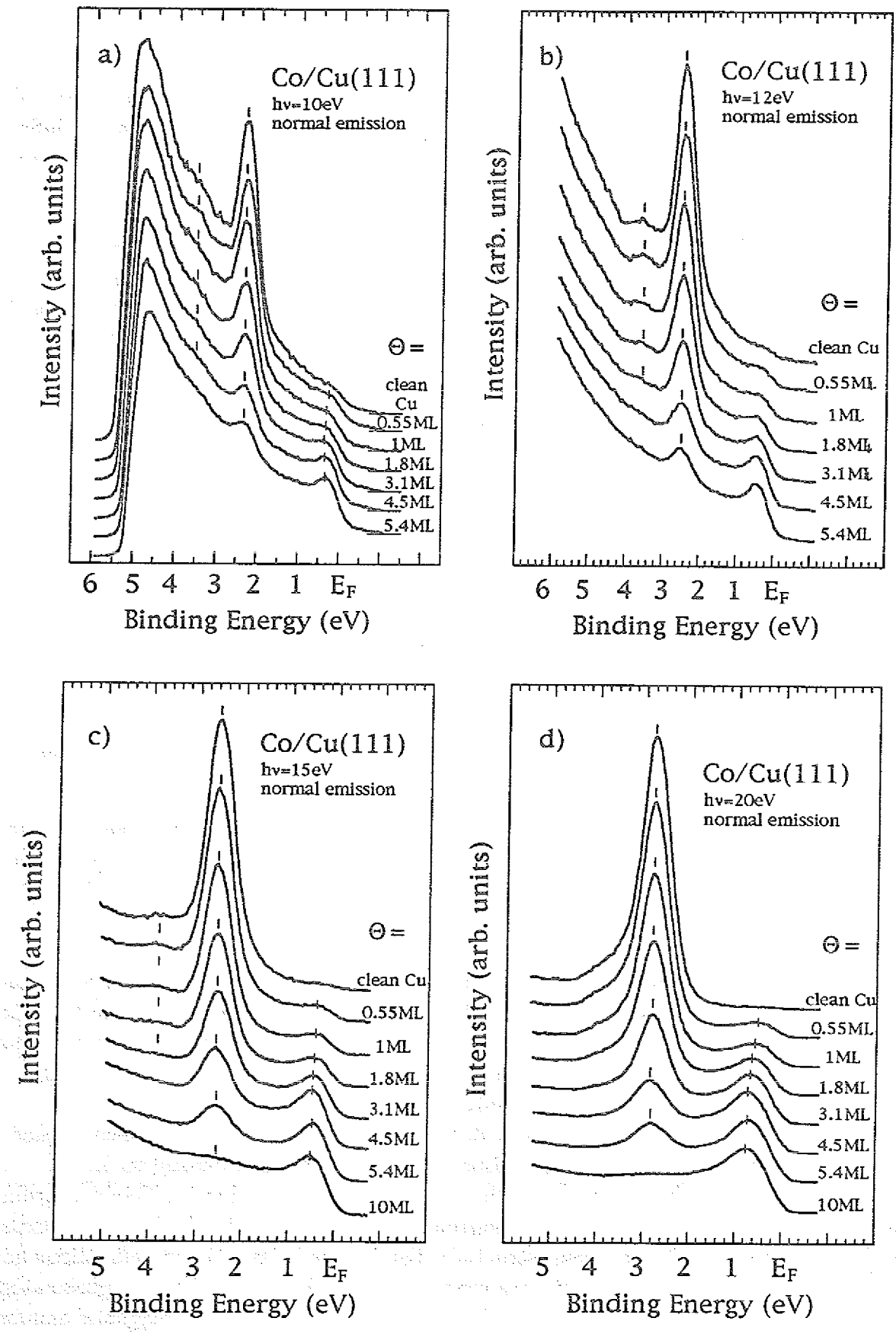
a)
Co/Cu(111)
hv=10eV
normal emission
Θ =
clean Cu
0.55ML
1ML
1.8ML
3.1ML
4.5ML
5.4ML
Intensity (arb. units)
6 5 4 3 2 1 E_F
Binding Energy (eV)
b)
Co/Cu(111)
hv=12eV
normal emission
Θ =
clean Cu
0.55ML
1ML
1.8ML
3.1ML
4.5ML
5.4ML
Intensity (arb. units)
6 5 4 3 2 1 E_F
Binding Energy (eV)
c)
Co/Cu(111)
hv=15eV
normal emission
Θ =
clean Cu
0.55ML
1ML
1.8ML
3.1ML
4.5ML
5.4ML
10ML
Intensity (arb. units)
5 4 3 2 1 E_F
Binding Energy (eV)
d)
Co/Cu(111)
hv=20eV
normal emission
Θ =
clean Cu
0.55ML
1ML
1.8ML
3.1ML
4.5ML
5.4ML
10ML
Intensity (arb. units)
5 4 3 2 1 E_F
Binding Energy (eV)

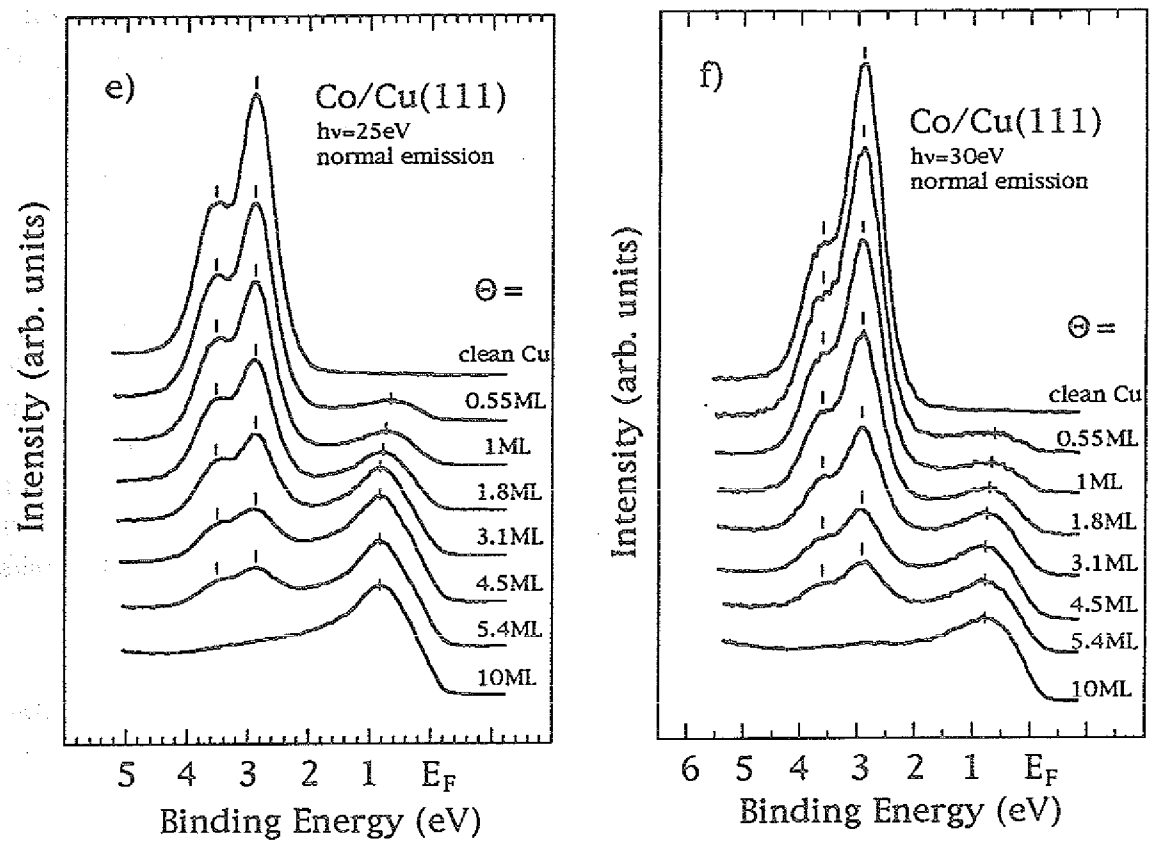

Fig 6.1a-f: Spinintegrated photoemission curves of 0-10ML Co on Cu(111) for different photon energies taken in normal emission with s-polarized light. The spectra are normalized to the photon flux on the sample.

Co deposited on Cu(100) or Cu(111) substrates represents a good system to study the differences between a two-dimensional system and the bulk. Co grows epitaxially on Cu in both cases and shows only a weak interaction with the substrate.
In Fig. 6.1a-f we present a series of spin-integrated photoemission spectra for different Co coverages at photon energies ranging from 10eV to 30eV. The spectra are taken in normal emission with s-polarized light. Selection rules restrict our observation to emission from Λ_3-symmetry states. This time the spectra are normalized to the photon flux on the sample. That allows one to compare the intensity of spectra with different Co thicknesses, taken at the same photon energy. The intensity of spectra that were taken with different photon energies cannot be compared, because the transmission function of the analyser changes with electron energy.
The topmost spectra have been measured with the clean Cu(111) crystal. They show the dispersion of the Λ_3 bands in Cu that has been discussed previously in chapter 5. A photon energy of 10eV corresponds to emission near the L-point and $h\nu = 30eV$ corresponds to emission near Γ.

With increasing Co coverage the intensity of the Cu peaks goes down, following an exponential function. The decrease of the substrate signal can be seen in a similar way in

all spectra of fig. 6.1. That it follows an exponential decrease results from a quantitative analysis which will be discussed in more detail in chapter 7. The attenuation of the Cu signal will be used in that chapter to determine the inelastic mean free path of the electrons.
We do not see any structure in our photoemission spectra that can be attributed to an interaction of Co and Cu states. This is an indication for the weak interaction between the Cu substrate and the Co adsorbate. Reasons for this behaviour are:

1. The overlap of Co and Cu valence bands is weak. The binding energy of Cu d-states is mainly above 2eV whereas Co has the highest density of states below 2eV binding energy. This can be seen in the local density of states in fig. 6.2 and also by comparison of the band structures of Co (fig. 5.4) and Cu (fig. 5.3). In the photoemission spectra, the peaks of Cu and Co are well separated. Except for one Co majority band, that has a weak structure in some spectra (20eV and 25eV photon energy) at a binding energy of about 2eV, there is no overlap with Cu peaks. Emission near E_F belongs to Co and peaks with a binding energy of more than 2eV belong to Cu.

2. The valence 3d-shell of Cu is filled with 10 electrons. For that reason the valence 3d electrons, that form to a high extent the valence band structure, are not very reactive. Changes in the electronic structure are mainly due to spd hybridization between substrate and adsorbate.

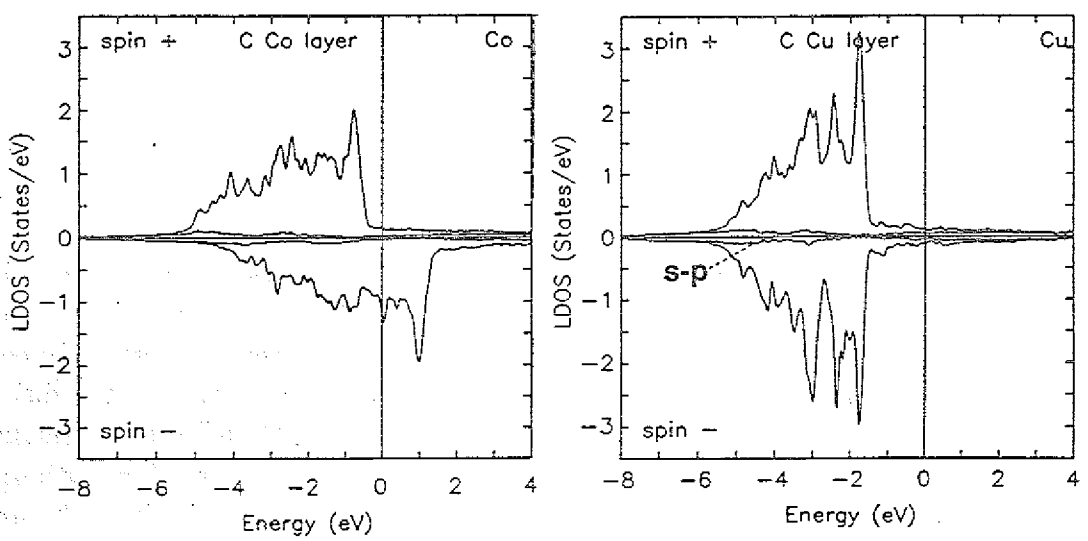

Fig 6.2a and 6.2b: Local density of state of bulk fcc Co and bulk Cu after [Clemens, 91].

At 10eV (6.1a) we show the entire spectra. The secondary edge at about 5eV binding energy corresponds to electrons that had just enough energy to overcome the work function of the solid. They arrive in the detector with nearly 0eV kinetic energy. We calculate the work function Φ as the difference between photon energy and binding energy at the

secondary edge. For Cu(111) we get a work function of $\Phi_{Cu(111)} = (4.7 \pm 0.2eV)$ and with Co on top Cu(111) it changes by 0.2eV to $\Phi_{Co(111)} = (4.9 \pm 0.2eV)$ (see fig. 6.3). For comparison we give our value of $\Phi_{Co(100)} = (4.7 \pm 0.2eV)$ obtained for Co(100). For polycrystalline Co a work function of 5.0eV is reported in [Michaelson, 77].

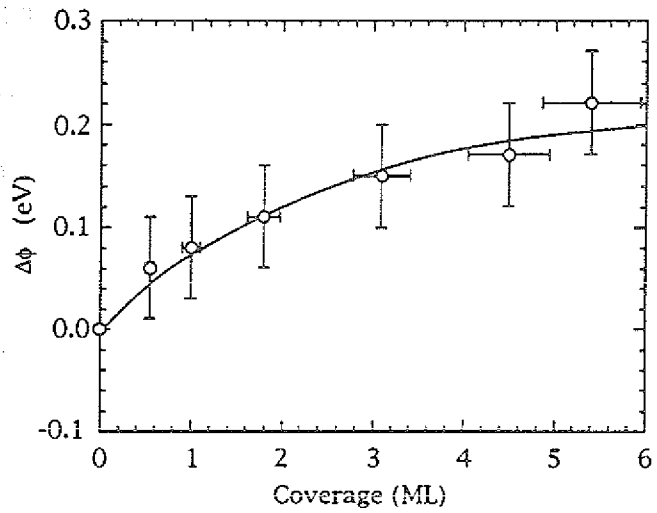

Fig. 6.3: Change of the work-function $\Delta\Phi$ of Cu(111) with increasing Co coverage.

The high intensity in the background for low kinetic energies has its origin in inelastic scattering of the excited electrons.
The intensity does not go to zero in the spectra at 10eV, above the Fermi energy. The electrons, that seem to have negative binding energy, are due to second-order light that can pass through the beamline. The monochromator, that has been adjusted to transmit light of a fixed energy, fulfills the Bragg law for light of twice the photon energy in the second harmonic. The relative intensity of the second harmonic light to first harmonic light is strongest at these low photon energies.

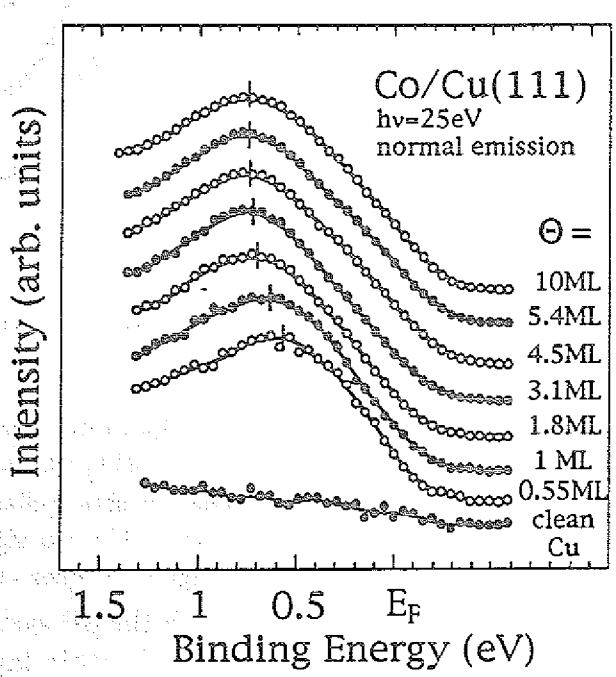

Fig. 6.4: Spin-integrated photoemission curves taken with 25eV photon energy in normal emission. The spectra are normalized to equal height.

While the Cu emission is attenuated by the overlayer, the intensity of the signal arising from the Co increases. Besides these changes in intensity, the Co peaks shift at low coverages. In fig. 6.4 the spectra of fig. 6.2e have been normalized to equal height and the binding-energy scale has been enlarged to emphasize the binding energy-shift of the Co peaks. It shows the spectra taken at 25eV photon energy where the strongest changes have been observed. The maximum of the curves at 25eV shifts between 0.55ML and 3.1ML Co coverage by about 0.2eV.
We attribute these shifts to a transition from a 2D ($E = E(k_{||})$) to a 3D system ($E = E(k_{||}, k_{\perp})$).
Due to the fact that the spectra in fig. 6.1a-f were taken in normal emission the parallel component of the momentum is always zero ($k_{||} = 0$). By varying the photon energy one changes $k_{\perp}$. A 2D system is independent on $k_{\perp}$ and therefore expected to show no dispersion.

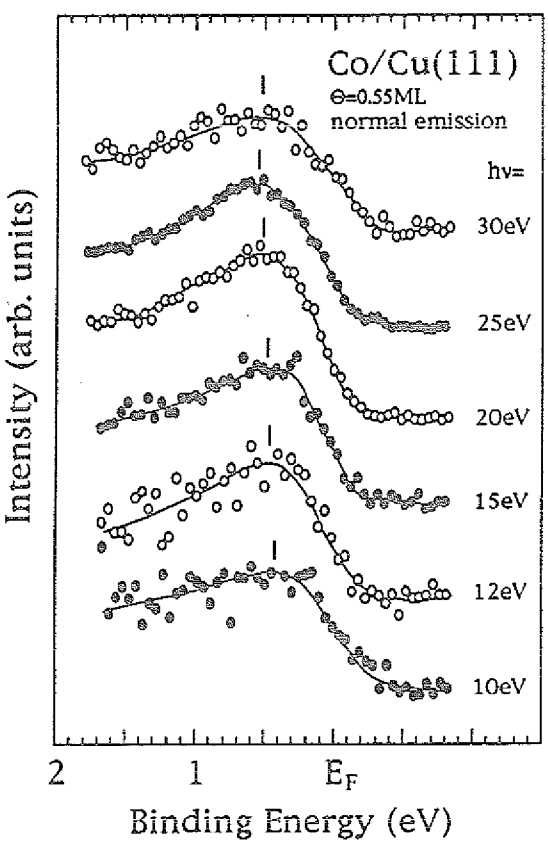

Fig. 6.5a: Spin-integrated curves of 0.55ML Co on Cu(111) for various photon energies in normal emission. The Cu signal distribution has been subtracted.

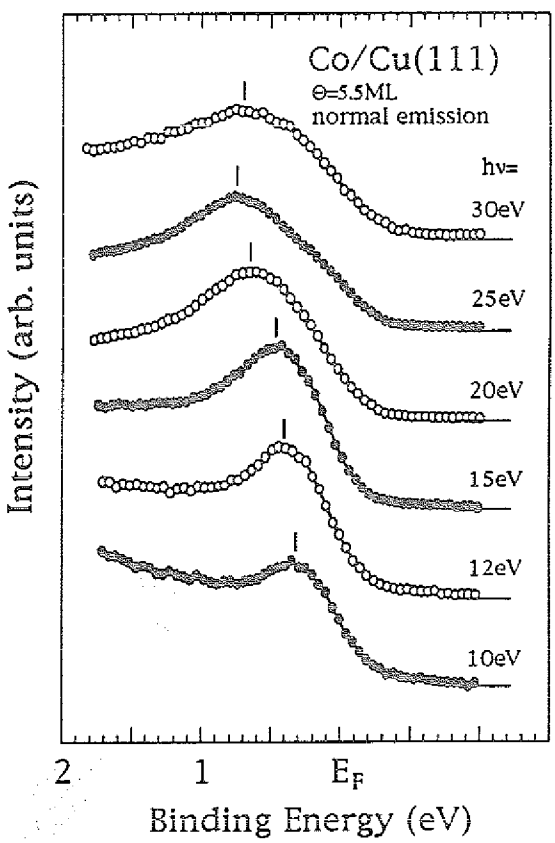

Fig. 6.5b: Spin-integrated curves of 5.5ML Co on Cu(111) for various photon energies. The Cu signal distribution has been subtracted. The Co signal near E_F does not change for higher coverage.

To study the dispersion of the 2D Co system in comparison with the 3D system, we show in fig. 6.5a and 6.5b the dispersion of the Co structure for an ultrathin layer (0.55ML)

and for a rather thick layer (5.5ML). The Co emission has been separated in the spectra by subtracting the clean Cu spectrum of the same photon energy with an intensity proportional to the Cu emission. This makes it easier to determine the maximum of the Co peak, especially at 10eV and 12eV photon energy of the 0.55ML film.
The results are shown in fig. 6.6. The dispersion of Co in the system 5.5ML Co/Cu(111) shows the $k_\perp$-dependence of bulk Co. The binding energy of the Co peak shifts from 0.35eV near L to 0.7eV at Γ. The dispersion is similar to the dispersion of the upper Cu Λ_3 band, serving separately as a reference.
The Co peak in the difference curves of 0.55ML Co/Cu(111) (fig 6.5a) shows only a slight shift of about 0.1eV between L and Γ. The dependence on $k_\perp$ is negligible within the accuracy of the experiment.
This indicates that between 0.55ML and 5.5ML Co/Cu(111) there is a transition from a two-dimensional to a three-dimensional system.

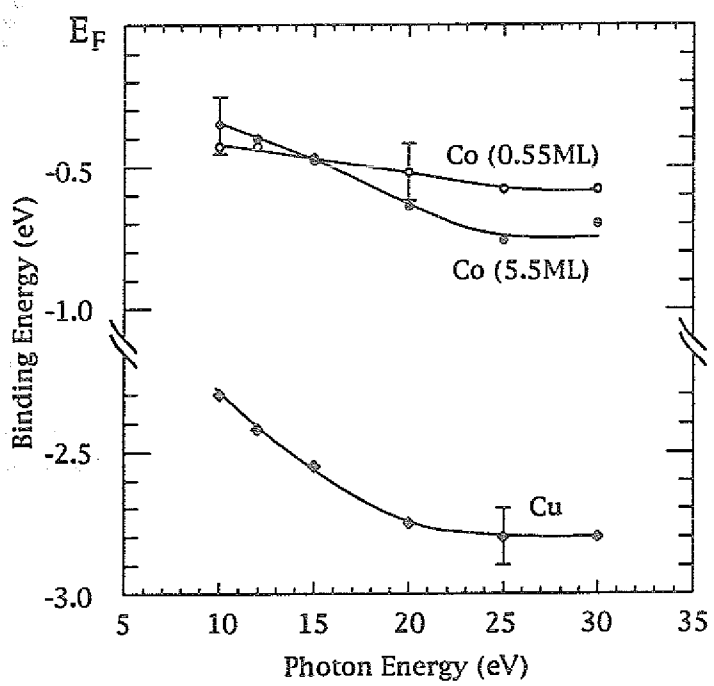

Fig 6.6: Co peak binding energy versus photon energy, as obtained from fig. 6.5. The photoemission spectra of 5.5ML Co coverage show the dispersion of the bulk, wheras nearly no dispersion can be found in the submonolayer regime.

Now we show with the help of spin-resolved spectra that already 2.5ML Co/Cu resemble the spin-split bandstructure of bulk Co. We therefore show spin-resolved spectra of different coverages in fig. 6.7a,b. The spectra were taken with s-polarized light of 15eV and 25eV photon energy in normal emission. We found that Co films of less than 2ML thickness cannot be magnetized permanently in plane; spin-resolved spectra below 2ML Co thickness are for that reason not informative. We have started the series with a coverage of 2.5ML Co ($h\nu = 15eV$) and 2.8ML Co ($h\nu = 25eV$). The last spectra were taken at a coverage of about 25ML, where no sign of Cu can be seen any more.

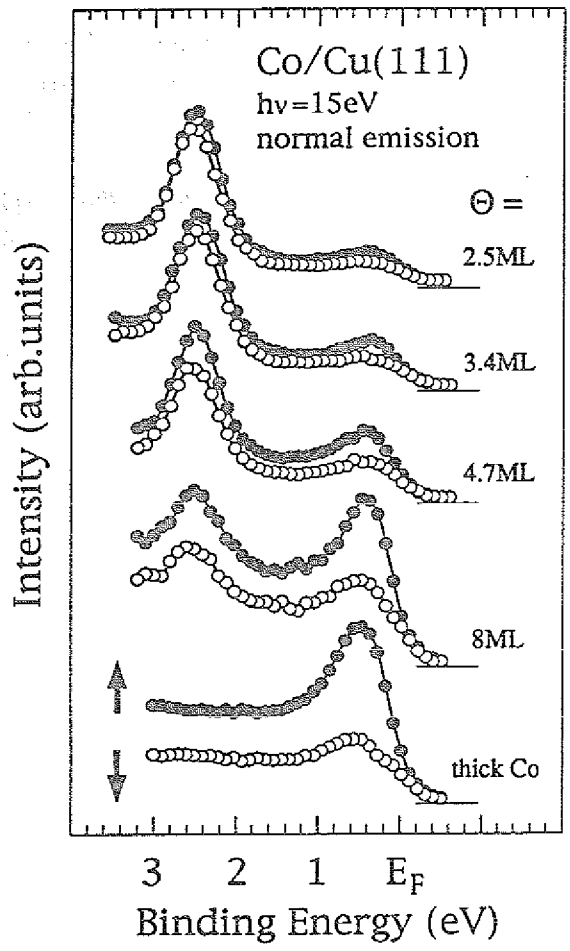

Fig. 6.7a: Spin-resolved photoemission curves of Co/Cu(111) taken at 15eV photon energy in normal emission. Filled (empty) circles correspond to majority- (minority-) spin direction.

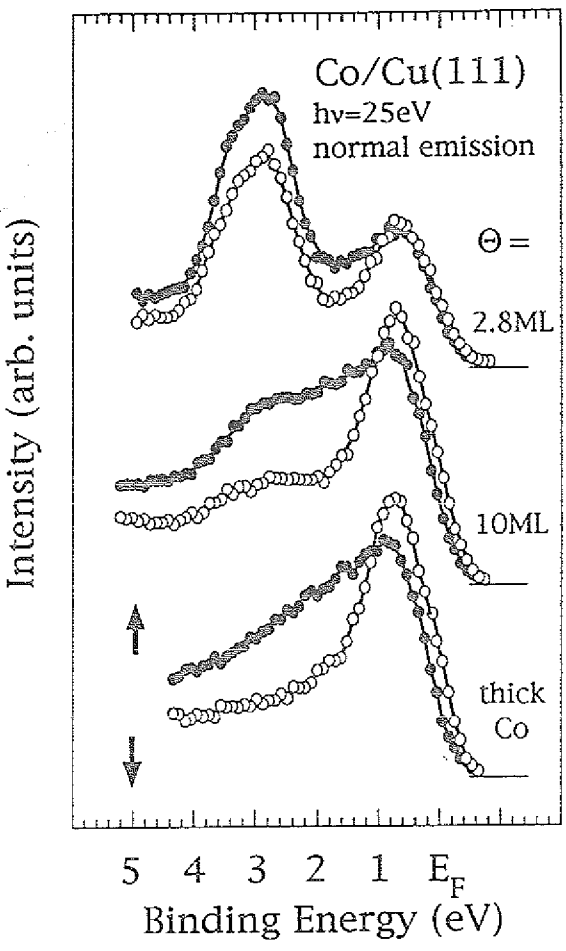

Fig. 6.7b: Spin-resolved photoemission curves of Co/Cu(111) taken at 25eV photon energy in normal emission. Filled (empty) circles correspond to majority- (minority-) spin direction.

In fig. 6.7 we show that the Cu peaks in the spin-resolved spectra resemble the behaviour that has been seen already in the spin-integrated spectra in chapter 5.1. With increasing Co thickness the substrate signal decreases in intensity, but the binding energy remains constant. Since Cu is not ferromagnetic and the interaction with Co is weak, we see the same behaviour for majority- and minority-spin electrons.
The structures arising from the Co overlayers on the other side are strongly polarized. In the bottom spectrum of a thick layer in fig. 6.7a there is strong emission from majority-spin electrons and a much smaller peak for minority-spin electrons. For lower coverages the spectra are qualitatively the same with respect to the Co emission. The peak positions of the Co structures for the very thin films agree with the peak positions of the thick film. A similar series that show the same behaviour for 20eV photon energies will be shown in chapter 7 (fig. 7.8a).

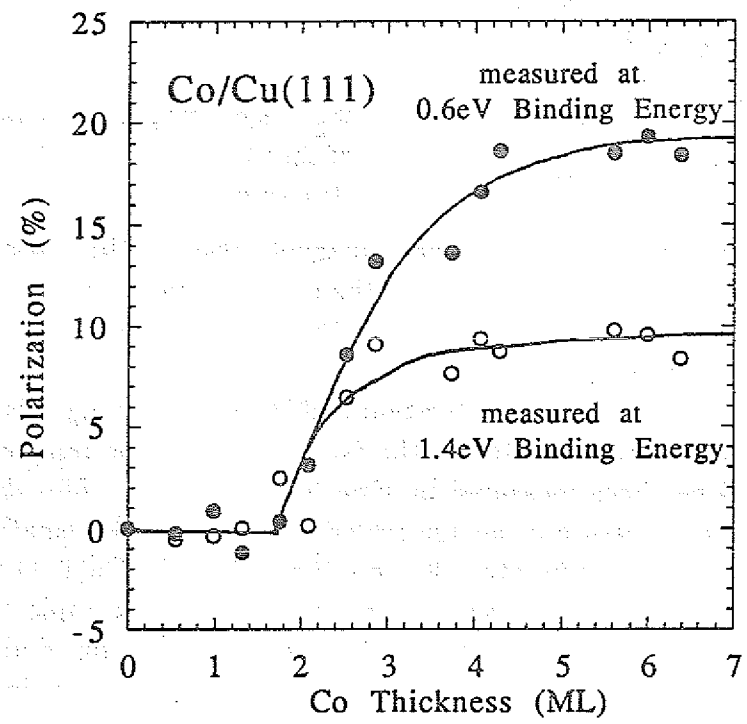

Fig. 6.8: Polarization P as a function of the Co film thickness, measured with 15eV photon energy in normal emission. Filled (empty) circles show the polarization at 0.6eV (1.4eV) binding energy.

The polarization $P(E)$, defined in eqn. 28, as a function of Co coverage at a fixed photon energy ($h\nu = 15eV$), is shown in fig. 6.8. The polarization has been measured at two different binding energies. At 0.6eV binding energy (filled circles) the Co majority peak comes out and the polarization is always higher than in the rest of the spectrum. The other point is 1.4eV (open circles) binding energy, where neither Cu nor Co shows strong emission.

The starting point for remanent in-plane magnetization is in fig. 6.8 at about 2ML Co/Cu(111). Up to 2ML we are not able to magnetize the sample remanently in plane. Between 2 and 3ML the polarization increases steeply and a 6ML Co sample already shows a strong polarization, which slowly increases for higher coverage.

Gradmann investigated the magnetic properties of ultrathin Co(111) films that were grown on Cu(111) [Gradmann, 70] [Gradmann, 71] [Gradmann, 73]. After the production of the Co film it has been covered with Cu to reduce contamination. Gradmann found that a monolayer of Co is spontaneously magnetized perpendicular to the surface, the magnetization $M_S(T)$ depending linearly on the temperature T [Gradmann, 70]. The Curie-temperature for the single layer is, according to this work, $0.3T_C(\infty) = 416K$ ($T_C(\infty)$=1388K [Kittel] is the Curie-temperature of the bulk).

He reports that the easy-magnetization axis rotates with increasing Co coverage and about two monolayers the magnetization was found to be in the surface plane.

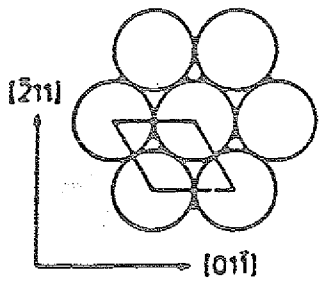

Fig. 6.9: Real-space image of the (111) surface of the fcc structure.

The polarization shown in fig. 6.8 depends on the in-plane magnetization of the sample. Taking into account the results of Gradmann we interpret the onset of magnetization in the surface at 2ML with a turn of the magnetization axis rather than with an onset of magnetic long-range order at this coverage.
Another possible explanation for the onset of magnetization at 2ML is the change of the Curie temperature with the Co film thickness. Due to the fact that the Curie temperature of the single Co layer (416K) has been measured by Gradmann with a Co film that was covered with Cu, the Curie temperature of an uncovered Co layer can be smaller. If the Curie temperature is below room temperature for less than 2ML Co/Cu(111) we can expect an onset of magnetization at this coverage. In our experiment the sample was oriented in a way that applied the magnetic field along the ($\underline{2}11$) direction (see fig. 6.9) of the fcc crystal. With this geometry we obtained a high polarization in the spectra, indicating that the magnetization stayed to a high degree within this axis after the external magnetic field was switched off.
We are not able to decide absolutely whether the sample was magnetized in the chosen ($\underline{2}11$) axis or the (01$\underline{1}$) axis. If the sample was misaligned completely (field applied along ($\underline{2}11$) axis, but magnetization is along the (01$\underline{1}$) axis) where the sample is 30^0 out of the magnetization direction one can expect only a decrease of 15% in the absolute polarization of the spectra. Due to the fact that we have applied the magnetic field always along the same direction we do not know whether the polarization increases or decreases when the sample is rotated.

Only a few studies of ultrathin layers of Co on Cu(111) have been published up to now. Miranda [Miranda, 82] studied 1 and 2ML Co/Cu(111) with angle-resolved photoemission. He presented spin-integrated spectra of 0.9 and 2.1ML Co/Cu(111) taken with s-polarized light of 25eV photon energy in normal emission. These spectra can be directly compared to the spectra in fig. 6.1e. The ratio of the Co and the Cu signal intensity in Miranda's spectra agree with our thickness calibration.
He found, in contrast to our results, that the peak positions in the spectra at 25eV do not change between 1 and 2 monolayers. He claimed moreover that they do not differ to those of the single Co(0001) crystal. We clearly see changes of the peak positions in fig. 6.4, although they are small for coverages of more than 1.8ML ($\approx 0.1eV$). Possible reasons for the fact that already 1ML Co shows a small dispersion (a difference between 0.55ML and 1ML is evident in fig. 6.4) dispersion are (a) the thickness of the films is

underestimated and the second layer has already started to grow in the spectra referred to as 1ML, or (b) the second layer starts to grow when the first layer is not finished completely (multi-layer growth). When we take into account the results of the Auger study of Tikhov [Tikhov, priv.], where the low-energy curve did not show the discontinuity in the slope as expected for Frank van der Merve growth, the multi-layer growth (b) seems more likely.
Miranda determined the peak positions in his spectra at 25eV as a result of a deconvolution of the spin-integrated spectra (see fig. 6.10). The peak positions and the intensities of this deconvolution do not fit with our spin-resolved spectra (see fig 6.7b, 2.8ML). The main difference is the peak position of the majority Co peak found in our spin-resolved spectra at about 2eV. He determines the binding energy of this peak as 1.4eV and obtained an exchange splitting of 0.7eV that is much less our value of $\Delta E_{ex} = 1.4eV$.

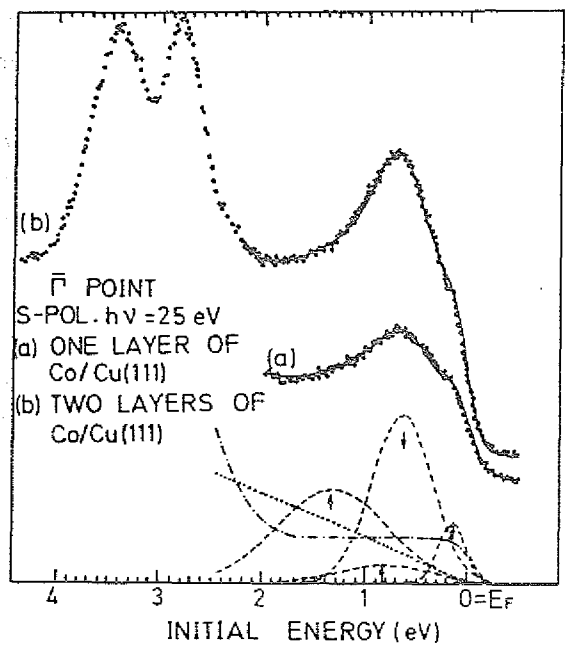

Fig. 6.10: after Miranda [Miranda, 82]: Angle-resolved energy distribution curves of photoelectrons taken at normal emission, using s-polarized light. The photon energy is 25eV. Experimental results for (a) one (0.9 ± 0.2) layer of cobalt on Cu(111) and (b) two (2.1 ± 0.2) layers of cobalt on Cu(111), are shown. The continuous lines show the fit of the experimental data with the following contributions: four Gaussians for the exchange-split bands (the lower pair being more intense), the s-p band of Cu and a secondary electron background. The arrows indicate spin-up (-down) subbands. The same set of Gaussians properly weighted fits the one (0.9) layer and two (2.1) layer spectra.

Summarizing the results obtained in this chapter we can say that a film of 0.55ML Co on top of the Cu(111) has been found to represent a two-dimensional system.
With increasing coverage a three-dimensional bandstructure develops and at a coverage of 5.5ML Co on Cu(111) we see the bandstructure of bulk Co.
At 2ML we observe an onset of magnetic behaviour that has been interpret with a rotation of the magnetization axis into the surface plane.

7 The Inelastic Mean Free Path (IMFP) of Electrons

7.1 Determination of the Electron Mean Free Path in Co

For most electron spectroscopies the characteristic surface information is contained in the energy E, the momentum k and the spin s of the electrons escaping the material. Therefore the information is lost after elastic or inelastic scattering events that the electron may encounter on its way between the point where it was generated and the detector. Inelastic scattering processes arise from electron-electron or electron-phonon interactions. For a homogeneous material the inelastic scattering probability is proportional to the path length x in the material. The flux of electrons of a certain state $(E, \mathrm{k}, \mathrm{s})$ therefore decays exponentially according to

$$I = I_0 \cdot e^{-x/\lambda} \tag{41}$$

where λ is the mean free path of the electron. For electrons with energies ranging from 10-1000eV, experimental values of 2-20Å for the mean free path have been found for most materials. In fig. 1.1 we have shown a compilation of the available experimental data for the mean free path of various materials [Zangwill, 88]. This experimental data were obtained either by direct transmission experiments or by measuring the reduction in a characteristic electron emission from a different substrate after the deposition of an overlayer of the material. For the use of the overlayer technique it must be ensured, that the adsorbate grows strictly layer-by-layer to avoid errors due to holes in the overlayer or diffraction effects.
Due to the fact that most of the accumulated data show a similar dependence of λ as a function of energy, the data are often displayed as the "*universal curve*" for the mean free path. In fig. 1.1 the full line represents a universal curve.
Seah [Seah, 79] has described the variation of λ with energy in the analytical form

$$\lambda_m = \frac{538}{E^2} + 0.41\sqrt{a \cdot E} \tag{42}$$

where λ_m is the IMFP in monolayers and a is the monolayer thickness in nanometres. For low electron energies λ is proportional to E^{-2}. This can be explained by the fact, that the scattering probability of the excited electron is proportional to the product of accessible filled electron states ($\simeq E\,n(E_F)$) and accessible unoccupied states ($\simeq E\,n(E_F)$).
Electrons with high kinetic energies are much less influenced by electron- or phonon-scattering events which leads to a higher IMFP. As a consequence we find a universal curve with a minimum at about 50eV electron energy.

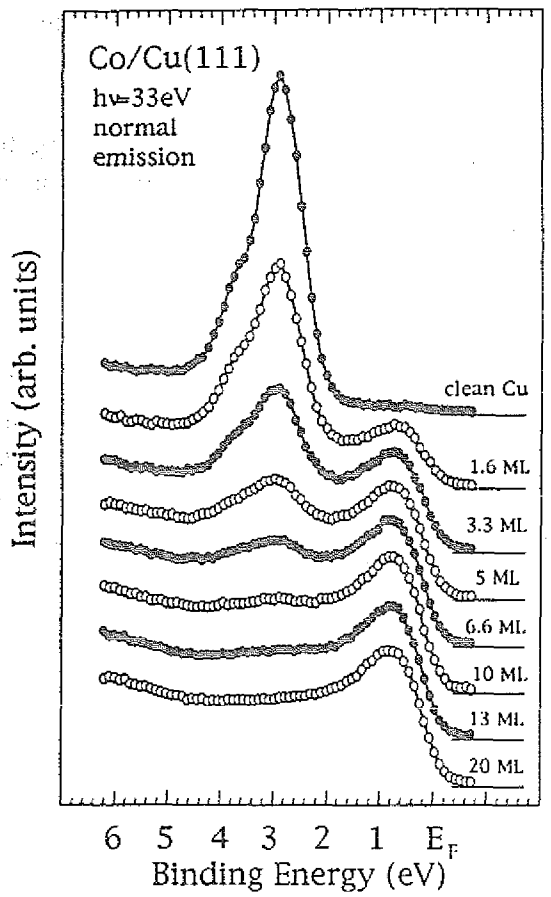

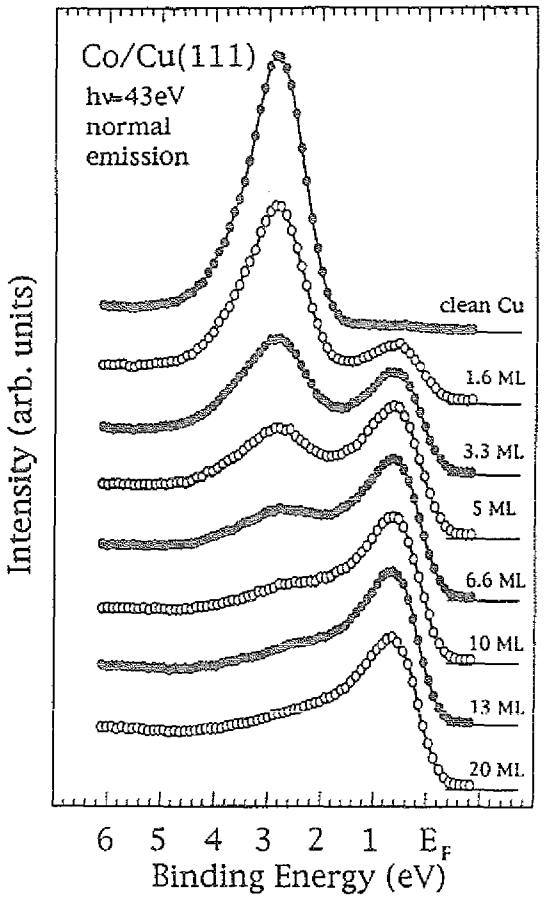

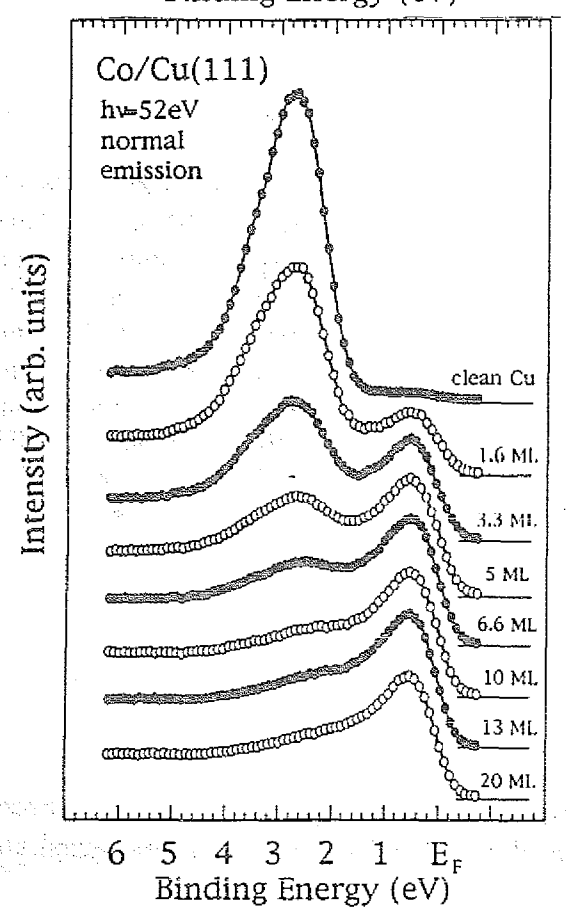

Fig. 7.1a-c: Spin-integrated photoemission curves of Co/Cu(111), taken in normal emission with s-polarized light of a) 33eV, b) 43eV and c) 52eV photon energy. The spectra are normalized to the photon flux.

However, there exists no reason for the assumption that a single curve should be able to describe the IMFP in all materials and consequently large deviations are expected.

In this chapter we study the inelastic mean free path of electrons originating from a Cu substrate travelling through a thin Co film. We determine the IMFP by measuring the attenuation of the Cu signal in photoemission experiments. Including the results obtained in chapter 4 for the high-energy electrons of the Auger decay process we determine the IMFP of electrons in Co for kinetic energies ranging from 7-920eV.

The spectra in fig. 7.1 show spin-integrated photoemission spectra as a function of coverage for three different photon energies. They were taken in normal emission with s-polarized light. The spectra are normalized to the photon flux on the sample. At this point we are interested mainly in the intensities of the Cu and the Co peaks. Due to the fact that the spectra are normalized, we can also compare the intensities of the Cu peak for different coverages. As already seen in the Auger study of chapter 4 this allows one to determine the IMFP with the Cu signal and the Co signal independently.
In some of the following spectra where the photon flux has not been measured, we can use the ratio between Cu and Co peak intensities only leading to larger uncertanties in the resultimg IMFP.

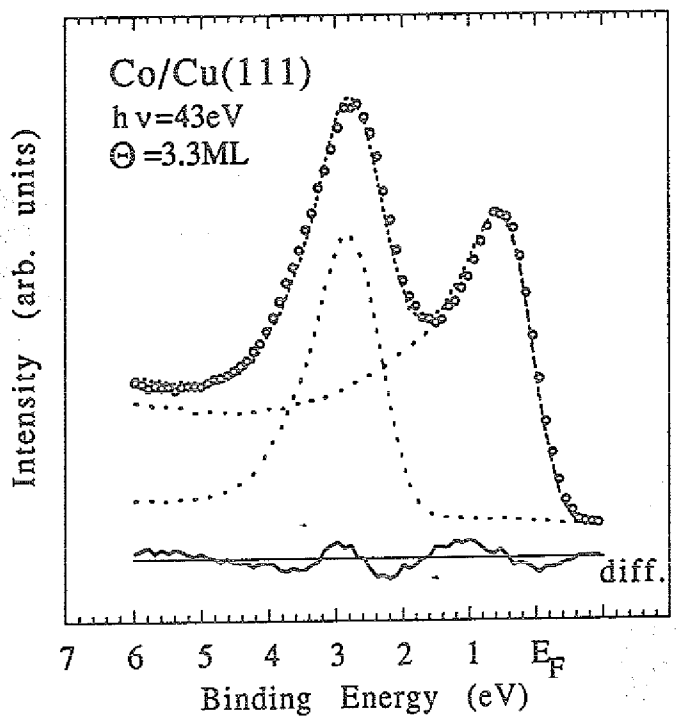

Fig. 7.2: Spin-integrated spectrum of 3.3ML Co/Cu(111) taken with 43eV photon energy. The dotted lines show a Cu(111) and a Co(111) spectrum taken at the same photon energy. The superposition of these two spectra is printed with a broken line. Also the difference between the simulation and the 3.3ML Co/Cu spectrum is shown.

To determine the relative signal intensities in fig 7.1, each spectrum has been simulated by the superposition of a measured clean Cu spectrum and a measured thick Co

spectrum. For the 3.3ML spectrum measured at 43eV photon energy we show such a simulated spectrum in fig. 7.2. The superposition is drawn with a dotted line and the spectrum of 3.3ML Co/Cu(111) is plotted with circles. In the difference curve appear small structures that indicate a broadening of the Cu peak in the 3.3ML spectrum. Due to the weak interaction between adsorbate and substrate, the simulated spectra match very well with the measured spectra for intermediate thicknesses.
We also tried other methods to determine the signal intensities, such as integration over the peak area or measuring the peak height but these methods include uncertanties in the background that can be avoided with the our method of simulating the spectra.

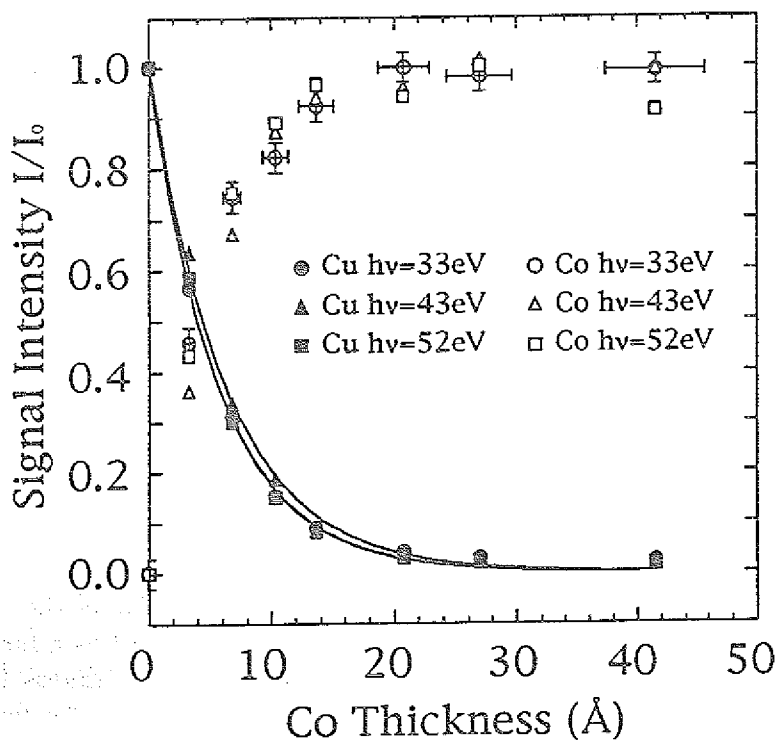

Fig. 7.3: Intensity of the Cobalt (open circles) and Copper (filled circles) signal in fig. 7.1 as a function of the Co thickness. The lines show exponential curves fitted to the points.

With the intensity of the clean Cu and thick Co set to 100%, we get changes of the signal intensities with overlayer thickness as shown in fig. 7.3. Errors of ± 0.03 in the intensity I/I_0 are due to uncertainties in the superposition. The errors in the thickness are 10% of the total coverage. Due to the fact that usually the IMFP is given in Å we give the coverage in fig. 7.3 in Å instead of ML (for Co(111): 1ML=2.08Å). For the growth mode we considered ideal layer-by-layer growth with a linear increase of the Co coverage with deposition time.
The lines in fig. 7.3 represent a least-squares fit of an exponential curve to the intensity of the Cu substrate signal. Obviously the attenuation of the Cu signal is very similar for 30eV, 40eV and 49eV kinetic energy (the kinetic energy is referred to E_F and can be calculated as photon energy minus binding energy). Consequently the IMFP does not change strongly with the kinetic energy in this energy range. We obtain IMFP's of

$\lambda(30eV) = (5.3 \pm 0.6)$Å, $\lambda(40eV) = (5.8 \pm 0.6)$Å and $\lambda(49eV) = (5.3 \pm 0.6)$Å from the Cu substrate signal. The intensity of the Co signal in fig 7.2 has been fitted with the expression

$$I = I_0(1 - e^{-x/\lambda}) \tag{43}$$

where I_0 and λ are the fitting parameters. The IMFP's resulting from the fits to the overlayer signal intensity are $\lambda(32.5eV) = (5.0 \pm 0.6)$Å, $\lambda(42.5eV) = (5.5 \pm 0.6)$Å and $\lambda(51.5eV) = (4.7 \pm 0.6)$Å. The kinetic energy of the electrons originating from the Co is 2.5eV higher than for electrons that originate from Cu because the binding energy is about 2.5eV less.
The IMFP's that have been determined for the Co adsorbate electrons agree with those determined for the Cu substrate. This is expected since they both describe the same physical property, the inelastic mean free path of electrons in Co.

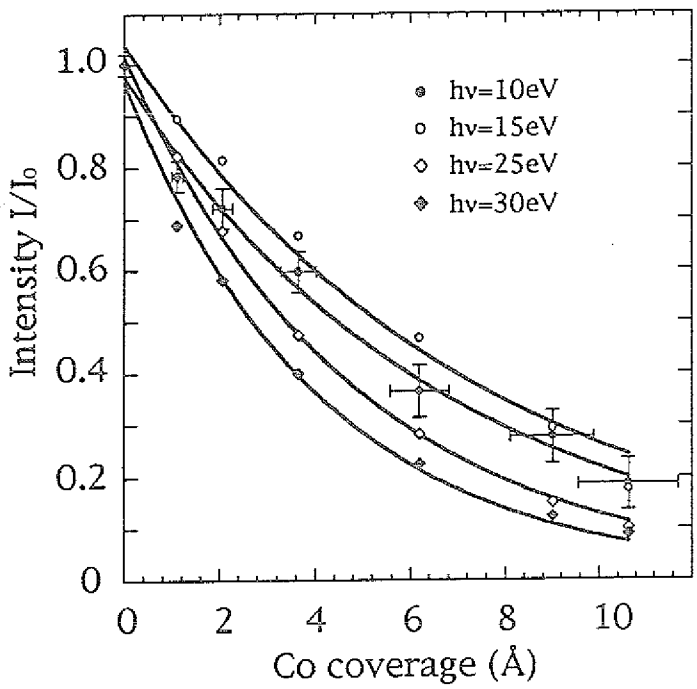

Fig. 7.4: Intensity of the Cu signal in fig. 6.1a-f as a function of the Co thickness for different energies. The lines show exponential curves fitted to the points.

We have extended our study of the IMFP to photon energies down to 10eV. In fig. 7.5 we show spectra similar to 7.1, but for lower photon energy. At $h\nu = 10eV$ the binding energy of the Cu peak is about 2.5eV. This corresponds to a kinetic energy of the electrons of 7.5eV in the solid (referred to E_F). In this energy range the universal curve already shows a strong increase.
The spectra in fig. 7.5 are not normalized. This means we can compare only the ratio of the Co and the Cu signal and not the absolute intensity. But when there is only one variable, we are not able to determine λ from the Co and the Cu signal separately. For this reason we assumed the same IMFP λ for the substrate and the overlayer signal. The

least-squares fit for the ratio I_{Cu}/I_{Co} has been done with the function

$$\frac{I_{Cu}}{I_{Co}} = A \cdot \frac{e^{-x/\lambda}}{(1 - e^{-x/\lambda})} \tag{44}$$

The results of this fit are included in fig. 7.6 (open circles). They clearly show an increase of λ between $h\nu = 30eV$ (27eV kinetic energy) and $h\nu = 10eV$ (7.5eV kinetic energy). In the photoemission spectra we can confirm this statement qualitatively by comparing spectra of the same Co coverage. At 10eV and 15eV photon energy, we can still see emission of the Cu substrate after deposition of 21ML Co. In the spectra taken at $h\nu = 20eV$ and above the Cu peak has vanished at this coverage. The same can be found by comparing spectra with 10ML Co coverage. The 20eV spectrum for this coverage shows a small Cu peak that hardly visible in the spectra taken with 30eV or 35eV photon energy. It is important to note that these effects cannot be attributed only to the change of the cross sections with photon energy for the excitation of Co and Cu states. Comparing previous spectra that were normalized to the photon flux (fig. 7.1a-c and fig. 6.1a-f) one can see that the ratio of the peak intensity for clean Cu and thick Co differ always by a factor of about 2-4. The relative cross sections for Co and Cu do therefore not change dramatically with photon energy. However, the above discussion uses only qualitative arguments, the quantitative results were obtained from the fit procedure.
The filled circles in fig. 7.6 originate from the spectra shown in chapter 6, fig. 6.1. Those spectra are again normalized to the photon flux and λ has been determined with the absolute intensity of the Cu peak, as in fig. 7.1. The intensities of the Cu peak versus coverage for 10, 15, 25 and 30eV photon energy together with the fitted exponential functions is shown in fig. 7.6. The spectra with the strongest decrease of the Cu-peak and consequently the shortest IMFP are the spectra taken with 30eV photon energy. Towards smaller kinetic energies we see a continuous increase of λ. The spectra taken at 10eV ($\lambda(7.5eV) = (7.3 \pm 1.2)$Å) are the only exception to this rule. Due to the large errors in λ it is not possible to say if the curve of the IMFP decreases for very low electron energies or if it is due to uncertanties in the determination of the peak height.

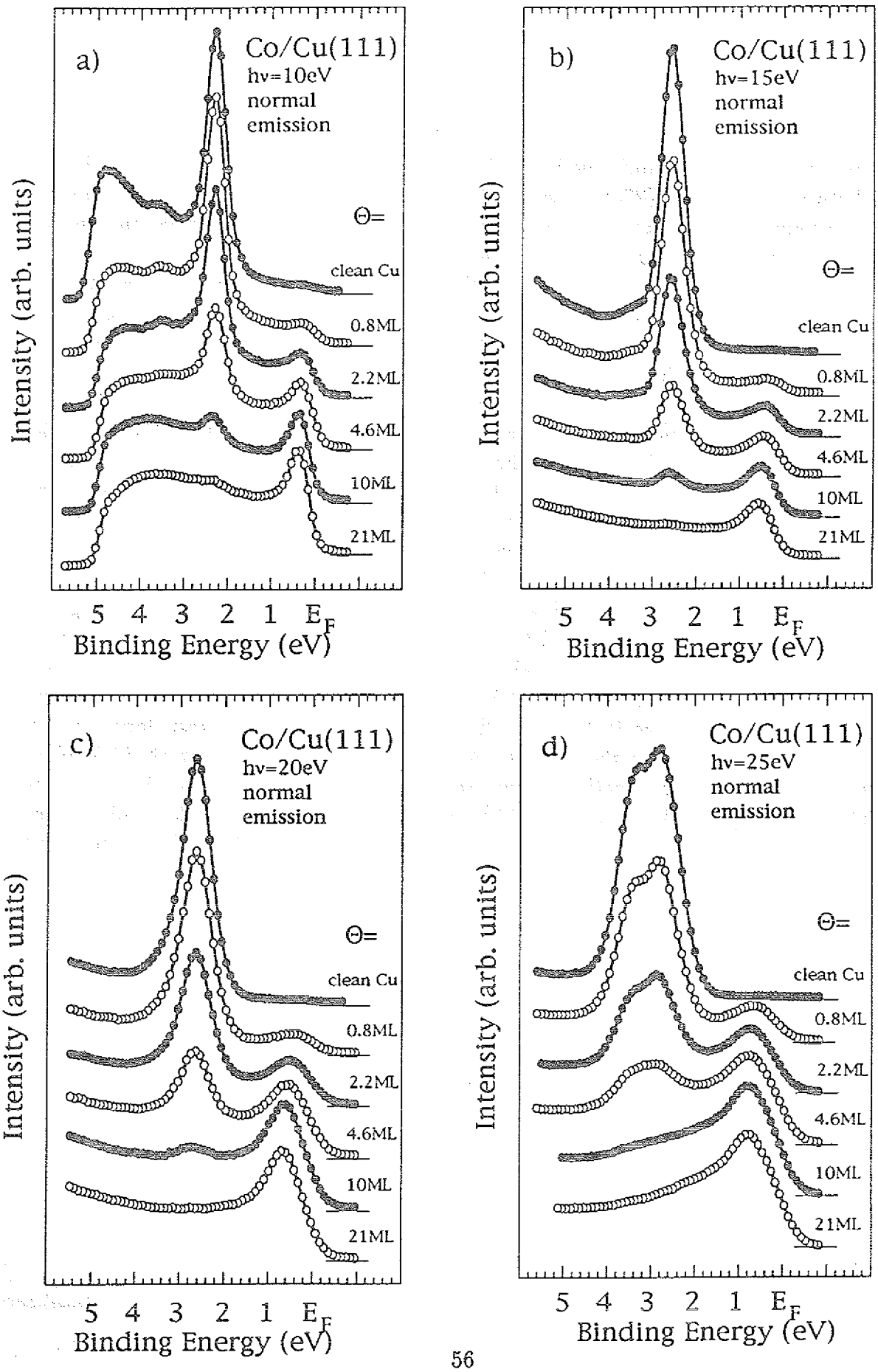
a)
Co/Cu(111)
hν=10eV
normal
emission
Θ=
clean Cu
0.8ML
2.2ML
4.6ML
10ML
21ML
Intensity (arb. units)
5 4 3 2 1 E_F
Binding Energy (eV)
b)
Co/Cu(111)
hν=15eV
normal
emission
Θ=
clean Cu
0.8ML
2.2ML
4.6ML
10ML
21ML
Intensity (arb. units)
5 4 3 2 1 E_F
Binding Energy (eV)
c)
Co/Cu(111)
hν=20eV
normal
emission
Θ=
clean Cu
0.8ML
2.2ML
4.6ML
10ML
21ML
Intensity (arb. units)
5 4 3 2 1 E_F
Binding Energy (eV)
d)
Co/Cu(111)
hν=25eV
normal
emission
Θ=
clean Cu
0.8ML
2.2ML
4.6ML
10ML
21ML
Intensity (arb. units)
5 4 3 2 1 E_F
Binding Energy (eV)

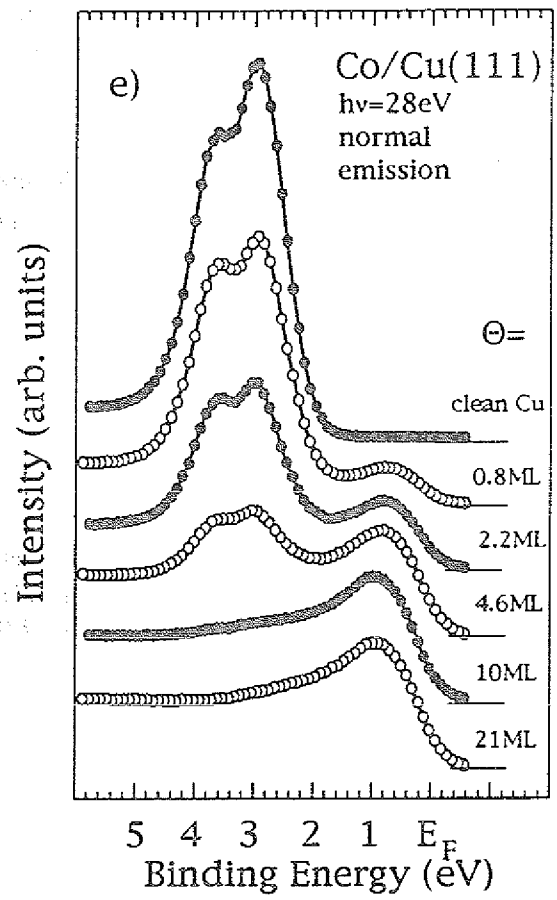

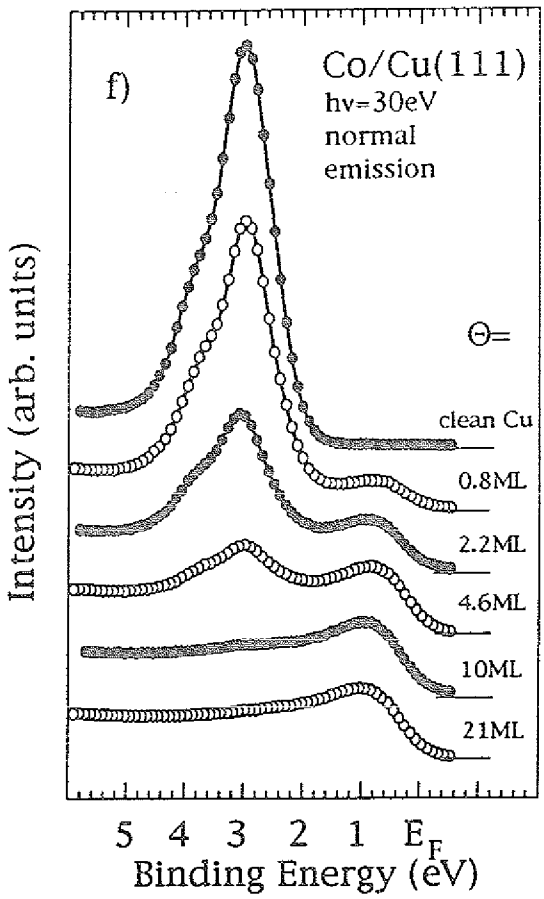

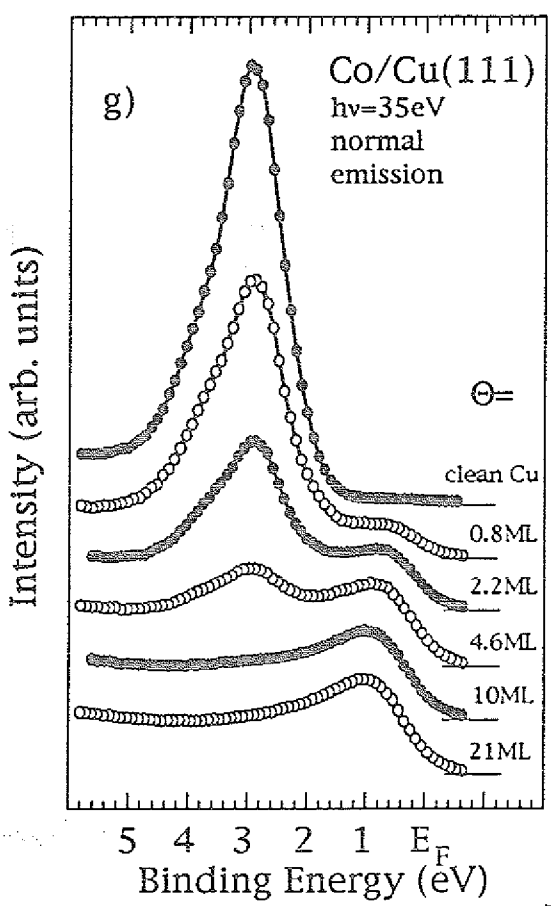

Fig. 7.5a-g: Spin-integrated photoemission curves of Co/Cu(111), taken in normal emission with s-polarized light of a) 10eV, b) 15eV and c) 20eV, d) 25eV, e) 28eV, f) 30eV and g) 35eV photon energy.

In fig. 7.6 the diamonds show the results of other measurements. They include the data obtained with the attenuation of high-energy Auger electrons discussed in chapter 4.

As a result of this study we have determined the IMFP in a Co film over a wide energy range. Qualitatively the data points and the theoretical curve of Seah and Dench (eqn. 42) agree. We see the minimum of the curve in the range 30-60eV and an increasing IMFP towards very low and high energies.

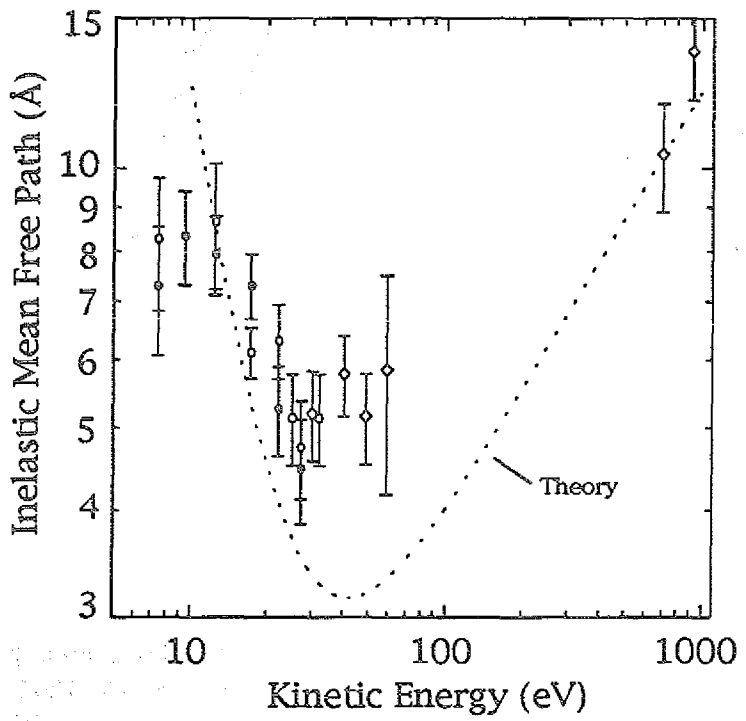

Fig. 7.6: IMFP of electrons scattered through a thin Co film as determined in PES and AES in comparison with the theoretical curve of Seah and Dench [Seah, 79].

The main differences are (a) that the theory predicts an IMFP of about 3Å in the minimum, whereas we find $\lambda_{min} = 5$Å in the experiment and (b) that for very low kinetic energies (below 10eV) the IMFP does not increase as strong as expected.

7.2 Spin Dependence of the IMFP

A long-standing question in spin-resolved spectroscopy and diffraction is whether and to what extent the IMFP is a spin-dependent quantity. If in photoemission the scattering probability differs for majority- and minority-spin electrons on their way to the surface we would observe a net polarization of the emitted electrons in photoemission that does not correspond to their polarization after excitation. To interpret measurements of ferromagnetic materials obtained with electron emission it is therefore important to know the value of the IMFP separately for majority- and minority-spin electrons.
Experimentally only a few data are available about the spin dependence of the IMFP. These are measurements of the spin polarization in secondary electron emission as for example [Bringer, 79] [Penn, 85] [Kisker, 82] and recent results from spin-resolved photoemission adressing this subject [Pappas, 91]. The relation between these experiments and the spin dependence of the IMFP will be discussed below.

Different theoretical models have been proposed to calculate the spin-dependent IMFP as a function of electron kinetic energy. They usually result in a shorter IMFP for electrons of minority-spin direction. The first attempt to calculate spin-dependent IMFP's on the basis of an atomic model has been suggested by Bringer *et al* [Bringer, 79]. Bringer *et al* predict a shorter IMFP for the minority- than for majority-spin electrons. They consider the scattering of an excited electron (below 50eV) by a valence electron in the center-of-mass frame of the two electrons. The antisymmetry of the total wave function implies that scattering cross sections are larger for electrons of opposite spin direction. Bringer *et al* make the assumption that the inelastic scattering probability of the excited electrons of one spin direction is proportional to the number of conduction-band electrons of the opposite spin direction. That leads to the following equation for the IMFP's for majority-spin ($\lambda^{\uparrow}$) and minority-spin ($\lambda^{\downarrow}$) electrons.

$$\frac{\lambda^{\uparrow}}{\lambda^{\downarrow}} = \frac{n^{\uparrow}}{n^{\downarrow}} \tag{45}$$

where $n^{\uparrow}$ and $n^{\downarrow}$ are the number of majority and minority spins per atom respectively. It is often convenient to express the difference between the IMFP of the two spin direction with a quantity called the *mean free path asymmetry*. The mean free path asymmetry is defined as

$$A_{\lambda} = \frac{\lambda^{\uparrow} - \lambda^{\downarrow}}{\lambda^{\uparrow} + \lambda^{\downarrow}} \tag{46}$$

This quantity is rather insensitive to the absolute magnitude of the IMFP. Errors in the determination of the average IMFP (as those obtained with spin-integrated spectra in the last chapter) do not influence the mean free path asymmetry as much as the IMFP of majority- and minority-spin electrons itself.
In the model of Bringer *et al* A_{λ} turns out to be positive and it does not change very much with the energy of the scattered electrons.

A more detailed calculation which takes into account the spin dependent band struc-

ture effects of the solid has been performed by Penn [Penn, 85]. According to Penn the shorter IMFP of the minority-spin electrons can be explained with the fact that in a ferromagnetic material there are more unfilled d states available for minority-spin electrons than for majority-spin electrons. Consequently, the scattering probability of minority-spin electrons into the empty minority states is larger than the corresponding scattering probability of majority-spin electrons into empty majority states. As a result of a spin-dependent calculation he found that the mean-free-path difference between the two spin-directions is significant only at very low energies (below 4eV above the vacuum level) where a relative small number of empty free-electron states is available and the scattering into the empty d states is emphasized. The mean free path asymmetry A_λ decreases rapidly with increasing electron energy.

Other calculations of Rendell and Penn [Rendell, 80] treat the conduction-band electrons as an electron gas in a local-density approximation including exchange effects. They predict at very low energy a mean free path asymmetry that is by a factor of 3 smaller than calculated in ref. [Penn, 85] ($A_\lambda \approx 0.02$ for Co at the vacuum level). It decreases further at higher energies but less rapidly than in the calculation of Penn [Penn, 85]. The calculated mean free path difference for Fe, Co and Ni, as calculated for this model by Rendell and Penn [Rendell, 80], is shown in fig. 7.15 at the end of this chapter.

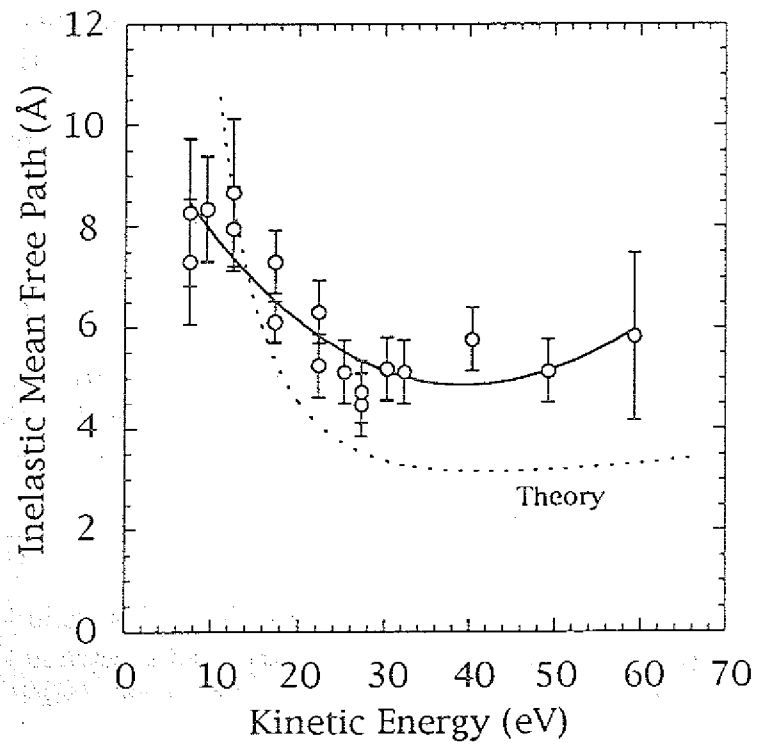

Fig. 7.7: IMFP of electrons scattered through a thin Co film. The theoretical curve of Seah and Dench [Seah, 79] is plotted with a broken line. The full line corresponds to least-squares fit of a 3rd order polynom.

A calculation of the spin-dependent IMFP and elastic scattering cross sections for energies above 100eV can be found in ref. [Matthew, 82]. Matthew's calculations are based on an atomistic model, as the model of Bringer [Bringer, 79]. His calculations predict a very small mean free path asymmetry at 100eV ($A_\lambda = 2.6 \cdot 10^{-3}$ for Co at 100eV) ,comparable

in magnitude to the predictions of Rendell and Penn [Rendell, 80]. It decreases further towards higher energies ($A_\lambda = 6.5 \cdot 10^{-4}$ for Co at 200eV).

Indirect experimental evidence for the spin dependence of electron scattering has been found in the secondary electron emission of a ferromagnetic material [Bringer, 79] [Penn, 85] [Kisker, 82]. It has been found that electrons with energies comparable to the vacuum level that had just enough energy to overcome the work function have a strong spin polarization which is significantly larger than the bulk electron-spin polarization. The spin polarization of these low-energy electrons decreases rapidly with increasing electron energy and reaches the electron-spin polarization of the bulk already a few eV above E_{Vac}. The enhanced spin polarization of the low-energy electrons can be attributed to different IMFP's for majority- and minority-spin electrons. When the scattering probability at low energies is greater for minority-spin electrons the signal originating from these electrons is attenuated stronger than the signal of the majority-spin electrons leading to an increased polarization at low energies.
Due to the fact that the polarization of the secondary electron emission is a rather indirect way to determine spin-dependent asymmetries of the electron scattering, there is much interest in getting more direct results. A new experimental and more direct approach to this question has been presented in a recent paper of Pappas [Pappas, 91]. Pappas studied a 4ML film of Fe deposited on Cu(100) with spin-resolved photoemission. Due to the fact that Cu is not magnetic one expects an equal number of majority- and minority-spin photoelectrons from an uncovered Cu sample. When this nonmagnetic substrate is coverered with a magnetic overlayer the electrons undergo scattering events on their way to the surface. If the scattering cross sections are the same for majority and minority spin electrons we can expect an equal signal intensity of the substrate electrons at the surface for both spin directions. In contrast Pappas found a strong spin dependence for the electrons photoemitted from the 3d bands of the Cu after travelling through the 4ML Fe film. The signal intensity for electrons with minority-spin direction was always smaller than for electrons with the opposite spin direction suggesting a shorter IMFP for minority-spin electrons. This approach allows to determine the spin-dependent mean free path in a ferromagnetic material as a function of electron kinetic energy. An extrapolation of his results towards the vacuum level gave a mean-free-path asymmetry of $A_\lambda \approx 0.2$ for the secondary electrons of Fe. Unfortunately the measurements were restricted to one coverage (4ML) and only 3 different electron energies. Furthermore the statistic in the spectra is rather poor and the presented spectra seem not to be representative for the asymmetries given in the text.
We follow in our experiment the approach of Pappas [Pappas, 91] to determine in a direct way the spin-dependent IMFP of electrons in Co. We give quantitative values for the IMFP's of majority- and minority-spin electrons as a function of energy and a curve for the mean-free-path asymmetry. A wide range of electron energies is studied at many different film thicknesses.

We study the emission of the Cu peak for the system Co/Cu(111).

Starting from an unpolarized Cu peak with the same photocurrent for minority-spin and majority-spin electrons, we can expect a thickness dependence of the individual spin currents according to

$$I^{\uparrow\downarrow} = \frac{1}{2} I_0 e^{-d/\lambda^{\uparrow\downarrow}} \tag{47}$$

We obtain for the spin-integrated current (sum of $I^{\uparrow}$ and $I^{\downarrow}$) with eqn. 47

$$I(d) = \frac{1}{2} I_0 \cdot (e^{-d/\lambda^{\uparrow}} + e^{-d/\lambda^{\downarrow}}) \tag{48}$$

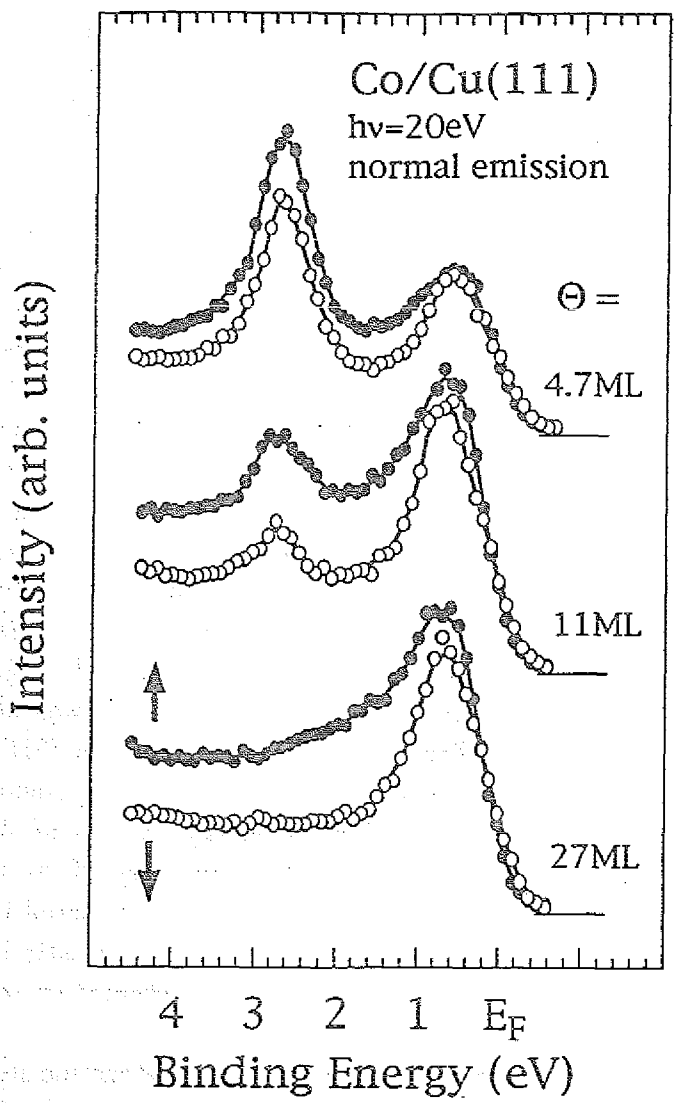

Fig. 7.8: Spin-resolved photoemission spectra of different coverages of Co on Cu(111), taken in normal emission with s-polarized light of 20eV photon energy

On first sight the intensity of the Cu signal in the spin-resolved spectra appears to be very similar for the two spin directions in nearly all spectra presented in this and in previous chapters. Differences come out only after a detailed analysis of the spectra. Since the attenuation of the Cu signal for the two spin directions is very similar we can expect that also the IMFP's do not differ very much. In this case the double-exponential decay is

experimentally indistinguishible from a single exponential,

$$I(d) = I_0 \cdot e^{-d/\lambda} \qquad \text{with} \qquad \lambda = \frac{1}{2}(\lambda^{\uparrow} + \lambda^{\downarrow}) \tag{49}$$

The spin-averaged IMFP λ can be obtained from spin-integrated spectra by measuring the attenuation of the substrate signal. This has been done for Co/Cu(111) in the last section. In fig. 7.7 we show again the results of this study. The solid line in this plot corresponds to a least-squares fit with a 3rd order polynomial and the dashed line shows the theoretical curve of Seah and Dench (eqn. 42) [Seah, 79]. We define the polarization of the Cu peak as

$$P_{Cu}(d) = \frac{I^{\uparrow} - I^{\downarrow}}{I^{\uparrow} + I^{\downarrow}} = \frac{1}{2} \cdot \frac{e^{-d/\lambda^{\uparrow}} - e^{-d/\lambda^{\downarrow}}}{e^{-d/\lambda}} \tag{50}$$

For the second part of the equation we used eqn. 47 and eqn. 49.

The intensity $I^{\uparrow\downarrow}$ is given experimentally by the peak area of the Cu signal. To determine the peak area of the Cu we have subtracted a spectrum of clean Cu in both spin directions of the spin-resolved spectra separately. The intensity of the subtracted spectrum is proportional to the peak area.
It turned out that it was often necessary to subtract a Cu spectrum with a higher intensity in the majority-spectrum than in the minority spectrum to obtain a smooth background in both cases. This effect is not visible on first sight, but in the subtraction there is clearly a difference between the two spin directions that is out of the error of the measurement. We obtain $\lambda^{\uparrow}$ and $\lambda^{\downarrow}$ by transforming eqn. 50 to

$$\frac{1}{\lambda^{\uparrow\downarrow}} = \frac{1}{\lambda} - \frac{\ln(1 \pm P(d))}{d} \tag{51}$$

Several spin-resolved spectra for different coverages over a wide range of photon energies were taken. Some of them, taken in normal emission geometry at 20eV photon energy, are shown in fig. 7.8 but compare also the spectra shown in fig 6.7a,b in chapter 6.
The emission of the Cu substrate can be seen at about 3eV binding energy. It originates from the upper Cu Λ_3 band as described in chapter 5. Near E_F we see the Co Λ_3 bands (lower minority Λ_3 band and upper majority Λ_3 band) and at 2eV in the bottom majority spectrum we find also emission from the lower majority Λ_3 band.

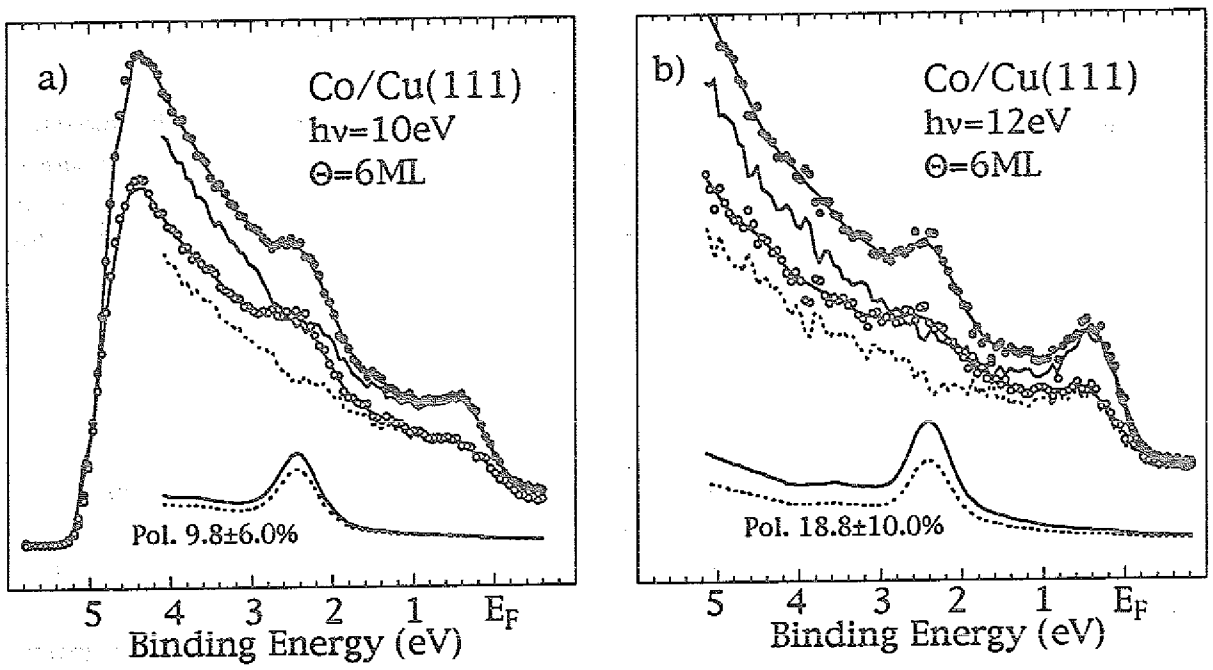

Fig. 7.9a,b: Spin-resolved spectra of Co/Cu(111) taken at 10eV (a) and 12eV (b) photon energy in normal emission. Majority-spin curves are printed with filled and minority-spin curves with open circles, rsp. In the bottom of the plots the contribution of the Cu substrate to the spectra is shown. The difference spectra after subtraction of the Cu signal are also shown. Full (dotted) lines correspond to majority (minority) spin direction.

We do not show all of the spin-resolved spectra used in our analysis, but some of them which are thought to be representative are shown in fig. 7.9a,b and 7.10a-d. The spectra in fig. 7.9 are taken with 10eV (a) and 12eV (b) photon energy at a medium film thickness (6ML) and the spectra in fig. 7.10a-d were all taken with 15eV photon energy but for different Co coverages. We plotted majority-spin curves with filled circles and minority-spin curves with open circles. To obtain the Cu signal contribution to the spin-resolved spectra we subtracted a spin-integrated spectrum that was taken at the same photon energy for clean Cu. The intensity of the subtracted Cu spectrum gives us the relative intensity of the Cu signal to the spin-resolved curves.

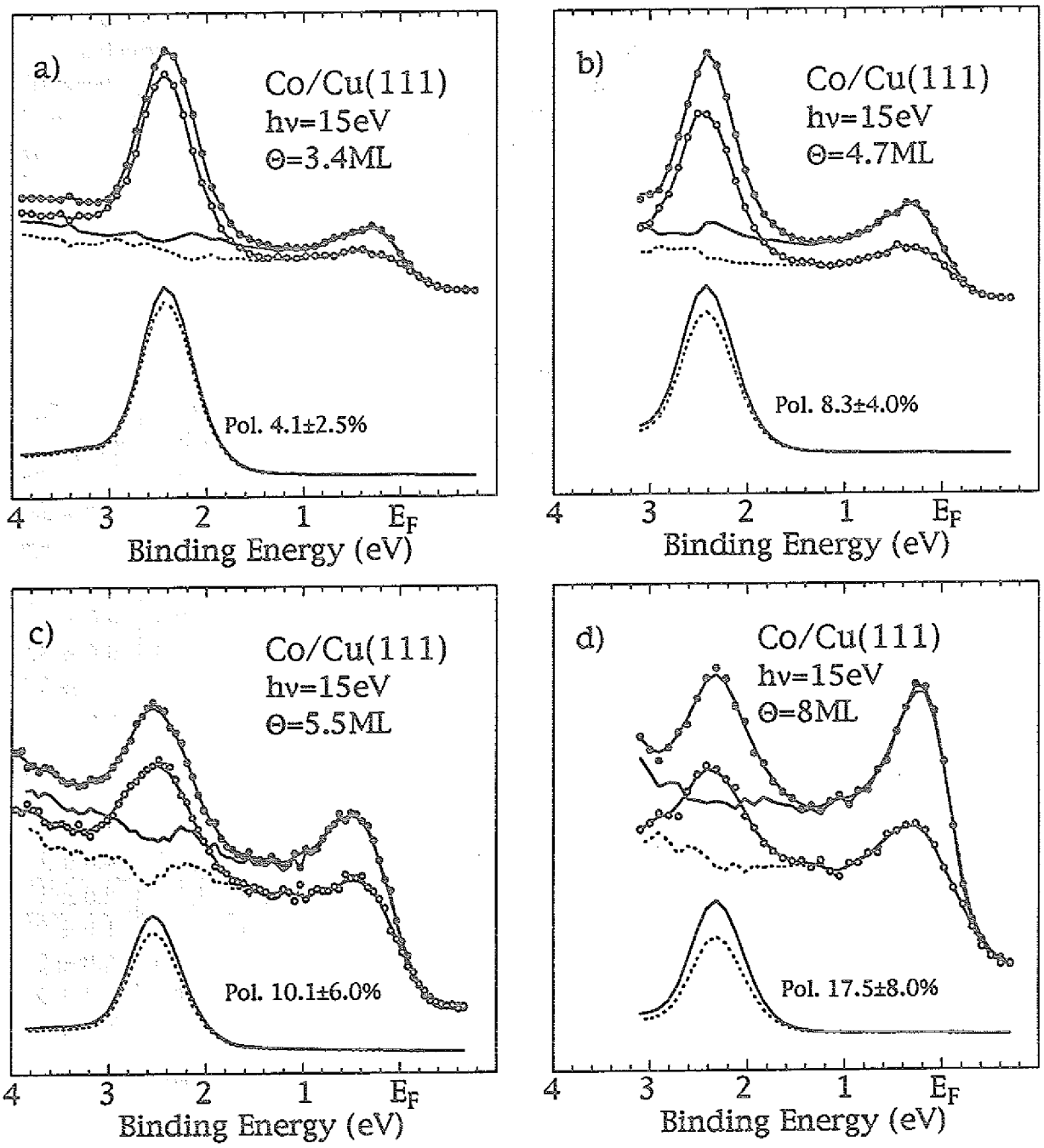

Fig. 7.10a-d: Spin-resolved spectra of Co/Cu(111) taken at 15eV photon energy in normal emission. Majority-spin curves are printed with filled and minority-spin curves with open circles, rsp. In the bottom of the plots the contribution of the Cu substrate to the spectra is shown. The difference spectra after subtraction of the Cu signal are also shown. Full (dotted) lines correspond to majority (minority) spin direction.

The subtracted Cu contribution is shown in the bottom of the figures 7.9 and 7.10. It is always smaller for the minority spectrum. The curve resulting after subtraction of the Cu contribution is shown also. It is not always possible to obtain a smooth background

after subtraction of the Cu spectrum (see for example the difference curve in fig. 7.10c) due to the different resolution of the spin-integrated and the spin-resolved spectra.
A compilation of the results of this analysis is given in table 2. It shows the polarization for different energies and coverages. The IMFP's $\lambda^{\uparrow}$ and $\lambda^{\downarrow}$ were calculated with eqn. 51 and the mean free path asymmetries were calculated with eqn. 46. The errors in $\lambda^{\uparrow\downarrow}$ and A_λ are due to errors in the determination of the polarization only. Uncertainties of the averaged IMFP λ (full line in fig. 7.7) have not been taken into account.

Photon Energy (eV)	Kinetic Energy (eV)	Thickness (Å)	Polarization (%)	$\lambda^{\uparrow}$(Å)	$\lambda^{\downarrow}$(Å)	A_λ(%)
10	7.8	12.5	9.8 ± 6.0	9.1 ± 0.4	8.0 ± 0.4	6.4 ± 0.4
12	9.6	12.5	18.8 ± 10.0	9.1 ± 0.6	7.1 ± 0.5	12.0 ± 6.0
15	12.4	5.2	4.8 ± 3.0	8.0 ± 0.4	7.0 ± 0.3	6.6 ± 4.4
15	12.4	7.1	4.1 ± 2.5	7.8 ± 0.2	7.1 ± 0.2	4.6 ± 2.6
15	12.4	7.3	8.7 ± 4.0	8.1 ± 0.3	6.8 ± 0.3	8.7 ± 3.7
15	12.4	9.8	8.3 ± 4.0	7.9 ± 0.2	7.0 ± 0.2	6.0 ± 2.5
15	12.4	11.4	10.1 ± 6.0	7.9 ± 0.3	7.0 ± 0.3	6.0 ± 3.8
15	12.4	16.6	17.5 ± 8.0	8.0 ± 0.3	6.9 ± 0.3	7.4 ± 3.8
20	17.2	9.8	6.2 ± 4.0	6.8 ± 0.2	6.3 ± 0.2	3.8 ± 2.9
20	17.2	22.9	17.8 ± 9.0	6.9 ± 0.2	6.2 ± 0.2	5.3 ± 2.9
25	22.2	6.2	6.6 ± 4.0	6.2 ± 0.2	5.5 ± 0.2	6.0 ± 3.2
25	22.2	20.6	9.3 ± 5.0	6.0 ± 0.1	5.7 ± 0.1	2.5 ± 1.7
30	27.2	10.0	8.9 ± 5.0	5.6 ± 0.1	5.1 ± 0.1	4.6 ± 1.8
34	27.2	10.0	3.5 ± 2.5	5.2 ± 0.1	5.0 ± 0.1	2.0 ± 1.9
43	40.2	9.2	2.5 ± 3.0	4.9 ± 0.1	4.8 ± 0.1	1.0 ± 2.0
43	40.2	10.0	2.4 ± 3.0	4.9 ± 0.1	4.8 ± 0.1	1.0 ± 2.0
43	40.2	11.4	2.9 ± 3.0	4.9 ± 0.1	4.8 ± 0.1	1.0 ± 2.0
52	49.4	10.4	2.1 ± 3.0	5.2 ± 0.1	5.1 ± 0.1	1.0 ± 2.0

Table 2: Results of different spin-resolved spectra. For each spectrum we give the polarization and the spin-dependent IMFP as determined with eqn. 51

Additional information can be provided by comparing spectra of different coverages but with the same kinetic energy. In fig. 7.10a-d we showed spectra that were taken with 15eV photon energy. In these spectra we see an increase of the polarization of the Cu signal with increasing Co coverage. When we plot the polarization P_{Cu} of the Cu signal as a function of Co coverage, as we did in fig. 7.11, we find within the error bars an approximately linear dependence. This is reasonable since the different scattering probabilities for majority- and minority-spin electrons polarize the electron beam originating from the Cu substrate more and more when the electrons travel through the Co film.

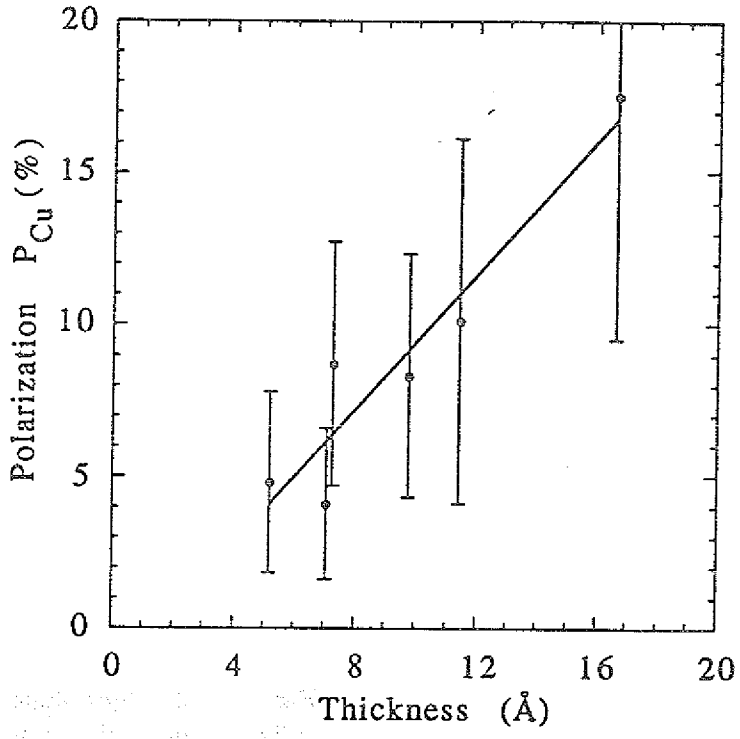

Fig. 7.11: Polarization P_{Cu} of the Cu peak as a function of the Co coverage for 12eV kinetic energy. The data were taken from table 2.

This increase of the polarization with the coverage has been observed also at different energies but for 15eV photon energy we recorded by far the most spectra.
At 25eV photon energy the analysis of the spin-resolved spectra is more difficult than for other energies due to the different shape of the majority spectrum at this energy. We tried to take this into account when subtracting the Cu contribution in the spectra, but the uncertainty of the results at 25eV is in any case larger. This explains that we get two rather different values for the asymmetry in table 2 for 25eV photon energy.

A plot showing $\lambda^{\uparrow\downarrow}$ versus kinetic energy (referred to E_F) is presented in fig. 7.12. Filled circles correspond to majority-spin electrons and open circles correspond to minority-spin electrons. The lines show a least-squares fit of a third-order polynomial to the data. For kinetic energies above 30eV the polarization is so small (below 4%) that the difference between $\lambda^{\uparrow}$ and $\lambda^{\downarrow}$ lies within the error of the measurement for all the observed spectra but towards lower energy we find the IMFP values are more different for the two spin directions. Especially at 12eV kinetic energy (that corresponds to 15eV photon energy), where several data points exist, we can establish a difference of $\lambda^{\uparrow}$ and $\lambda^{\downarrow}$ of about 1Å.
A different way to plot the data of fig. 7.12 is given in fig. 7.13. It shows the mean free path asymmetry defined in eqn. 51 as a function of the kinetic energy of the electrons (referred to E_F). As mentioned above this way to plot the results has the advantage of being rather insensitive to uncertanties in the determination of the averaged IMFP.
A_λ is small or zero for kinetic energies above 30eV but increases towards low kinetic energies. At 12.4eV kinetic energy we can give a rather reliable value of $A_\lambda \approx 0.065$. In all these plots (fig. 7.10-7.12) we obtained large error bars compared to the absolute size of

the effects expressing how small the spin-dependence of the scattering is in Co.

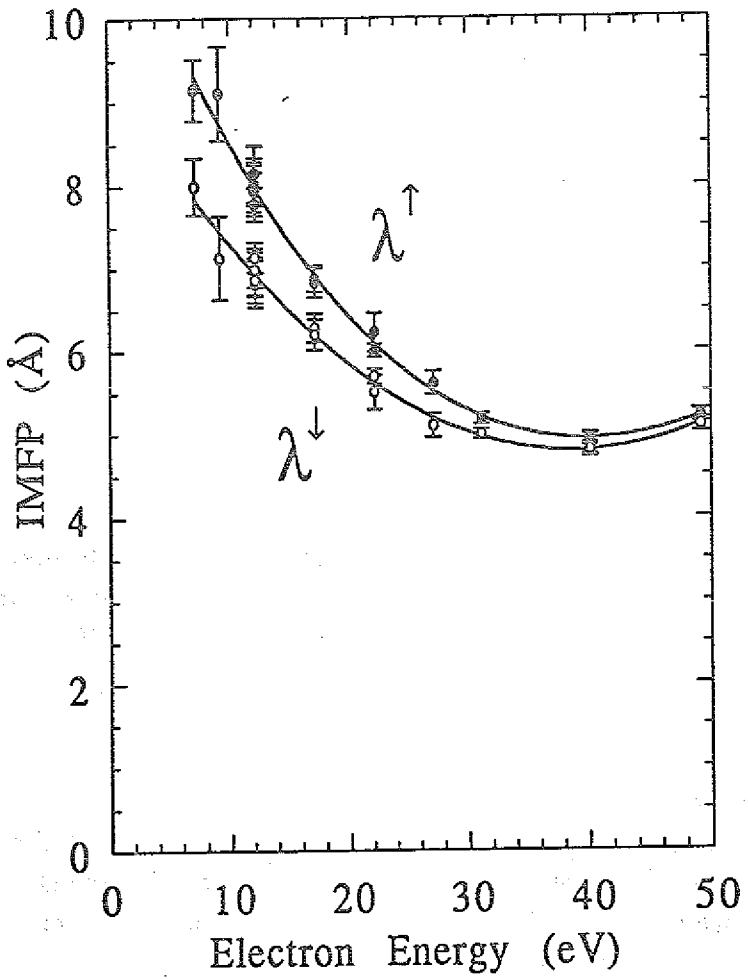

Fig. 7.12: Spin-dependent inelastic mean free path determined from spin-polarized photoemission spectra. Filled (empty) circles correspond to majority- (minority-) spin electrons. The full line show a least-squares fit of a 3rd order polynom.

Until now we have discussed the spin-dependent asymmetries in the transmission through the Co film on the basis of different IMFP's for the two spin-directions, as Pappas did in his work about 4ML Fe/Cu(100) [Pappas, 91]. Another explanation for the spin-dependent asymmetries has been proposed by Gokhale [Gokhale, 91]. Gokhale calculated spin-dependent asymmetries for electrons transmitted through thin magnetic Fe films on the basis of different cross sections for *elastic scattering* due to exchange coupling to the atom of the ferromagnetic adsorbate rather than different cross sections for inelastic scattering. He calculates transmission asymmetries (P_{Cu} in our analysis) for 1-5 ML Fe on Cu(100) and electron energies up to 40eV. Due to the fact that Gokhale's calculations were performed for Fe instead of Co we can compare our results only qualitatively with his calculations. We show these results for energies ranging from 20eV to 40eV in fig. 7.14. The calculations predict strong oscillations with energy and also with coverage. At a kinetic energy of 30eV for example the polarization of the Cu peak changes from 0% for 1ML to +50% for 3ML, -15% for 4ML and again 0% for 5ML Fe/Cu(100). Similar oscillations are predicted when the electron energy changes. This can be seen best for

the 3ML film in fig. 7.14. The results of Pappas agree very well with the asymmetries predicted in this theory although the comparison could not be considered to be conclusive because of the very limited number of experimental data points.
Calculations for Co are not available. However, if the model by Gokhale can be applied one would expect to observe an oscillation of the polarization for a given coverage by varying the photoelectron energy and, conversely, for a fixed electron energy by varying the coverage.
Experimentally, we did not observe such oscillations. We found a smooth decrease of the polarization with increasing electron energy for similar Co coverages leading to the calculated decrease of the mean free path asymmetry in fig. 7.13. For different Co coverages we observed a linear increase of the polarization with film thickness (fig.7.13).
We did not see any indication for the predicted strong oscillations in the polarization of the Cu peak and therefore think that Gokhales theory cannot be applied to explain our results about the spin-dependent attenuation and that elastic scattering is in our case not the dominant scattering process.

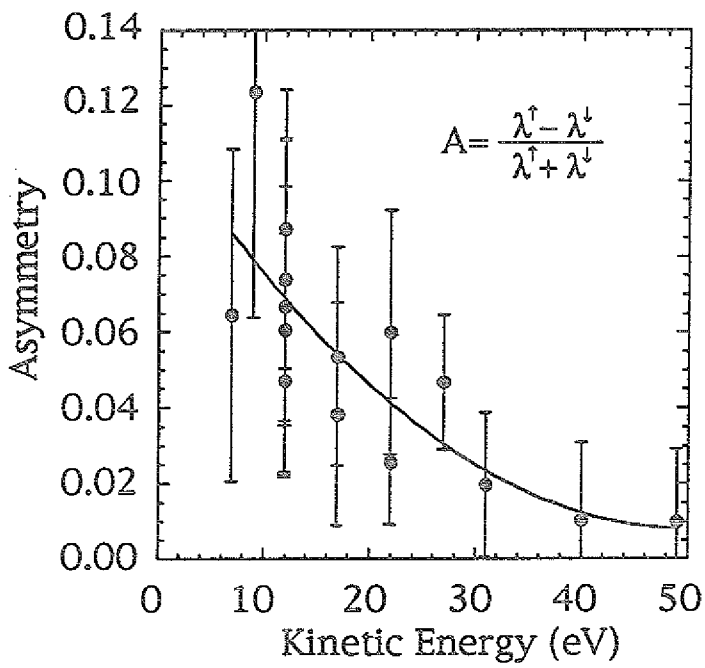

Fig. 7.13: Mean free path asymmetry A_λ as a function of the kinetic energy of the electrons (referred to E_F). Data are taken from table 2. The full line show a least-squares fit of a 2nd order polynom.

The atomistic model of Bringer [Bringer, 79] strongly overestimates the spin dependence of the IMFP. With 9 electrons per Co atom ($n^{\uparrow} + n^{\downarrow} = 9$) and a difference in the occupation of the majority- and minority-spin states of 1.5 electrons per atom ($n^{\uparrow} - n^{\downarrow} = 1.5$) [Tebble, 69] one gets (using eqn. 45) a mean free path asymmetry of 0.17 for Co, independent on the electron energy. The sign of A_λ agrees with our results, but the magnitude and the energy dependence were found to be different. At very low kinetic energies where we found the strongest asymmetries our results are still by about a factor of two smaller than Bringers predictions. Instead of an energy independent A_λ we measured a strong

decrease of A_λ with increasing electron energy.
The models of Penn [Penn, 85] and Rendell and Penn [Rendell, 80] agree better with our data since they both predict a decreasing spin dependence for higher electron energies. In ref. [Penn, 85] predictions are made about the spin dependent IMFP only for a rather limited energy range at very low energy (0-5eV above E_{Vac}). Two of our data points fall within this range (spectra taken with 10eV and 12eV photon energy). They agree in magnitude with the calculated spin asymmetries although the decrease of A_λ at higher energies is smaller in theexperiment. We therefore do not agree with the statement of Penn that the mean-free-path difference between majority and minority spins is significant only at very low energies.

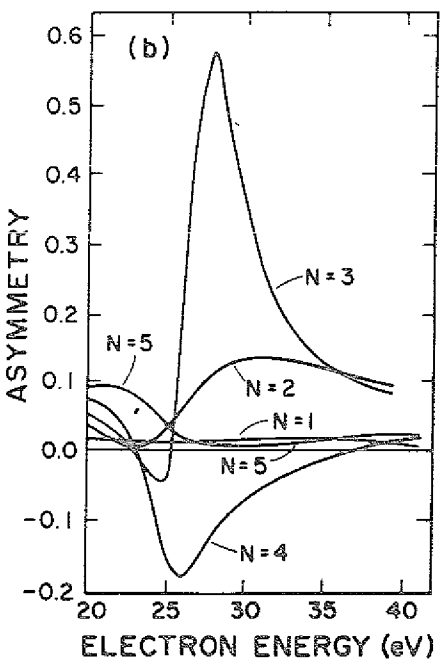

Fig. 7.14: The asymmetry in transmissivity ($= P_{Cu}$) for films that range from 1 to 5 monolayers, in the energy range 20-40eV (referred to the vacuum level) after [Gokhale, 91].

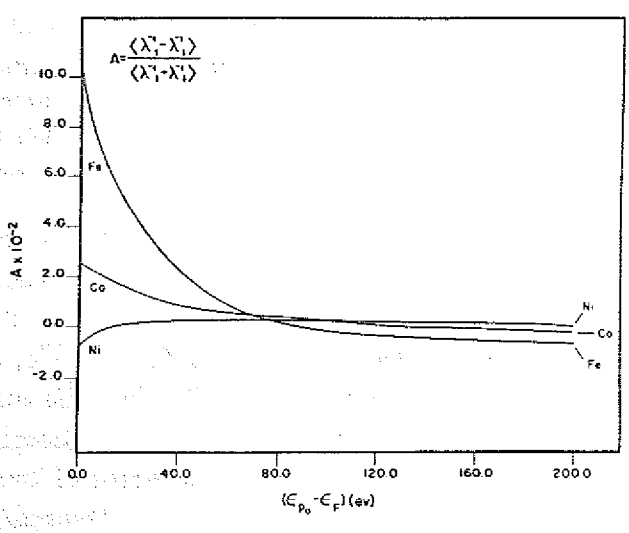

Fig. 7.15: Calculated difference of IMFP for incident electron with spin parallel and antiparallel to majority spins of Fe, Co and Ni as a function of incident electron energy after ref. [Rendell, 80]

At higher energies we find a better agreement with the model of Rendell and Penn [Rendell, 80]. Although experimentally the absolute values of A_λ are always about 3 times less than in this calculation, they predict the energy dependence of the results more accurate. Experimentally the decrease of A_λ is faster, but the energy range where effects can be expected is predicted correctly. The decrease of the mean free path asymmetry of Fe, Co and Ni with electron energy as calculated by Rendell is shown in in fig. 7.15. One can see that the effect is larger for Fe. This is consistent with the fact that Pappas [Pappas, 91] measured stronger asymmetries in the system Fe/Cu(100).
When we compare the model for elastic scattering of Gokhale [Gokhale, 91] with the model of Penn [Penn, 85] or Rendell and Penn [Rendell, 80] for inelastic scattering, we conclude that the dominant scattering process is the inelastic scattering. We cannot see the oscillations predicted by Gokhale, but we observe the decrease of the polarization with increasing electron energy as predicted in the models for inelastic scattering.

Summarizing our results about the IMFP of electrons in Co obtained in the last two chapters we can say the following. With spin-integrated photoemission spectra we find an IMFP curve for electrons, travelling through a thin cobalt film, that agrees qualitatively with the theoretical curve predicted by Seah and Dench [Seah, 79] for Co. It shows a minimum at about 30-50eV electron energy and increases towards low and high energy.
We found a difference for majority-spin and minority-spin electrons in the attenuation of the Cu peak in spin-resolved measurements. The effects are very small, but due to the good statistics in our spectra and the large amount of available data we are able to establish the difference for low kinetic energies. The polarization P_{Cu} of the Cu signal in the spin-resolved spectra increases proportional to the thickness of the ferromagnetic Co overlayer. The different attenuation for the two spin directions can be explained with a difference in the IMFP for majority- and minority-spin electrons. The IMFP for majority-spin electrons has been found to be larger than for minority-spin electrons at kinetic energies below 30eV. A comparison of the results with the available theoretical models indicates that in our case elastic scattering is of minor importance.

8 Final States of Cu(100) and Co(100)

Angle-resolved energy distribution measurements of secondary-electron emission from metals reveal spectral fine structure that relates directly to the density distribution of the one-electron states above the vacuum level.
Structures in the secondary electrons can be seen best at low kinetic energies, where the inelasically scattered electrons accumulate.
In contrast to states below E_F which produce primary electrons with kinetic energies changing according to the energy of the incident light ($E_{kin} = h\nu - E_B - \Phi$), final state structures in the secondaries are located at fixed kinetic energies.

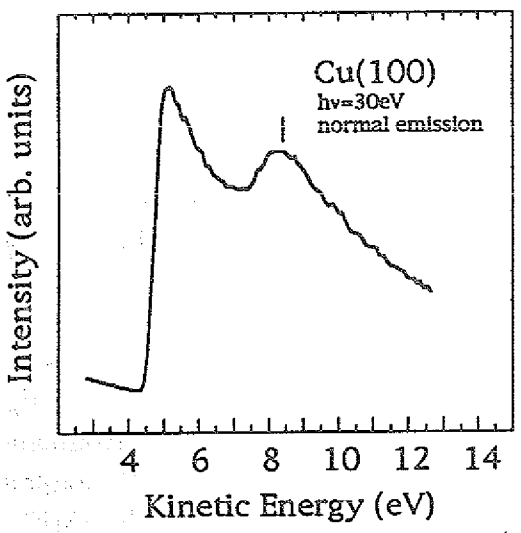

Fig. 8.1a: Spin-integrated spectra of clean Cu(100) taken with s-polarized light of 30eV photon energy in normal emission. The kinetic energy is referred to E_F.

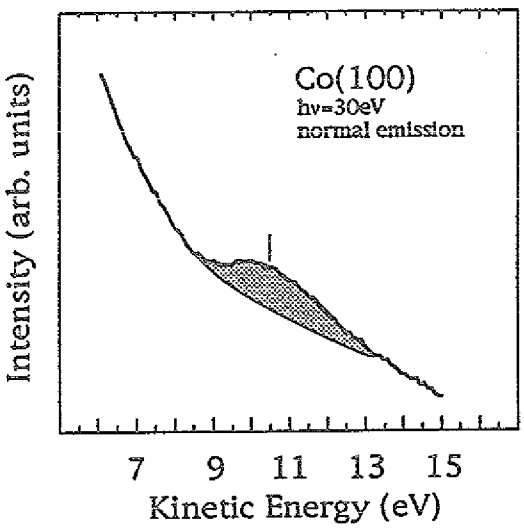

Fig. 8.1b: Spin-integrated spectra of Co(100) taken with s-polarized light of 30eV photon energy in normal emission. The kinetic energy is referred to E_F.

With Cu(100) and Co(100) we found such structures at low kinetic energies. In fig. 8.1a and 8.1b we show photoemission spectra of Cu(100) and Co(100) in the range of the secondary electrons. The spectra show a broad structure at 8.5eV (Cu(100)) and 10.5eV (Co(100)). The states were found to be at fixed kinetic energy. When the photon energy is changed the peaks shift with respect to the Fermi level in the photoemission spectra. The energy axis corresponds for that reason to the kinetic energy of the electrons.
The zero in the kinetic energy corresponds to Fermi level and the onset of the secondary-electron emission (4.8eV in fig. 8.1a) defines the vacuum level. Final states below the vacuum level cannot be detected since the electrons in these states can not overcome the work function.

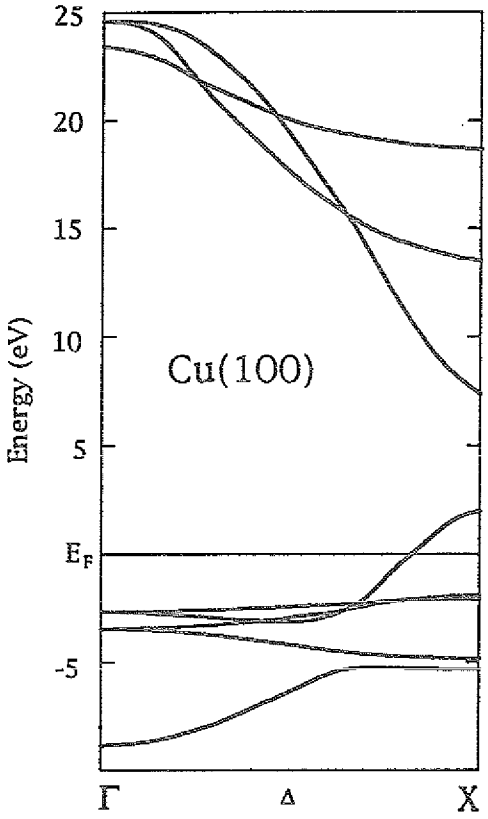

Fig. 8.2a: Band structure of Cu along the direction $\Gamma - X$ of the fcc Brillouin zone including final-state bands as calculated by Burdick [Burdick, 62].

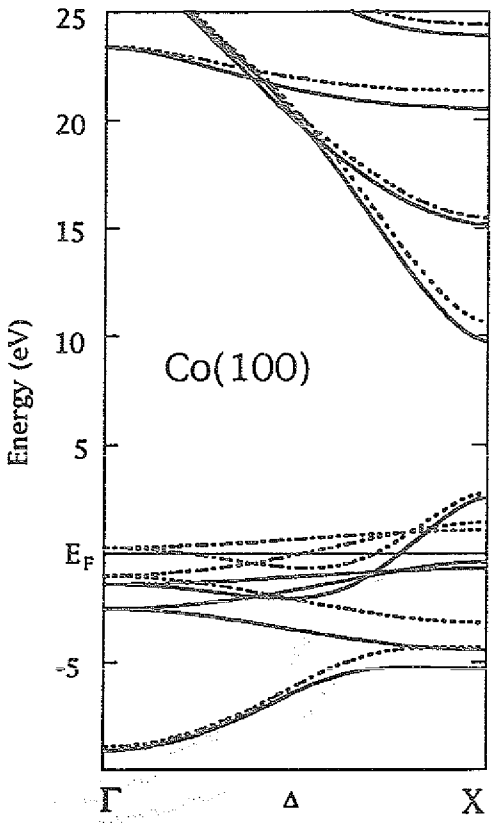

Fig. 8.2b: Band structure of Co along the direction $\Gamma - X$ of the fcc Brillouin zone including final-state bands as calculated by Noffke [Noffke, priv.]

For the interpretation of the structures we show in fig. 8.2a and 8.2b the band structures of copper and cobalt in $\Gamma - X$ direction as calculated by Burdick [Burdick, 62] and Noffke [Noffke, priv.]. We see again the s- and d-bands of the two metals that have been studied already in chapter 5.
The final statesabove E_F are shown in fig. 8.2 up to 25eV. For ferromagnetic cobalt they are spin split (straight lines were used for majority bands, broken lines for minority bands). The final-state band, that reaches down to 8eV on Cu at the X point, has Δ_1 symmetry and shows a dispersion that is very similar to the free-electron parabola.
Near X, where this Δ_1 band becomes flat, the density of states increases. In the range 2eV to 8eV there is gap between the valence bands and the Δ_1 final-state band of Cu in the direction $\Gamma - X$.
The energy of the observed structure in the photoemission spectra (fig. 8.1a) agrees well with the increased density of states at about 8eV. When the electrons are inelastically scattered, they scatter with a high probability into Δ_1 states near X, leading to the observed peak. Due to the fact, that there are no final-state bands for lower energies, one

expects a dip in the secondary-electron emission for lower energies that stresses the peak even more.
For Co(100) we see a similar structure at higher kinetic energy (10.5eV). This is in agreement with the fact, that the corresponding Δ_1 bands for Co(100) has an energy of 10eV at the X-point.

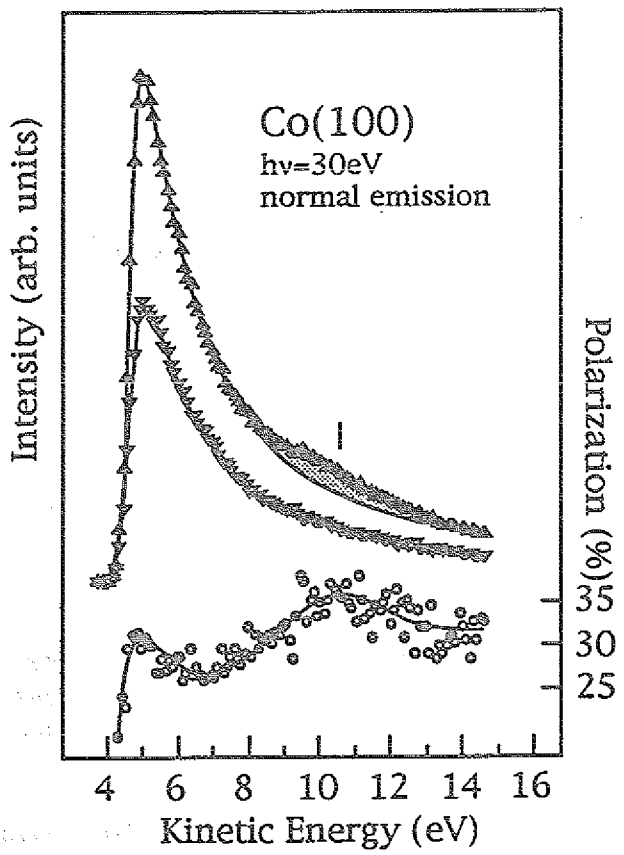

Fig. 8.3: Spin-resolved photoemission spectrum of a thick Co layer on Cu(100)($\approx$ 20ML). $\triangle$ and $\triangledown$ are used for majority- and minority-spin electrons. Circles show the corresponding polarization ($P(E) = (I^{\uparrow} - I^{\downarrow})/(I^{\uparrow} + I^{\downarrow})$

Spin-resolved photoemission spectra of a Co(100) film ($\approx$ 20ML), taken at the same photon energy in normal emission, are shown in fig. 8.3. In this figure we show the energy distribution curves of majority- (filled triangles up) and minority-spin (open triangle down) direction together with the polarization ($(I^{\uparrow} - I^{\downarrow})/(I^{\uparrow} + I^{\downarrow})$). The spin-resolved spectra reveal the majority-spin character of the final-state structure on Co. A peak in the minority-spin spectrum can be expected 1eV higher in energy than in the majority-spin spectrum, when comparing the minority and the majority Δ_1 final-state band. Obviously we do not see this peak in the minority spectrum of the spin-resolved spectrum. We expect the structure to be weaker in the minority spectrum due to the fact that the overall emission is smaller, but that does not explain the lack of observation of the minority peak. When comparing the bandstructure of Co for minority- and majority-spin direction in fig. 8.2b one finds that much more unoccupied states near E_F exist for minority-

than for majority-spin electrons. Consequently, the scattering probability of majority-spin electrons into unoccupied states of lower energy is smaller than for minority-spin electrons. This qualitative argument for the explanation of the polarized final-state structure in Co(100) is obviously connected to the spin dependence of the inelastic scattering discussed in the previous chapter. It can be related to the argument of Penn [Penn, 85] although the present calculation does not include a detailed analysis with respect to the photoelectron wave vector k.

It has been discussed in the previous chapter that secondary-electron emission of magnetic bulk materials has been found to show an increased polarization for low-energy electrons. The polarization in fig. 8.3 does not increase between 14eV and 4eV kinetic energy. It shows structures corresponding to the final-state structures explained above, but no increase.

This is due to the limited thickness of the Co films ($\approx$ 20ML). We did not see any signal of the Cu substrate in the valence band or in the Auger spectrum, but due to the fact that the IMFP steeply increases towards low energies, the photoemission spectrum may be influenced by electrons originating from the substrate as one goes to very low kinetic energies. The electrons originating from the Cu substrate are unpolarized and mainly decrease the average polarization of the spectrum. They become more dominant as one goes to low energies, the IMFP becomes longer and more substrate electrons reach the detector.

9 Summary

In this work we have studied the electronic and magnetic structure of Co/Cu(100) and Co/Cu(111) using spin- and angle-resolved photoemission spectroscopy, Auger electron spectroscopy and low-energy electron diffraction.

The growth of cobalt on the (111) surface of copper has been studied under ultra-high vacuum conditions at room temperature using Auger-electron spectroscopy and low-energy electron diffraction. It has been found that cobalt grows layer-by-layer (Frank van der Merve growth) on Cu(111). The overlayer grows epitaxially with the fcc structure of the substrate up to at least 5.5 monolayers (ML).

The band structure of Cu has been found in good agreement with theory [Burdick, 62] and previous experiments [Thiry, 81]. We determined the dispersion of the Δ_5 and Λ_3 bands in the high-symmetry directions $\Gamma - X$ and $\Gamma - L$ of the fcc Brillouin zone.

We have followed the transition from a 2D to a 3D character of the electronic structure of Co/Cu(111) with increasing coverage. Below 1ML Co/Cu(111) shows no dispersion of the Co states with respect to $k_\perp$ (momentum perpendicular to the surface) and is for that reason regarded as a 2D system. Coverages of more than 5.5ML show a dispersion with $k_\perp$ comparable to bulk Co.

At 2ML Co/Cu(111) we observed the onset of magnetization in the surface plane. We interpret this with a rotation of the magnetization axis from the surface-normal direction into the surface plane.

With a thick layer ($\approx 20ML$) of Co on Cu(111) the spin-split band structure of Co has been studied using spin-resolved photoemission. The Λ_3 bands of Co reveal an exchange splitting at the Γ point ($\Delta E_{ex} = 1.4 \pm 0.2$eV) that is larger than reported by other groups for Co(1000) [Himpsel, 80] and 2ML Co/Cu(111) [Miranda, 82] but agrees with the results of a previous work on Co/Cu(100) [Clemens, 92].

The inelastic mean free path (IMFP) of electrons transmitted through a thin Co film has been determined by measuring the attenuation of the Cu(111) substrate signal with increasing Co overlayer thickness.
The IMFP as a function of electron kinetic energy follows qualitatively the *universal curve* having a minimum at 30-50eV electron energy and increasing towards very low and high energies.
For electron kinetic energies below 30eV (referred to E_F) the IMFP was found to depend on the electron spin. In Co it is larger for majority-spin electrons than for minority-spin electrons. The spin dependence of the IMFP increases towards low energies. A comparison of the results of this study to the available theoretical models about spin-dependent scattering shows that elastic scattering is of minor importance.

In the secondary-electron emission of Cu(100) and Co(100) we observed structures that originate from final-state bands above the vacuum level. They are due to emission from a band of Δ_1 symmetry with a high density of states at the X-point of the fcc Brillouin zone. In Co these structures are spin polarized.

10 Acknowledgements

This work was done at the *Institut für Elekronische Eigenschaften* (IFF/IEE) within the *Institut für Festkörperforschung* of the *Forschungszentrum Jülich* (KFA).
Firstly, I thank Prof. Dr. W. Eberhardt for giving me the possibility to perform my diploma work in his institute. He suggested the subject of the thesis and was always available for many helpful discussions.
I am greatly indebted to Dr. C. Carbone who guided me during this thesis with his knowledge and his expertise, and to Dr. T. Kachel who introduced me to ultrahigh vaccum techniqes.
A very special thanks is given to Dr. E. Vescovo and O. Rader who spent so many days and nights with me at the experiment at Bessy in Berlin.
I am very grateful to W. Clemens for the discussions, and to Dr. Kevin Colbow who improved this thesis with respect to vocabulary and comprehensibility.
Finally I thank the members of the IFF/IEE and the BESSY staff for their helpfulness and pleasant atmosphere.

References

[Andersson, 73] S.Andersson and U.Jostell, Solid State Commun. **13**, 829 (1973)

[Argile, 89] C.Argile and G.E.Rhead, Surface Science Reports **10**, 277 (1989)

[Ascroft] N.W.Ashcroft and N.D.Mermin, *Solid State Physics*, Saunders College, Philadelphia (1976)

[Boutry, 69] G.A.Boutry and H.Dormont, Philips Tech. Rev. **30**, 225 (1969)

[Bringer, 79] A.Bringer, M.Campagna, R.Feder, W.Gudat, E.Kisker, and E.Kulhmann, Phys. Rev. Lett. **42**, 1705 (1979)

[Burdick, 62] G.A.Burdick, Phys. Rev. **129**, 138 (1962)

[Cardona] *Photoemission in Solids I and II*, ed. by M.Cardona and L.Ley, Springer Berlin (1978/79)

[Clarke, 87] A.Clarke, G.Jennings, R.F.Willis, P.J.Rous, and J.B.Pendry, Surface Science **187**, 327 (1987)

[Clemens, 91] W.Clemens, *Berichte des Forschungszentrums Jülich*, Jül-2601 (1991)

[Clemens, 92] W.Clemens, T.Kachel, O.Rader, E.Vescove, S.Blügel, C.Carbone and W.Eberhardt, Solid State Communications **81**, 739 (1992)

[Eberhardt, 80] W.Eberhardt and F.J.Himpsel, Phys. Rev. B **21**, 5572 (1980)

[Einstein, 1905] A.Einstein, Ann. Physik **17**, 132 (1905)

[Gartland, 75] P.O.Gartland and B.J.Slagsvold, Phys. Rev. B **12**, 4047 (1975)

[Getzlaff, 92] M.Getzlaff, J.Bansmann, C.Westphal, and G.Schönhense , Journal of Magnetism and Magnetic Materials **104-107**, 1781 (1992)

[Gokhale, 91] M.P.Gokhale and D.L.Mills, Phys. Rev. Lett **66**, 2251 (1991)

[Gonzalez, 81] L.Gonzalez, R.Miranda, M.Salmerón, J.A.Vergés, and Felix Ynduróin, Phys. Rev. B **24**, 3245 (1981)

[Gradmann, 70] U.Gradmann und J.Müller, Zeitschrift für angew. Physik **30**, 87 (1970)

[Gradmann, 71] U.Gradmann and J.Müller, Czech. J. Phys. B **21**, 553 (1971)

[Gradmann, 73] U.Gradmann, Applied Physics **3**, 161 (1973)

[Gradmann, 83] U.Gradmann, Physical Review B **27**, 1935 (1983)

[Hermanson, 77] J.Hermanson, Solid State Comm. **22**, 9 (1977)

[Himpsel, 79] F.J.Himpsel and D.E.Eastman, Physical Review. B 20, 3217 (1979)

[Himpsel, 80] F.J.Himpsel and D.E.Eastman, Physical Review. B 21, 3207 (1980)

[Kessler, 85] J.Kessler, *Polarized Electrons* 2nd ed., Springer Ser. Atoms Plasmas, Vol. 1, Heidelberg (1985)

[Kisker, 82] E.Kisker, W.Gudat, and K.Schröder, Solid State Commun. 44, 591 (1982)

[Kittel] C.Kittel, J.Wiley, & Sons, *Introduction to Solid State Physics*, New York (1986)

[Langmuir, 32] I.Langmuir, J. Am. Chem. Soc. 54, 2798 (1932)

[Lee, 78] B.W.Lee, R.Alsenz, A.Ignatiev, and M.A.Hove, Phys. Rev. B 17, 1510 (1978)

[C.Li, 91] H.Li, A.J.Freeman, and C.L.Fu, Journal of Magnetism and Magnetic Materials 94, 134 (1991)

[H.Li, 90] H.Li and B.P.Tonner, Surface Science 237, 141 (1990)

[Matthew, 82] J.A.D.Matthew, Phys. Rev. B 25, 3326 (1982)

[Michaelson, 77] H.B.Michaelson, Journal of Applied Physics 48, 4729 (1977)

[Miguel, 89] J.J.de Miguel, A.Cebollada, J.M.Gallego, S.Ferrer, R.Miranda, C.M.Schneider, P-Bressler, J.Garbe, K.Bethke, and J.Kirschner, Surf. Sci. 211, 732, (1989)

[Miranda, 82] R.Miranda, F.Yndurain, D.Chandesris, J.Lecante, and Y.Petroff, Phys. Rev. B 25, 527 (1982)

[Moruzzi, 78] V.L.Moruzzi, J.F.Janak, and A.R.Williams, *Calculated Electronic Properties of Metals* (Pergamon, New York, 1978)

[Noffke, priv.] J.Noffke and L.Fritsche, priv. comm.

[Pappas, 91] D.P.Pappas, K.-P.Kämper, B.P.Miller, and H.Hopster, Phys. Rev. Lett. 66, 504 (1991)

[Penn, 76] D.R.Penn, Phys. Rev. B 13, 5248 (1976)

[Penn, 85] D.R.Penn, S.P.Apell, and S.M.Girvin, Phys. Rev. Lett. 55, 518 (1985)

[Pirug, 85] G.Pirug, A.Winkler, and H.P.Bonzel, Surf. Sci. 163, 153 (1985)

[Plummer, 82] E.W.Plummer and W.Eberhardt, *Angle resolved Photoemission as a Tool for the Study of Surfaces*, Adv. Chem. Phys. 49, 533 (1982)

[Quinn, 62] J.J.Quinn, Phys. Rev.126, 1453 (1962)

[Rader, 91] O.Rader, *Berichte des Forschungszentrums Jülich*, Jül-2558 (1991)

[Rendell, 80] R.W.Rendell and D.R.Penn, Phys. Rev. Lett 45; 2057 (1980)

[Sham, 89] T.K.Sham, G.-Q.Xu, J.Hrbek, and M.-L.Shek, Surface Science 210, L185 (1989)

[Seah, 79] M.P.Seah and W.A.Dench, Surface and Interface Analysis, 1, 2 (1979)

[Tebble, 69] R.S.Tebble and D.J.Craik, *Magnetic Materials* (Wiley, New York, 1969)

[Thiry, 81] P.Thiry, Thesis (french), Université Pierre et Marie Curie (Paris 1981)

[Tikhov, priv.] M.Tikhov and E.Bauer, priv. comm.

[Wimmer, 83] E.Wimmer, A.J.Freeman, J.R.Hiskes, and A.M.Karo, Phys. Rev. B 28, 3074 (1983)

[Wu, 91] S.C.Wu, H.Li, Y.S.Tian, and F.Jona, Phys. Rev. B 44, 13308 (1991)

[Zangwill, 88] A.Zangwill, *Physics at Surfaces*, Cambridge University Press, Cambridge(1988)

FORSCHUNGSZENTRUM JÜLICH GmbH

KFA

Jül-2706
Dezember 1992
ISSN 0366-0885